Analysis of the low-boiling working fluid expansion processes in the volumetric expander operating in the ORC system

Dissertation presented in partial fulfillment of the requirements for the degree of Doctor of Engineering (dr inż): Environmental Engineering, Mining, and Energy from Wrocław University of Science and Technology (WUST), Poland, and the degree of Doctor of Engineering (PhD): Mechanical and Energy Processes from Budapest University of Technology and Economics (BME), Hungary under a cotutelle agreement

Sindu Daniarta

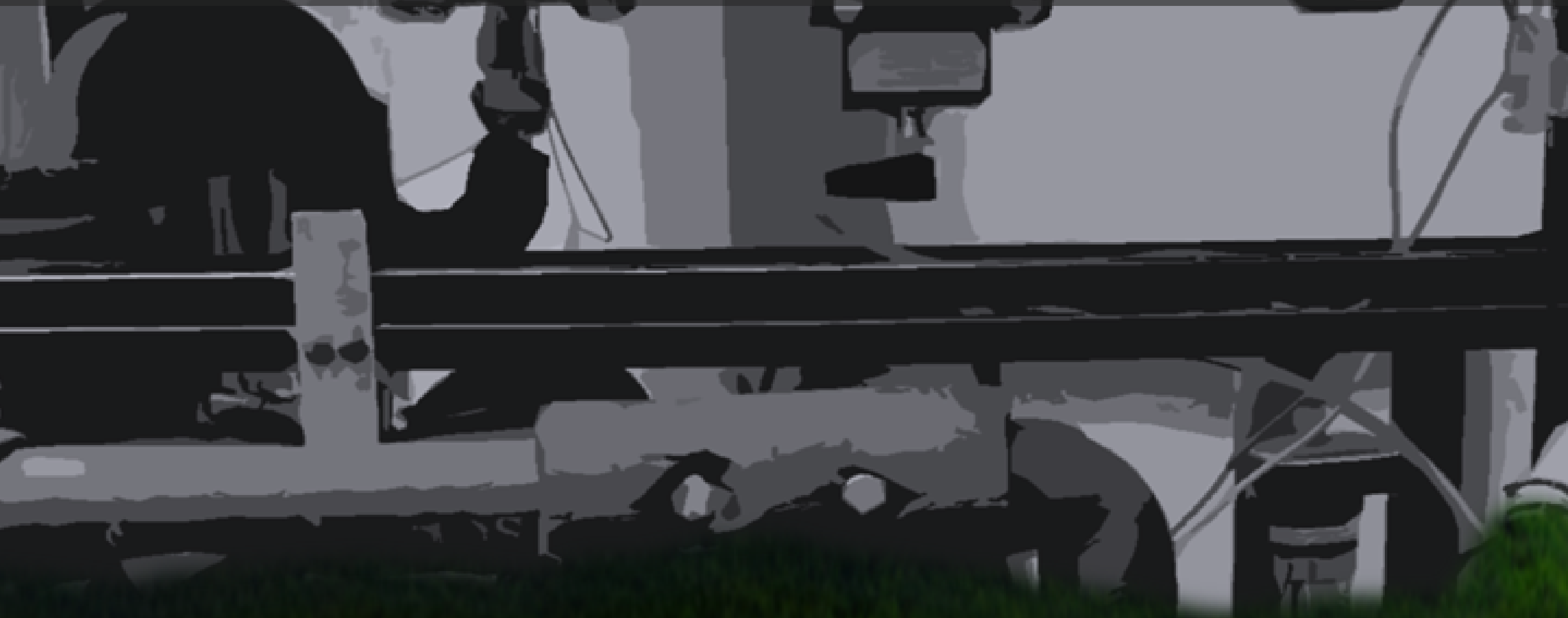

Wrocław University
of Science and Technology

MŰEGYETEM 1782

Wrocław University
of Science and Technology

MŰEGYETEM 1782

Analysis of the low-boiling working fluid expansion processes in the volumetric expander operating in the ORC system

Dissertation presented in partial fulfillment of the requirements for the degree of Doctor of Engineering (dr inż): Environmental Engineering, Mining, and Energy from Wrocław University of Science and Technology (WUST), Poland, and the degree of Doctor of Engineering (PhD): Mechanical and Energy Processes from Budapest University of Technology and Economics (BME), Hungary under a cotutelle agreement

presented in 2024
to the Doctoral School of WUST, and
the Géza Pattantyús-Ábrahám Doctoral School of Mechanical Engineering Sciences BME

by

Sindu Daniarta

Supervisors:

Supervisor from WUST : Prof. dr hab. inż. Piotr Kolasiński
Supervisor from BME : Prof. Attila R. Imre., PhD., DSc

Wrocław, 2024

Wrocław University
of Science and Technology

Field of Science: Energy
Discipline of Science: Environmental Engineering, Mining, and Energy

Doctoral Dissertation

Analysis of the low-boiling working fluid expansion processes in the volumetric expander operating in the ORC system

Sindu Daniarta

Supervisor:
prof. dr hab. inż. Piotr Kolasiński

Keywords: organic Rankine cycle, phase equilibria, partially evaporation, two-phase expander

Wrocław, 2024

BUDAPEST UNIVERSITY OF TECHNOLOGY AND ECONOMICS
FACULTY OF MECHANICAL ENGINEERING
DEPARTMENT OF ENERGY ENGINEERING

Sindu Daniarta

Doctoral Dissertation

Analysis of the low-boiling working fluid expansion processes in the volumetric expander operating in the ORC system

Supervisor:

Prof. Attila R. Imre., PhD., DSc.

Budapest, 2024

Abstract

An organic Rankine cycle (ORC) modifies the Clausius-Rankine cycle of the steam power plant by employing organic working fluid (or low-boiling working fluid) instead of water. While ORC technology is nowadays well-established in numerous applications, it still presents unexplored potential for further development, particularly in its ability to efficiently utilize intermittent and fluctuating heat sources. This dissertation conducts an analysis of the low-boiling working fluid expansion process and investigates how this process affects the efficiency of various ORC configurations (e.g., partially evaporated ORC, basic ORC, and ORC with a superheater). The study includes theoretical analysis and modeling simulations to evaluate the impact of this expansion on ORC efficiency using different working fluids. These analyses also compare different ORC systems with alternative thermodynamic cycles, namely the trilateral flash cycle and the transcritical power cycle. Moreover, an experimental investigation into the expansion process of low-boiling working fluids in an ORC system was carried out using a multi-vane volumetric expander. Further research predicted the wet isentropic efficiency of the two-phase expansion process using experimental data and artificial intelligence. The dissertation concludes by exploring the practical applications of volumetric expanders in ORC systems. Some results that are part of this dissertation demonstrate that incorporating a two-phase expansion system significantly enhances the adaptability of ORC systems to manage fluctuating low- and medium-temperature heat sources across several fields, including waste heat recovery, geothermal power systems, cold energy utilization, district heating systems, and Carnot batteries.

Keywords: organic Rankine cycle, phase equilibria, partially evaporation, two-phase expander

Streszczenie (Abstract in Polish)

Obieg ORC jest zmodyfikowanym obiegiem Clausiusa-Rankine'a, który wykorzystuje organiczne czynniki robocze (lub czynniki robocze o niskiej temperaturze wrzenia) zamiast wody. Chociaż technologia ORC jest obecnie dobrze rozwinięta i znajduje liczne zastosowania w przemyśle, nadal posiada ona potencjał do dalszego rozwoju i optymalizacji, szczególnie w zakresie efektywnego pozyskiwania energii ze źródeł ciepła, których charakterystyki termiczne i wydajność są przerywanych lub fluktuacyjne. W niniejszej dysertacji przeprowadzono analizę procesu rozprężania czynnika roboczego o niskiej temperaturze wrzenia i badano, jak ten proces wpływa na wydajność różnych konfiguracji układów ORC (np. układ ORC z częściowym odparowaniem czynnika roboczego, standardowy układ ORC, oraz układ ORC z przegrzewaczem). Badania te obejmują analizy teoretyczne oraz modelowe w celu oceny wpływu różnych parametrów zjawiska rozprężania na wydajność ORC przy użyciu różnych czynników roboczych. Porównano również różne alternatywne systemy ORC, w tym m.in. tzw. trilateral flash cycle i transcritical power cycle. Ponadto, przeprowadzono badania eks-perymentalne procesu rozprężania czynników roboczych o niskiej temperaturze wrzenia w systemie ORC, wykorzystując wielołopatkową rozprężarkę objętościową. Dalsze badania poświęcone były określaniu sprawności izentropowej procesu rozprężania dwufazowego, wykorzystując dane eksperymentalne i sztuczną inteligencję. W pracy rozeznano też możliwe kierunki praktycznego zastosowania rozprężarek objętościowych w systemach ORC. Niektóre uzyskane w czasie badań wyniki, wskazują, że zastosowanie rozprężania dwufazowego znacząco zwiększa możliwości wykorzystania układów ORC do pozyskiwania energii ze źródeł ciepła o zmiennych charakterystykach oraz niskiej i średniej temperaturze w różnych dziedzinach, w tym odzysku ciepła odpadowego, systemach geotermalnych, wykorzystaniu chłodu, systemach ciepłowniczych oraz bateriach Carnota.

Słowa kluczowe: cykl Rankine'a z cieczą organiczną, równowaga fazowa, częściowe odparowanie, rozprężarka dwufazowa

Kivonat (Abstract in Hungarian)

A szerves Rankine-ciklus (ORC) a Clausius-Rankine ciklus egy típusa, amely a hagyományos gőzerőművekben alkalmazott víz helyett szerves munkaközeget (általában valamilyen alacsony forráspontú hűtőközeget) használ. Míg az ORC technológia használata napjainkban már számos alkalmazásban jól megalapozott, tová-bbi fejlesztési potenciált rejt magában, különösen a szakaszosan és ingadozóan jelentkező hőforrások hatékony hasznosításának képességét illetően. A disszertáció tárgya az alacsony forráspontú hűtőközegek expanziós folyamatainak elemzése, különös tekintettel arra, hogy ez a folyamat hogyan befolyásolja különböző ORC konfigurációk (például részleges elpárologtatású ORC, alap ORC, valamint túlhevítős ORC) hatékonyságát. A tanulmány elméleti elemzéseket és szimulációkat foglal magában, hogy értékelje az expanzió hatását az ORC hatásfokára és más tulajdonságaira, különböző hűtőközegek használata esetén. Ezek az elemzések továbbá összehasonlítják a különböző ORC rendszereket alternatív termodinamikai ciklusokkal, nevezetesen a trilaterális flash ciklussal és a transzkritikus ciklussal. Ezenkívül egy kísérleti vizsgálat is bemutatásra kerül, amelyben az alacsony forráspontú hűtőközegek expanziós folyamatát egy ORC-rendszerbe illesztett többlamellás volumetrikus expanderen vizsgáltuk. Emellett ismertetünk egy prediktív módszert a kétfázisú expanziós folyamat kevert fázisú (nedves gőz) hatásfokának megbecsülésére, kísérleti adatok és mesterséges intelligencia felhasználásával. A disszertáció végül a volumetrikus expanderek gyakorlati alkalmazásait vizsgálja az ORC rendszerekben. A disszertáció részét képező néhány eredmény azt mutatja, hogy egy kétfázisú expander beépítése jelentősen növeli az ORC konfigurációk alkalmazkodóképességét az ingadozó hőáramú, alacsony és közepes hőmérsékletű hőforrások hasznosításának több területen, beleértve a hulladékhőt, a geotermikus hőt és a kriogenikus hőt, a távfűtési rendszereket és a Carnot-akkumulátorokat.

Kulcsszavak: szerves Rankine-ciklus, fázisegyensúlyok, részleges elpárologtatás, kétfázisú expander

Declaration

Undersigned, Sindu Daniarta, author of this dissertation, hereby, I declare that I prepared this dissertation myself and I used only the referred sources. All parts of the dissertation, which are either cited verbatim or with the same content but rephrased as in the original source, are referred to unambiguously and provide the sources used. Furthermore, under the cotutelle agreement, the dissertation submitted to Wrocław University of Science and Technology in Poland is identical to the one submitted to Budapest University of Technology and Economics in Hungary.

Wrocław, 1 July 2024

Sindu Daniarta

Acknowledgments

This dissertation focuses on a modular thermal power plant which operates via an advanced organic Rankine cycle, which has the potential to provide reliable and cost-effective power to communities with varying energy demands. The research presented here has been conducted with the guidance and support of many individuals and institutions.

First and foremost, I would like to express my sincere gratitude to my advisors, prof. dr hab. inż. Piotr Kolasiński from Wrocław University of Science and Technology (WUST), Poland, and Prof. Attila R. Imre., PhD., D.Sc from Budapest University of Technology and Economics (BME), Hungary, for their invaluable guidance, encouragement, and feedback throughout this research. Their expertise and passion for this topic have been instrumental in shaping the direction and focus of this work. I also extend my heartfelt thanks to them for their support in facilitating this joint research doctoral program under the cotutelle agreement between WUST and BME. This cotutelle agreement has been a key factor in making this international scientific collaboration possible.

Furthermore, I would like to thank all of my colleagues from the Department of Thermodynamics and Renewable Energy Sources, WUST, and from the Department of Energy Engineering, BME, for the open-minded and motivating conversations in science and life that helped the progress of this research. Also, I am thankful for the insightful exchanges and feedback from colleagues I have met at various international conferences in Munich, Seville, Eger, Pilsen, and Bandung, as well as those at summer, winter, and training schools in Delft, Szczecin, Jakarta, Moscow, Gdańsk, and during my research mobility in London and Budapest. These interactions have been invaluable in advancing this study.

This work was supported by NAWA STER Program Internationalization of Wrocław University of Science and Technology Doctoral School. This research was supported and funded by the Department of Thermodynamics and Renewable Energy Sources, WUST. This study was supported and funded by the Faculty of Mechanical and Power Engineering through Wspieramy Młodych Naukowców 2022. Part of the research reported in this dissertation and carried out at BME has been supported by Project No. RRF-2.3.1-21-2022-00009, titled National Laboratory for Renewable Energy has been implemented with the support provided by the Recovery and Resilience Facility of the European Union within the framework of Programme Széchenyi Plan Plus. Part of this work was performed in the frame of the FIEK_16-1-2016-0007 project, implemented with the support provided by the National Research, Development and Innovation Fund of Hungary, financed under the FIEK_16 funding scheme. Moreover, part of the research reported in this dissertation and carried out at BME has been supported by the NRDI Fund (Grant No. BME-NC) based on the charter of bolster issued by the NRDI Office under the auspices of the Ministry for Innovation and Technology. Part of the research reported in this dissertation and carried out at BME was funded by the Sustainable Development and

Technologies National Programme of the Hungarian Academy of Sciences (FFT NP FTA). This research was also supported by the Foundation for Polish Science (FNP) through the START program 2024.

Last but certainly not least, I am deeply indebted to my family and friends, who have provided unwavering support and encouragement throughout my academic journey. Their love, patience, and understanding have been a constant source of motivation, and their contributions are too numerous to list individually here. Their support is a significant contributor to my success. I could not have completed this work without them.

Wrocław, 1 July 2024

Sindu Daniarta

Contents

List of Figures

List of Tables

Nomenclature

Symbols

$C_{\text{p,i}}$	total purchase cost	EUR
C_{BM}	capital cost of the bare module	EUR
C_{TM}	capital cost of the total module	EUR
C_{t}	cost of operation and maintenance	EUR
COP	coefficient of performance	-
d	annual discount rate	-
E	energy	J
F_{BM}	multiplication factor of bare module	-
F_{TM}	multiplication factor of total module	-
g	gravitational acceleration	m/s^2
h	specific enthalpy	J/kg
$LCOE$	levelized cost of electricity	EUR/W
m	mass	kg
$\dot{m}$	mass flow rate	kg/s
n	number of components	-
N	rotational speed	rpm
p	pressure	MPa
P	power	W
$P2P$	power-to-power	-
$\dot{Q}$	heat transfer rate	W
R^2	coefficient of determination	-
s	specific entropy	J/kg·K
SIC	specific investment cost	EUR/W
t	time	s
τ	torque	Nm
T	temperature	K
v	velocity	m/s
V	volume	m^3
$\dot{V}$	volumetric flow rate ($\dot{V} = \dot{m} \cdot \rho$)	m^3/s
$\dot{W}$	energy rate or power	W
W	energy	J
x	vapor quality	-
y	wet quality	-
Y_i	experimental data	-
$\hat{Y}_i$	predicted data or validated data	-
z	height or elevation	m
η_{cycle}	efficiency of cycle	-

$\eta_{\text{PMP,is}}$	isentropic efficiency of pump	-
$\eta_{\text{EXP,is}}$	isentropic efficiency of expander	-
$\eta_{\text{EXP,is,wet}}$	wet isentropic efficiency of expander	-
$\eta_{\text{EXP,is,dry}}$	dry isentropic efficiency of expander	-
ρ	specific density	kg/m^3

Abbreviations

BR	Bayesian regularization
CDS	condenser
CFC	chlorofluorocarbons
CFDNN	cascaded forward DNN
CHC	chlorohydrocarbons
COP	coefficient of performance
CPR	compressor
CV	control valve
DME	dimethyl ether
DNN	deep neural network
EEP	equal efficiency points
EVA	evaporator
EXP	expander
FFDNN	feed-forward DNN
G	generator
GM	generator-motor
GWP	global warming potential
HC	hydrocarbons
HCFC	hydrochlorofluorocarbons
HCFO	hydrochlorofluoroolefins
HE	heat exchanger
HFC	hydrofluorocarbons
HFO	hydrofluoroolefins
IEA	International Energy Agency
LCOE	levelized cost of electricity
LH	liquid heater
LM	Levenberg-Marquardt
LNG	liquefied natural gas
LTDH	low-temperature district heating
MDM	octamethyltrisiloxane
MD2M	decamethyltetrasiloxane
MD3M	dodecamethylpentasiloxane
MD4M	tetradecamethylhexasiloxane
MM	hexamethyldisiloxane
MSE	mean square error
ODP	ozone depletion potential
OFC	organic flash cycle
ORC	organic Rankine cycle

P2P	power-to-power
PCM	phase change material
PE	partial evaporator
PE-ORC	partially evaporated ORC
PFC	perfluorocarbons
PMP	pump
PRZR	pressurizer
PV	photovoltaic
RC	Clausius-Rankine cycle
RMSE	root mean squared error
SHE	supercritical heat exchanger
SIC	specific investment cost
SUP	superheater
sup-ORC	superheated ORC
TES	thermal energy storage
TFC	trilateral flash cycle or trilateral ORC
TPC	transcritical power cycle or transcritical ORC
VAP	vaporizer

1

Introduction

1.1. Background and motivation

An industrial revolution and subsequent technological advancements have significantly enhanced the quality of human life by introducing innovations that have led to increased productivity, improved health care, and a higher standard of living. However, these developments have also had unintended consequences for the environment [1]. The intensive use of natural resources required to fuel industrial machinery and produce goods has led to their depletion and degradation. Furthermore, the rising emissions of greenhouse gases that are a contributing factor to climate change and global warming are a result of the dependence on fossil fuels for energy [2]. These dual impacts highlight the complex relationship between technological progress and environmental sustainability, emphasizing the need for more sustainable practices as technological advancement continues. Therefore, in this case, an essential aspect of transitioning to sustainable energy involves achieving climate target goals, reducing dependence on fossil fuels, and aligning with Sustainable Development Goal 7 [3]. This shift involves developing and adopting renewable energy sources (e.g., solar, wind, and others), which produce minimal greenhouse gas emissions. Alongside the growth of electricity generation through photovoltaic and wind turbine power systems, tapping into reliable low and medium-temperature heat sources is also crucial [4]. These heat sources include low enthalpy geothermal heat, ocean thermal energy, solar thermal energy, biomass combustion, and waste heat. Despite the fact that these heat sources may be intermittent and fluctuating, they can still be harnessed effectively with well-designed thermodynamic cycles.

Thermodynamic cycles consist of a series of steps where a working fluid undergoes changes in its thermodynamic parameters. At the end of these steps, the working fluid returns to its original state, meaning the conditions at the initial and end of the cycle are the same. These cycles can serve to convert heat into work and power (i.e., power-generating cycles) or power into heat (i.e., refrigeration cycles or heat pumps) [5]. In a general thermodynamic cycle, the net work (W) performed over one cycle can be calculated using the first law of thermodynamics, which can be represented as a closed path integral over the state changes, as shown in Eq. 1.1. Since the cycle returns to its initial state by the end, the integral of the change in the internal energy equals zero, $\oint dU = 0$, reflecting the initial and the final thermodynamic states are identical. Moreover, the second law of thermodynamics, when applied to reversible processes, described that the integral of the heat transfer is equal to the integral of temperature times the change in entropy ($\oint dQ = \oint T ds$). Therefore, the net-specific work for one cycle can be described using Eq. 1.2.

$$W = \oint p\,dV = \oint dU - \oint dQ \tag{1.1}$$

$$W = \oint T ds \tag{1.2}$$

Furthermore, the Carnot cycle is an excellent representation of an ideal thermodynamic cycle that provides the maximum efficiency limit for how a classical heat engine can convert heat into work. The cycle is characterized by four processes (see Fig. 1.1). An isothermal heat addition process 1 → 2 at the upper temperature (T_h), then followed by the expansion process 2 → 3 (assumed as an isentropic process). Then, the heat is rejected to the sink at a lower temperature (T_c) in the process 3 → 4. After that, the system is followed by the isentropic compression process 4 → 1 to make it a closed loop cycle. It is worth noting that the Carnot cycle assumes the presence of infinitely large heat reservoirs for both heat source and sink, ensuring constant upper and lower temperatures (which are represented as T_h and T_c, respectively) and ignoring any variations in fluid properties. Moreover, the isothermal processes (heat addition and rejection) occur very slowly, allowing for ideal heat transfer conditions where the temperature of the working fluid matches perfectly with that of the heat source and sink. This optimal system enables no temperature gradients between the working fluid and the heat reservoirs during heat transfer stages. In this case, the efficiency of the Carnot cycle can be estimated using Eq. 1.3.

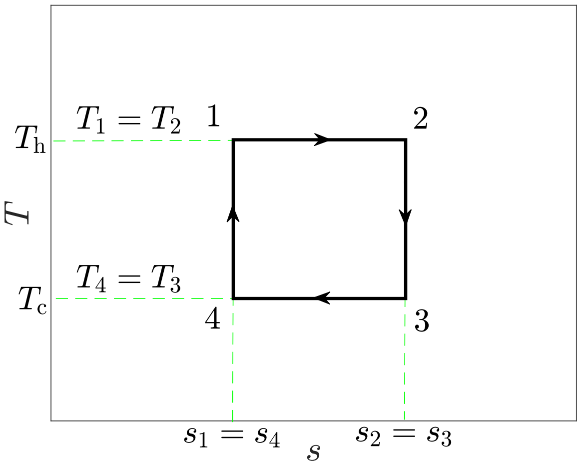

Fig. 1.1. A Carnot cycle as an excellent representation of an ideal thermodynamic cycle demonstrated by a Carnot heat engine in a $T - s$ diagram. This figure also illustrates the operation of the Carnot cycle with the isothermal heat addition process 1 → 2, isentropic expansion process 2 → 3, isothermal heat rejection process 3 → 4, and isentropic compression process 4 → 1.

$$\eta_{\mathsf{Carnot}} = \frac{|W|}{Q_{\mathsf{in}}} = \frac{\oint T ds}{\int_1^2 T ds} = \frac{T_{\mathsf{h}}(s_2 - s_1) + T_{\mathsf{c}}(s_4 - s_3)}{T_{\mathsf{h}}(s_2 - s_1)} = 1 - \frac{T_{\mathsf{c}}}{T_{\mathsf{h}}} \tag{1.3}$$

Several viable thermodynamic cycles exist, including a gaseous external heated Brayton cycle, supercritical cycle, transcritical power cycle (TPC), and subcritical power cycles, which are illustrated in Fig. 1.2, highlighting a comparison of these thermodynamic cycles using typical wet working fluid under ideal conditions in the $T - s$ diagram. Thermodynamic cycles consist of a series of steps that are almost similar components (referring to Fig. 1.2(a)), but a working fluid inside the cycle undergoes changes in different thermodynamic parameters and operation processes. The processes 1 $\rightarrow$ 2 and 3 $\rightarrow$ 4 involve isobaric (constant pressure) heat exchange taking place in the evaporator and condenser, respectively. In addition, process 2 $\rightarrow$ 3, which is an expansion process, and process 4 $\rightarrow$ 1, which is a pressurizing process, are typically assumed to be isentropic. An isobaric heat exchange might also be isothermal, particularly when a two-phase heat exchange occurs and the state of the working fluid transitions from liquid to vapor under the saturation curve (typically for pure working fluids). An example of such a subcritical cycle is the Clasius-Rankine cycle (RC), which operates with water as the working fluid. This RC represents an innovative technology used in conventional power plants, which are fueled by nuclear and coal. If the upper temperature is not sufficiently high to produce high-pressure steam to drive the turbine, organic substances can be used instead of water. In this case, the thermodynamic process is known as an organic Rankine cycle (ORC). While the basic thermodynamic steps of the RC and ORC are similar, the details in thermodynamic properties can vary significantly. This variation is primarily due to the differences in the $T - s$ diagram, which depend on the specific organic substances chosen for the ORC.

The development of ORC technology began in 1885 with the creation of the first solar-driven ORC system [10]. Since that time, ORC technology has advanced significantly and has successfully entered the commercial market, gaining considerable traction during the energy crisis of the 1970s [10]. Since then, over four gigawatts of ORC capacity have been installed across more than 2,600 plants worldwide [11]. Research into ORC technology has seen a significant increase since the early 2000s [12]. Among several thermodynamic cycles, an ORC might stand out as a viable solution as it is operating below the critical point of working fluid which the equipment does not need to withstand extreme pressure and temperatures. Unlike a conventional RC of a steam power plant, ORC offers advantages such as a wider range of operating temperatures, greater flexibility, compactness, automation, and integration [13, 14, 15]. These benefits can be achieved by employing organic working fluids instead of water in the cycle, and the thermal properties of the working fluids influence the performance of the system. An article [9] reported that ORC likely bridges the gap between smaller high-temperature operations like Stirling engines or thermoelectric devices and larger-scale steam cycles that demand higher temperatures and larger facilities, which is illustrated in Fig. 1.3. Moreover, to efficiently utilize intermittent and fluctuating heat sources, ORC systems can be integrated with thermal energy storage (TES). Several possible configurations of ORC systems with TES are detailed in [14, 16]. In addition, the sizing of the TES parameter is crucial for determining the ratio of TES mass to working fluid in the evaporator of ORC [17, 18].

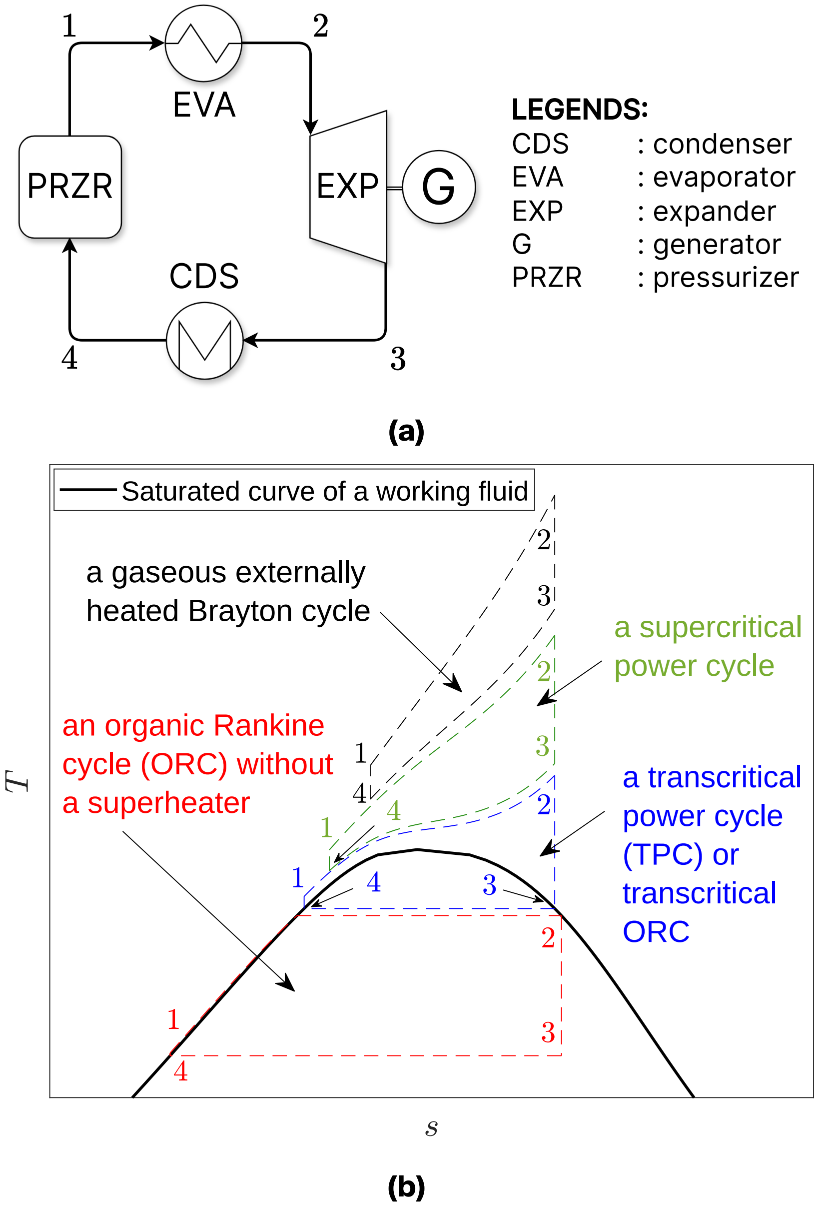

Fig. 1.2. An illustration of selected thermodynamic cycles: a gaseous externally heated Brayton cycle, a supercritical power cycle, a transcritical power cycle (TPC), and an organic Rankine cycle (ORC) **(a)** in simplified design and **(b)** a comparison of operating conditions using typical wet working fluid in a $T-s$ diagram, adapted from [6]. This diagram illustrates the operation of each cycle under ideal conditions, featuring isobaric heat exchanger process $1 \rightarrow 2$ for the evaporator, isentropic expansion process $2 \rightarrow 3$, isobaric heat exchanger process $3 \rightarrow 4$ for the condenser, and isentropic pressurizing process $4 \rightarrow 1$. It is worth noting that the condenser temperature of the TPC can be set similarly to the condenser temperature used in the ORC system. Moreover, it is important to note that in some articles [7, 8, 9], the TPC is described as a transcritical ORC system, therefore, it can be classified as part of configured ORC systems.

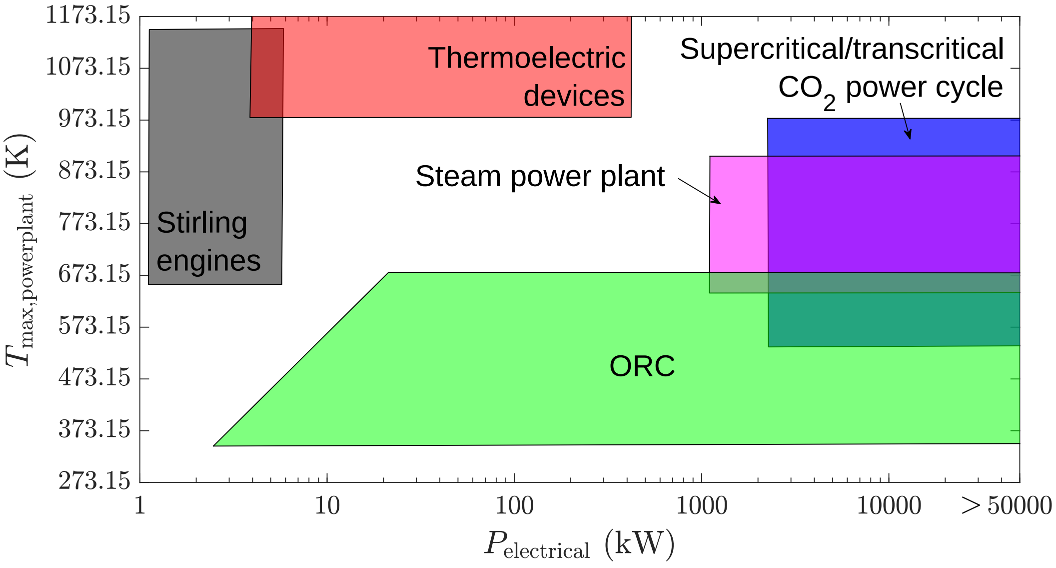

Fig. 1.3. Possible application ranges of various technologies for thermal energy harvesting in $T_{\text{max,power plant}} - P_{\text{electrical}}$ diagram, adapted from [9].

A recent study [11] has assessed around 2,900 projects from over thirty manufacturers, providing insight into the trends and development of the market across different applications, geographic regions, plant installations, capacities, and manufacturers. It reported that the market for ORC technology has seen significant growth, with a 40% increase in the number of installed plants, adding up to 861 new installations. The list of some ORC systems installed globally can be found at `https://orc-world-map.org` [19]. The current state of the ORC market seems strong, but the high cost of investment remains an obstacle, making it challenging to achieve a short payback period for different applications (which is crucial for its broader industrial adoption). Therefore, several efforts are required to enhance the ORC system in terms of technological advancements, cost-effectiveness, and efficiency improvements. Various configurations of ORC systems offer different cycle efficiency. It is essential to understand how each component and cycle operating condition impacts the cycle efficiency.

1.2. The state-of-the-art

Table 1.1 provides an overview of the results of several experimental tests that were carried out on configured ORC systems with temperature heat sources below 373.15 K. This table shows several types of expanders employed in various ORC systems, such as ORC with a separator, ORC with a recuperation, partially evaporated ORC (PE-ORC), and ORC with a superheater.

A separator used in the ORC system is used for separating the liquid and vapor phases of the working fluid, ensuring that only vapor enters the turbine. In addition, recuperation is employed after the expansion process when significant temperature differences remain. This technique uses the residual heat from the expander output to preheat the working fluid prior to the evaporation process, enhancing the overall thermal efficiency of the cycle.

Table 1.1. A list of experimental ORC studies with heat source temperature below 373.15 K, adopted from [20]. The list is continued on the next page.

Year	Type	Working fluids	Type of expanders	T_{hs} (K)	η_{EXP} (-)	$\dot{W}$ (kW)	η_{ORC} (-)
1994 [21]	sup-ORC	R134a	hermetic scroll	353.15	0.60	3.3	n.a.
2001 [22]	ORC with separator	n-Pentane	radial turbine	366.15	0.50	1.5	0.04
2006 [23]	ORC with separator	n-Pentane and HFE-301	radial turbine	n.a.	0.85	1.5	0.07
2007 [24]	sup-ORC	R134a	scroll (open drive)	338.15-343.15	0.65	2.05	0.04
2009 [25]	sup-ORC	R134a	scroll (open drive)	313.15-349.15	0.29	n.a.	0.11
2010 [26]	sup-ORC	R245fa	rolling-piston	333.15-363.15	0.45	1.64	0.04
2011 [27]	sup-ORC with recuperation	R245fa	scroll	323.15-363.15	0.80	n.a.	0.09
2013 [28]	sup-ORC	R227ea	radial turbine	339.15-384.15	n.a.	3.98-6.91	0.03-0.05
2014 [29]	sup-ORC	R601a	vane	338.55-357.25	n.a.	0.02-0.07	0.02
2014 [30]	sup-ORC	R152a	screw	332.45-332.95	n.a.	0.10-0.58	n.a.
2014 [31]	sup-ORC	R134a	screw	328.65-339.15	0.68	0.18-8.65	0.01-0.05
2015 [32]	sup-ORC	R123	vane	313.15-363.15	0.67-0.70	n.a.	n.a.
2015 [33]	sup-ORC	R123	vane	318.15-358.15	0.17-0.58	n.a.	n.a.
2016 [34]	sup-ORC	HFE7000	vane	318.55	0.58	0.15	0.04
2016 [35]	sup-ORC	R404a	hermetic scroll	338.15-373.15	0.85	3.00	0.05
2016 [36]	sup-ORC	TY1	screw twin	340.95-363.05	0.49-0.72	0.72-6.50	n.a.

Table 1.1. *(continued).*

Year	**Type**	**Working fluids**	**Type of expanders**	T_{hs} (K)	ηEXP (-)	$\dot{W}$ (kW)	ηORC (-)
2016 [37]	sup-ORC	R245fa and HFE7100	single-stage axial turbine	<373.15	0.59	1.03-1.98	0.04
2017 [38]	sup-ORC	R245fa	scroll	323.15-353.15	n.a.	0.08-0.41	0.04
2017 [39]	sup-ORC	R245fa	turbo-expander	n.a.	0.15-0.33	0.65-0.70	n.a.
2018 [40]	sup-ORC	n.a.	scroll	353.15-393.15	n.a.	0.30-1.30	0.05
2019 [41]	sup-ORC	R245fa	radial inflow turbine	n.a.	0.76-0.80	35.03-36.04	n.a.
2019 [42]	sup-ORC	R123	scroll	363.15-423.15	0.43	0.06-0.12	n.a.
2020 [43]	sup-ORC	R245fa	scroll	339.15-423.15	n.a.	0.11-1.88	n.a.
2020 [44]	sup-ORC	R123	single screw	n.a.	0.22-0.47	1.10-6.48	n.a.
2020 [45]	sup-ORC	R123	multi-vane	312.30-344.65	0.66-0.69	0.11-0.24	0.04-0.08
2021 [46]	sup-ORC	R245fa	radial inflow turbine	n.a.	0.53-0.88	7.04-17.30	0.12-0.16
2021 [47]	sup-ORC	R1233zd	multi-vane	n.a.	0.30-0.80	up to 3.00	0.02
2021 [48]	sup-ORC	R245fa	scroll (oil-free)	367.65-368.15	0.38-0.80	0.10-0.60	0.04
2021 [49]	sup-ORC	R245fa	radial inflow turbine	n.a.	n.a.	0.36-1.17	0.03
2022 [50]	sup-ORC	R134a	scroll	351.15-363.15	n.a.	1.22	0.07
2022 [51]	PE-ORC	mixture, HFE7000, HFE7100, and Novec649	axial turbine	363.15-373.15	n.a.	0.40-0.45	n.a.
2022 [52]	PE-ORC	R134a	reciprocating piston	313.15-348.15	0.26-0.38	0.13-1.20	n.a.

In a practical aspect, the expansion process occurs in the dry vapor conditions, also known as the superheated vapor state. Operating under this superheated vapor condition helps prevent the formation of droplets that can erode or damage turbine blades, which is often used in large-scale ORC systems. However, superheating the vapor to ensure it remains dry might lead to reduced cycle efficiency. This is because superheating requires significant additional heat to fully evaporate the working fluid until it reaches a saturated vapor state (x=1) and then heat the vapor working fluid further (in this case, the cycle is called superheated ORC or sup-ORC). As a result, the input heat increases, potentially lowering the overall efficiency of the cycle, which also depends on the properties of the working fluids used. As an alternative to sup-ORC, the pressurized working fluid can be heated until it reaches a supercritical condition. After that, it expands through the superheated state and is then condensed back to liquid form. This system is known as a transcritical power cycle (TPC), which has been illustrated in Fig. 1.2. It is worth noting that the lower temperature (i.e., the temperature of the working fluid in the condenser) of the TPC, as shown in Fig. 1.2, can be set to match the lower temperature used in the ORC system. It is also important to note that, in some articles [7, 8, 9] and other publications in the literature, the TPC is presented as a transcritical ORC system. This means that TPC can be categorized as a type of ORC system, particularly operating under transcritical conditions. In the further discussion of this dissertation, this transcritical ORC is described as TPC.

Furthermore, in the PE-ORC system, the working fluid flows through the expander in a two-phase state (vapor quality 0<x<1) rather than as superheated or saturated vapor (vapor quality x=1). The key concept of PE-ORC is to decrease the ratio of latent heat to sensible heat in the working fluid during the evaporation process. This adjustment allows for more efficient cooling heat source streams to lower temperatures, which improves the heat utilization efficiency. An alternative to PE-ORC is to arrange the working fluid to pass through the expander in the saturated liquid state instead of to the two-phase, superheated, or saturated vapor conditions. In this case, this system is known as a trilateral flash cycle (TFC). The main idea of TFC is to eliminate the ratio of latent heat to sensible heat in the working fluid. Therefore, an evaporation process is not needed, and the expansion process starts with the saturated liquid working fluid. This concept in TFC allows for more efficient cooling heat source streams to lower temperatures, which offers higher heat utilization efficiency compared to PE-ORC and ORC. It is worth noting that in some articles [9, 53], TFC is described as trilateral ORC. Therefore, TFC can be categorized as a type of configured ORC system.

Fig. 1.4 shows the various operational conditions of different ORC system configurations, including basic ORC (without a superheater), sup-ORC, PE-ORC, TFC, and TPC, illustrated on a $T-s$ diagram. The sup-ORC, ORC, PE-ORC, and TFC systems operate under subcritical conditions, either in terms of pressure or temperature, and can be categorized as subcritical ORC systems. On the other hand, the TPC operates partly in supercritical conditions, with the working fluid transitioning from supercritical to subcritical during the cycle.

Despite the maturity of ORC technology in certain applications, there remains a knowledge gap and potential for further development and advancement. Given this

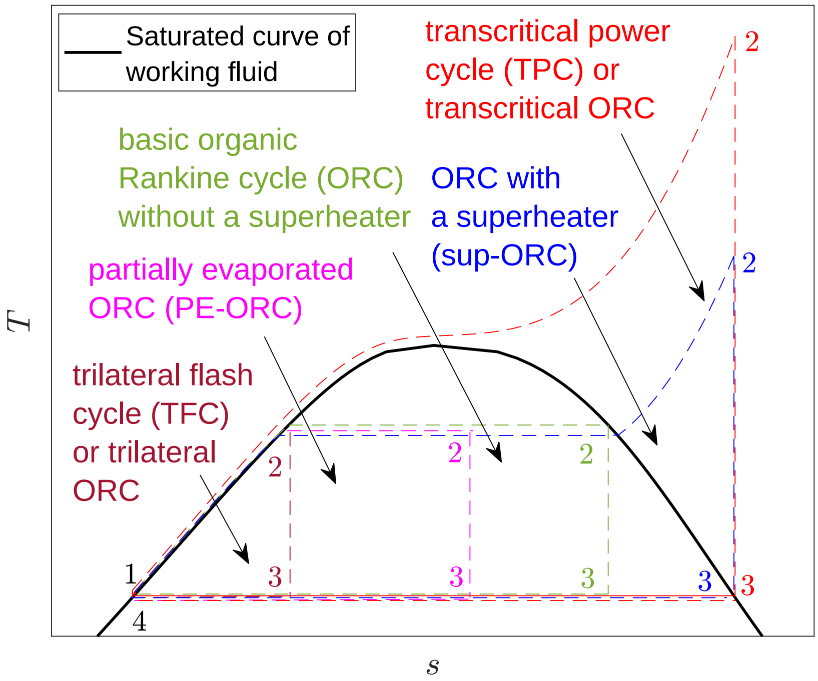

Fig. 1.4. An illustration of different ORC systems under subcritical and transcritical operating conditions in a $T-s$ diagram, using a wet working fluid. Several types of ORC systems operating under subcritical operating conditions include ORC without superheater, ORC with superheater (sup-ORC), partially evaporated ORC (PE-ORC), and trilateral flash cycle (TFC). The configured ORC system operating under transcritical operating conditions refers to the transcritical power cycle (TPC). It is important to note that in some articles [9, 53], TFC is described as trilateral ORC. Some articles [7, 8, 9] mentioned that TPC is a transcritical ORC. Therefore, both TFC and TPC can be categorized as types of ORC systems. This diagram illustrates the operation of each cycle under ideal conditions, featuring isobaric heat exchanger process $1 \rightarrow 2$ for the evaporator, isentropic expansion process $2 \rightarrow 3$, isobaric heat exchanger process $3 \rightarrow 4$ for the condenser, and isentropic pump process $4 \rightarrow 1$.

situation, it is still essential to conduct more research on how ORC can efficiently utilize intermittent and fluctuating heat sources [13, 14, 15]. Both PE-ORC and TFC systems have been the subject of a few numerical and experimental studies that can improve heat source utilization efficiency. Based on the literature studies and the author's knowledge, it seems that these promising PE-ORC and TFC technologies have not been as extensively investigated and explored. Therefore, theoretically exploring the efficiency of the ORC system under subcritical and transcritical operating conditions mentioned above, considering the operating condition of the low-boiling working fluid expansion process, could be promising, which is one of the state-of-the-art in this dissertation.

In ORC systems, the expansion process is crucial, as it involves the working fluid expanding and driving the shaft of the expander. TA generator that generates power is attached to this shaft. The types of expansion machines used in ORC systems are illustrated in Fig. 1.5. In larger ORC systems, turbines (radial and axial) are commonly used as expanders, while smaller setups often use volumetric expanders. These configurations are also found in several experimental ORC setups listed in Table 1.1. Volumetric expanders are particularly well-suited for use in ORC when it comes to utilizing energy from low-grade heat sources [54, 55]. These volumetric expanders are designed for use even under two-phase flows, which are usually avoided in turbines due to issues like erosion and condensation.

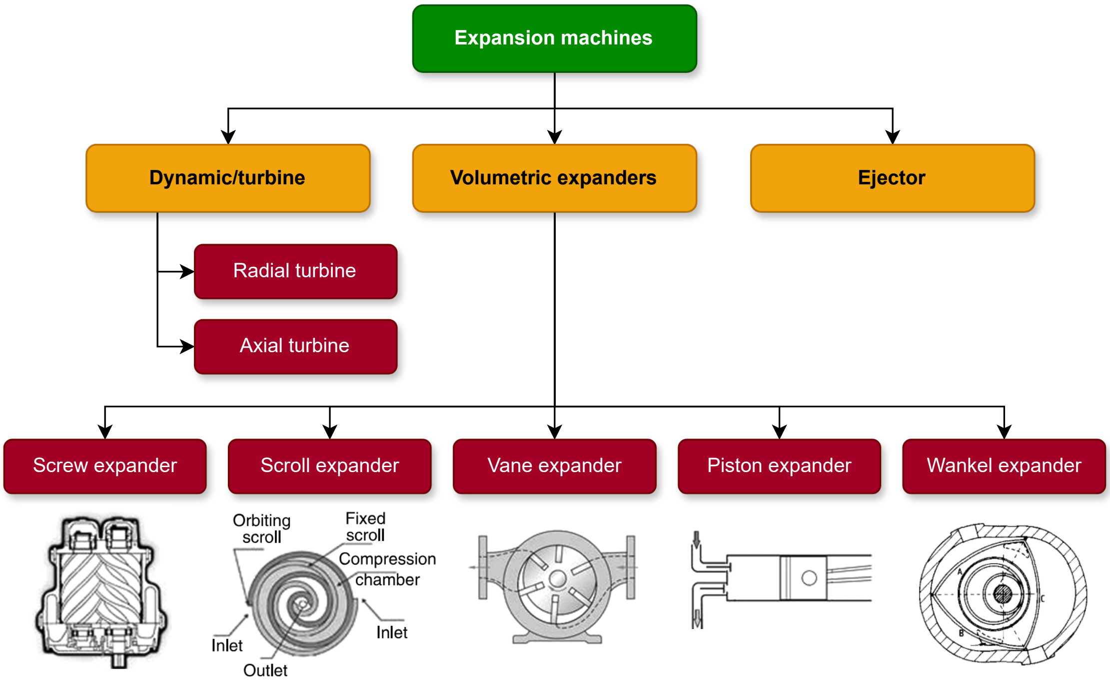

Fig. 1.5. A classification of expansion machines, including the classification of volumetric expanders, adapted from [56, 57].

Table 1.2. The comparison of operating conditions in selected types of volumetric expanders tested in ORC system, adapted from [58].

Volumetric types	p_{in} (MPa)	p_{out} (MPa)	$p_{\text{in}}/p_{\text{out}}$ (-)
Screw	1.5 – 1.6	0.1	16
Scroll	1	0.1	10
Multi-vane	0.7	0.1	10
Piston	20	0.1	200
Wankel [59, 60]	3	0.1	1.2-6

There are several types of volumetric expanders available, including screw, scroll, vane, piston, and Wankel expanders, which are illustrated in Fig. 1.5. The operation of these machines has been described in [56, 57, 61]. The operating conditions in these volumetric expanders are listed in Table 1.2. Moreover, these volumetric machines can be further classified into two types: reciprocating and rotary volumetric expanders. Their operating conditions can be analyzed using a $p - V$ diagram, and the technical work generated can be calculated using the relation $W = \int V dp$. Moreover, the volumetric expanders typically operate through a series of phases under the ideal condition: isobaric filling (process 1 → 2 where p, T=constant), expansion (process 2 → 3 where pV^{κ}=constant), and isobaric evacuation/discharge (process 3 → 4 where p, T=constant), as illustrated in $p - V$ diagram in Fig. 1.6. The specific heat at constant volume divided by the specific heat at constant pressure is represented by the symbol κ. In some cases, volumetric expanders may experience internal leakage, which can lead to an unintended compression process 4 → 1, affecting performance. These series phases are determined by specific design features of the machines. For rotary machines, these features include the working chamber's geometry, the rotor, and the stator. For reciprocating machines, they include the cylinder. Other common design elements influencing performance are internal leakage, internal friction, the lubrication system, as well as noise and vibration levels. These elements help define the operational capabilities of the machine. Pressure and volume are crucial parameters in designing volumetric expanders.

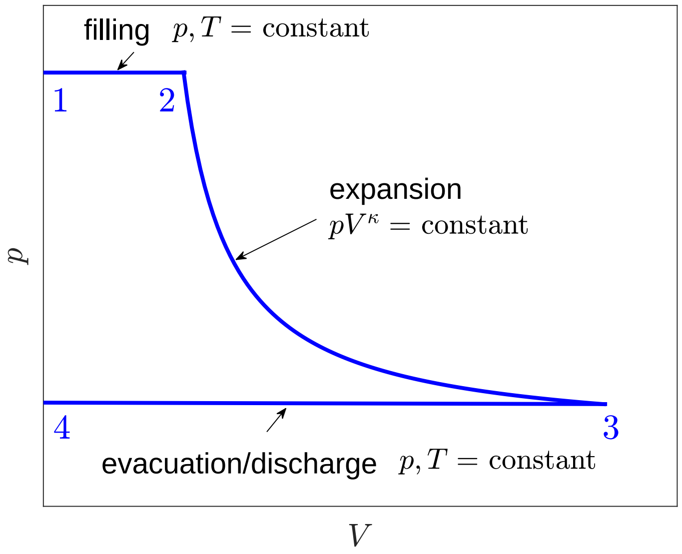

Fig. 1.6. A series of typical operation in the volumetric expanders in a $p - V$ diagram: isobaric filling process 1 → 2 (p, T=constant), expansion process 2 → 3 (pV^{κ}=constant), and isobaric evacuation/discharge process 3 → 4 (p, T=constant). If the volumetric expander experienced the internal leakage, the compression process 4 → 1 (pV^{κ}=constant).

Since some ORC systems, such as PE-ORC and TFC, may operate under two-phase conditions, using a volumetric expander in these systems could be promising. A preliminary study [58] has highlighted that typical rotary volumetric machines (e.g., screw, scroll, and vane) are more likely to be adapted for two-phase fluids undergoing phase changes. In contrast, reciprocating machines, like piston expanders, are less commonly used but might not be ideal for PE-ORC due to the risk that low boiling working fluid, in its liquid form, might dissolve the oil film, potentially damaging the cylinder and piston rings [62]. Some review articles [63, 64] have reported that two-phase volumetric expanders show potential as technologies for low-temperature heat-to-power cycles. The TFC, in particular, demonstrates a greater net output power, improved efficiency in heat source utilization, and higher exergy efficiency compared to a basic ORC system.

In literature study, several researchers have conducted experimental investigations on two-phase volumetric expanders [58, 63, 64]. The results suggest that a two-phase volumetric expander can offer a wider operating range of ORC systems designed to harvest energy from low-grade heat sources. Therefore, part of this dissertation also described the experimental investigation of the two-phase volumetric expander in the ORC system. Table 1.1 presents several volumetric expanders tested under both superheated and two-phase conditions. However, only a limited number of volumetric expanders have been utilized in micro-ORC systems that harness low-grade heat sources below 373.15 K. Given the potential of rotary volumetric machines to operate under two-phase conditions, this dissertation focuses on a multi-vane volumetric expander as a rotary-type expander for the ORC system analysis. The research on ORC systems using multi-vane expanders has been ongoing at the Department of Thermodynamics and Renewable Energy Sources at Wrocław University of Science and Technology since 1996 [65]. Moreover, the multi-vane expander offers lower maintenance requirements and a compact design compared to other rotary volumetric expanders. Therefore, to continue this line of research in this department, the multi-vane expander is selected. In this context, since there is a lack of investigation into the two-phase expander, experimentally investigating the performance of the two-phase multi-vane volumetric expander in ORC systems with heat sources below 373.15 K represents a state-of-the-art contribution to the scientific field.

1.3. Aim and objectives

The core of this dissertation analyzes the expansion process of low-boiling working fluids and its impact on the efficiency of various ORC configurations. This study aims to describe the efficiency variations of different ORC systems attributable to different working fluids and thermodynamic conditions influenced by the expansion process. Moreover, an experimental study focuses on a two-phase volumetric expansion system, employing artificial intelligence (AI) to predict the wet isentropic efficiency of the expander. This innovative approach seeks to redefine efficiency benchmarks for ORC systems and contribute to the state of the art in thermodynamic power cycles. A significant portion of this dissertation is dedicated to potential volumetric expanders in various ORC configuration systems. Given the suitability of volumetric expanders for ORC systems operating at low to medium temperatures and pressures, this could revolutionize the design of the ORC system for intermittent and fluctuating heat sources. The main objectives of the research are outlined as follows:

1. To analyze the influence of the low-boiling working fluid expansion process on the efficiency of different ORC systems under subcritical operating conditions for volumetric expanders,
2. To analyze the influence of the low-boiling working fluid expansion process on the efficiency of different ORC systems under transcritical operating conditions for volumetric expanders,
3. To evaluate and compare the efficiency variations in different ORC systems

influenced by different working fluids under subcritical and transcritical operating conditions for volumetric expanders,

4. To experimentally validate the isentropic efficiency of a low-boiling working fluid expansion process in an ORC system using a volumetric expander operating under two-phase conditions by using AI predictions, and
5. To analyze the adaptability and benefits of implementing volumetric expanders in different ORC systems.

1.4. Outlines of the dissertation

This dissertation consists of six main chapters that are structured in the following way. In Chapter 1, the introduction outlines the background and motivation behind this study. It also details the current state of the art, as well as the specific aims and objectives of the research. Then, the following chapters represent the contribution of the research. Each chapter systematically presents the research, beginning with a brief introduction, followed by methodology with some boundary conditions, discussion, main contributions, and concluding with the thesis points that encapsulate the research findings.

Chapter 2 describes the brief historical aspect and classification of low-boiling working fluids. In addition, it introduces the methodology of thermodynamic modeling simulation, which employs several types of working fluids. The focus of this chapter delves into the theoretical analysis of the low-boiling expansion process influencing the cycle efficiency of different ORC systems under subcritical operating conditions. Moreover, the cycle efficiency comparison of the different ORC systems influenced by different types of working fluid is described.

Furthermore, Chapter 3 extends the theoretical analysis of the low-boiling expansion process influencing the cycle efficiency of various ORC configuration systems. In addition, it compares the ORC system under subcritical and transcritical operating conditions. Also, the cycle efficiency comparison of different ORC systems influenced by different types of working fluid is described.

Chapter 4 reports an experimental study of a volumetric expander in an ORC system operating under two-phase conditions. It describes several components and some measurement systems used in the experimental study. This chapter also discussed the application of AI for predicting the isentropic efficiency of the expander.

In Chapter 5, various applications of the different ORC systems employing a volumetric expander are examined, highlighting selected thermodynamic issues. It expands the scope of the dissertation by exploring real-world applications and implications of the research.

In the end, Chapter 6 concludes with a comprehensive summary, highlighting the key findings and some main contributions of the research. This concluding chapter offers a reflective overview of the entire dissertation, emphasizing its significance and potential impact on the field of thermal power generation. Moreover, some future directions for research on this topic are described.

The publications by the author that are related to this chapter are [6, 13, 14, 15, 16, 17, 18, 20, 58].

2

Analysis of the low-boiling working fluid expansion process influencing the efficiency of selected different ORC systems under subcritical operating conditions

A steam-based RC serves as a foundation model for all ORC systems as an example of a subcritical thermodynamic cycle that utilizes typical wet working fluid. The operation of this cycle has been described in the prior chapter. Its widely recognized model provides an effective means to explore how different working fluids and operating conditions changes can impact the cycle efficiency of the system. Furthermore, another kind of subcritical cycle, a TFC system, has been introduced [66]. The TFC is characterized by the expansion process beginning from a saturated liquid state (vapor quality x=0). Several studies have reported that the RC and ORC may outperform TFC in terms of cycle efficiency [67] and other performances [68]. However, under specific conditions, TFCs can generate more output power [69, 70], achieve higher heat source utilization [71], and offer higher exergy efficiency [72, 73] than ORCs.

ORC systems operate with fully dry vapor at the inlet of an expander, meaning the vapor is either in a saturated state with a vapor quality x=1 or in superheated conditions. However, an incomplete evaporation process may arise from the use of intermittent and fluctuating heat sources. Then, the expander works under wet or two-phase conditions (i.e., the vapor quality is in the range of 0<x<1). This condition leads to a transition from a wet-to-dry cycle (a transition cycle between TFC and ORC), known as a partially evaporated ORC (PE-ORC). A maximum cycle efficiency of ORCs was observed in an article [74] that compared the cycle efficiency of ORCs and TFCs using various kinds of working fluid types. However, the study of PE-ORC was not carried out. Given this context, there is a lack of clarity regarding the cycle efficiency comparison between ORC, PE-ORC, and TFC.

This chapter addresses a notable research gap in the literature concerning the limited studies on TFC and PE-ORC, which are categorized as part of configured ORC systems. Assuming the heat sink temperature remains constant, the principles of the Carnot cycle suggest that any power generation may enhance its cycle efficiency by raising the heat source temperature. This chapter aims to theoretically prove that the PE-ORC, functioning as an intermediate cycle between the ORC and TFC, consistently achieves cycle efficiency between those of the ORC and TFC across various working fluids, with increasing operating temperatures and pressure ranges of the expander resulting in higher cycle efficiency. This part of the dissertation described in this chapter demonstrates and explores how different low-boiling working fluid expansion processes affect the cycle efficiency of different ORC systems (basic ORC, PE-ORC, TFC) under subcritical operating conditions considering vapor quality to the inlet of the expander.

2.1. Brief historical aspect of working fluids

Hundreds of organic substances taken from chemical classes such as hydrocarbons (HC), perfluorocarbons (PFC), chlorofluorocarbons (CFC), hydrochlorofluorocarbons (HCFC), hydrofluorocarbons (HFC), hydrofluoroolefins (HFO), hydrochlorofluoroolefins (HCFO), ethers, alcohols, and siloxanes are available as potential working fluids instead of water for thermodynamic power cycles. Several substances, including refrigerants and working fluid mixtures, could also be promising. Fig. 2.1 shows an overview of the historical usage of working fluids.

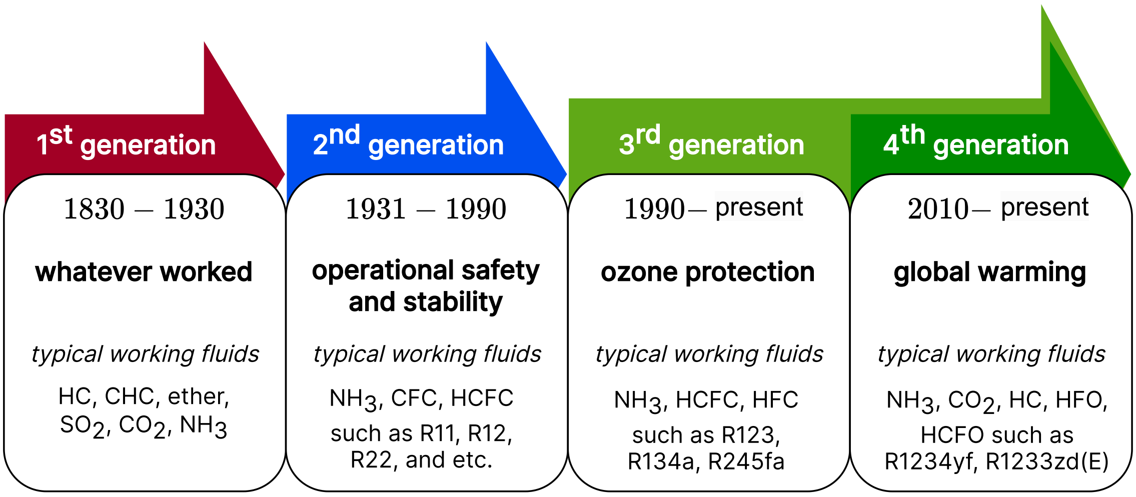

Fig. 2.1. Brief historical aspect of working fluids as an alternative to water used in various applications categorized by generations, adopted from [75].

The development of refrigerants has progressed through several generations, each marked by advancements in safety, environmental impact, efficiency, and other vital parameters [76]. Initially, the first generation of working fluids included hazardous and combustible substances like chlorohydrocarbons (CHC) and sulfur dioxide, alongside natural refrigerants such as carbon dioxide, HCs, and ammonia. The second generation introduced CFCs (like R11 and R12) and HCFCs (such as R22). These substances gained popularity due to their effectiveness, ease of handling, and safety concerns (e.g., non-toxic and non-flammable). However, in the 1970s, the significant ozone depletion potential (ODP) of these refrigerants was recognized. This concern led to the phase-out of many working fluids containing fluorine and chlorine under the Montreal Protocol in 1987 [77]. In that case, new solutions were developed with HFCs as the third generation, with R245fa and R134a being notable examples. HFCs have zero ODP but contribute to global warming more significantly than carbon dioxide, for which, in the 1990s, global warming became a threat.

Furthermore, the Kyoto Protocol in 1997 [78] identified HFCs as critical greenhouse gases, setting reduction targets for their emissions. The fourth generation of working fluids has recently been developed, including HFOs and HCFOs like R1233zd(E) and R1234yf. These refrigerants combine the benefits of minimal or no ODP and low global warming potential (GWP) with good thermodynamic properties. In addition, there has been a growing interest in using HC and carbon dioxide due to their environmental benefits.

2.2. Classification of working fluids

In a conventional approach, the classification of working fluid depends on the characteristic shape of the saturation curve (i.e., a bell-shaped curve) on a $T-s$ diagram, which is related to the vapor condition after it has been expanded in the expander employed in the ORC system. The working fluids could be classified into three different types: wet, dry, and isentropic, which are described as follows [79]:

- When an isentropic expansion occurs from a saturated vapor phase in a wet working fluid, the expansion process will end in the two-phase region. In that case, the curve representing saturated vapor for a wet fluid in the $T-s$ diagram slopes downward at every point (meaning ds/dT<0, see Fig. 2.2(a)). It indicates that as the saturation temperature decreases, the entropy of the fluid increases.
- When a similar isentropic expansion occurs in the dry working fluid, it ends up in a superheated or dry region. The curve for the saturated vapor of a dry working fluid on a $T-s$ diagram generally slopes upwards (indicating ds/dT>0, see Fig. 2.2(b), except the vicinity of the critical point.). Near the critical point, ds/dT<0 then, followed by ds/dT ≈0 and ds/dT>0 (i.e., a negative-to-positive ds/dT), can be observed.
- Originally, isentropic means that one can have an expansion process (s=constant) running all saturated vapor states because ds/dT=0 is in a finite, nonzero temperature range. Since this kind of $T-s$ diagram does not exist, therefore, ”real isentropic working fluids” can be defined, with a reverse S-shaped saturated vapor branch. With this condition, the expansion process from the saturated vapor state to other points in the saturated vapor state can be done by going through the dry vapor state (superheated conditions). In that case, the reverse S-shaped saturated vapor line can be observed in Fig. 2.2(c) showcasing ds/dT<0 from the critical point, then followed by ds/dT ≈0, ds/dT>0, ds/dT ≈0, and ds/dT<0 in sequence (i.e., a negative-to-positive-to-negative ds/dT). Moreover, the isentropic working fluid, which exists only in theory, is

also illustrated in Fig. 2.2(d). By altering the molecular complexity, it is possible to create a transition from wet to real to dry isentropic conditions [80]).

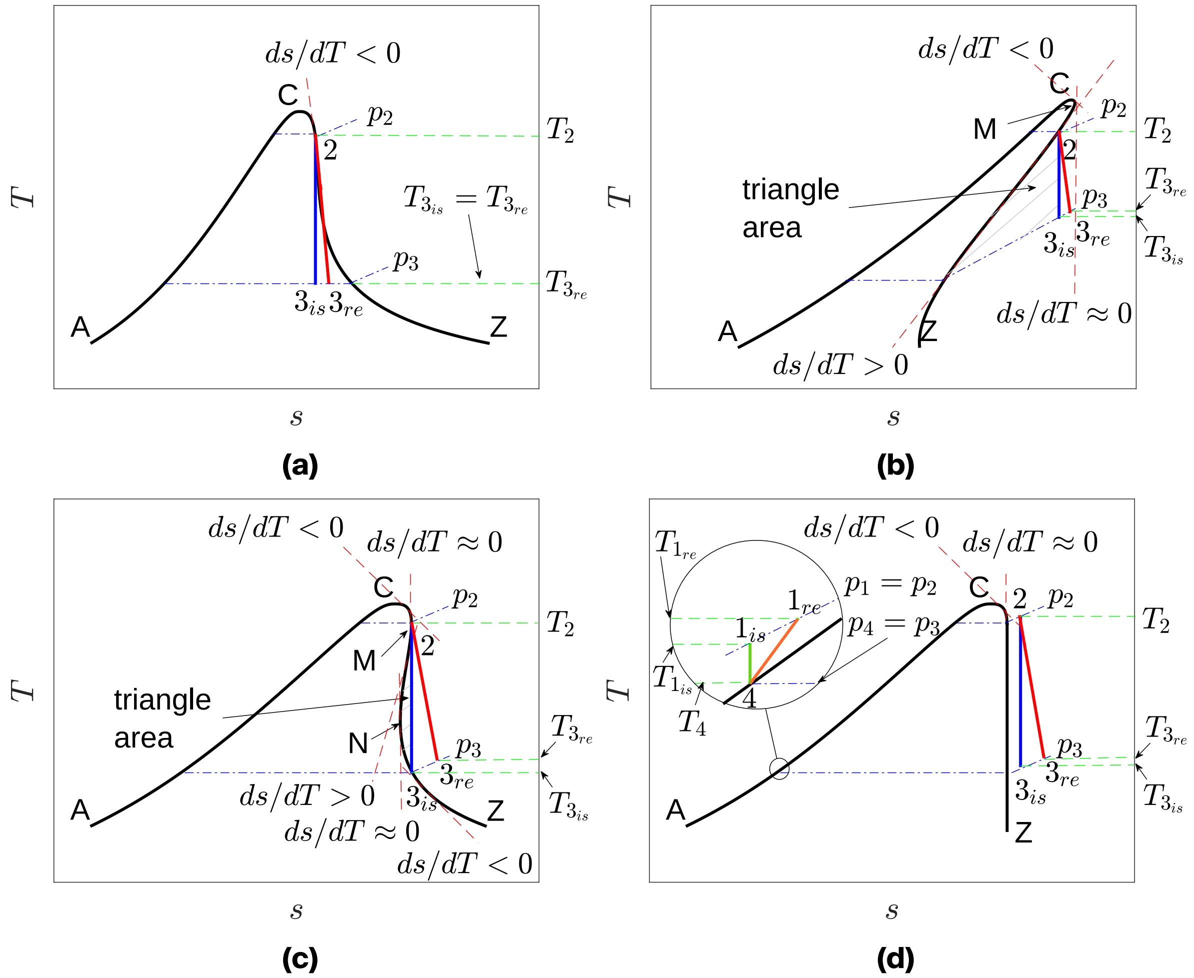

(a)

(b)

(c)

(d)

Fig. 2.2. Classification of working fluids in a $T - s$ diagram with examples of isentropic expansion processes in **(a)** a wet working fluid, showcasing ds/dT<0 along the saturated vapor line, classified as ACZ-type working fluid; **(b)** a dry working fluid, indicating ds/dT<0 from the critical point, then followed by ds/dT ≈0 and ds/dT>0 (i.e., a negative-to-positive ds/dT) along the saturated vapor line to triple point temperature (or Z point), classified as AZCM-type working fluid as an illustrative example; **(c)** an isentropic working fluid, showcasing ds/dT<0 from the critical point, then followed by ds/dT ≈0, ds/dT>0, ds/dT ≈0, and ds/dT<0 in sequence (i.e., a negative-to-positive-to-negative ds/dT), classified as ACNMZ-type working fluid as an illustrative example; and **(d)** an isentropic working fluid which exists only in theory or a negative-to-nearly zero ds/dT (changing molecular complexity can generate a wet-real isentropic-dry transition [80]). Moreover, this figure outlines novel classification methods using five points to demonstrate the potential sequences of these classifications [81, 82] or using a triangle area between saturated vapor curve and isentropic expansion path [83, 84]. The isentropic expansion process 2 → 3_{is} and the real expansion process 2 → 3_{re} are illustrated by the blue and red solid lines, respectively. The isentropic pump process 4 → 1_{is} and the real pump process 4 → 1_{re} are depicted by the green solid line and the orange solid line, respectively.

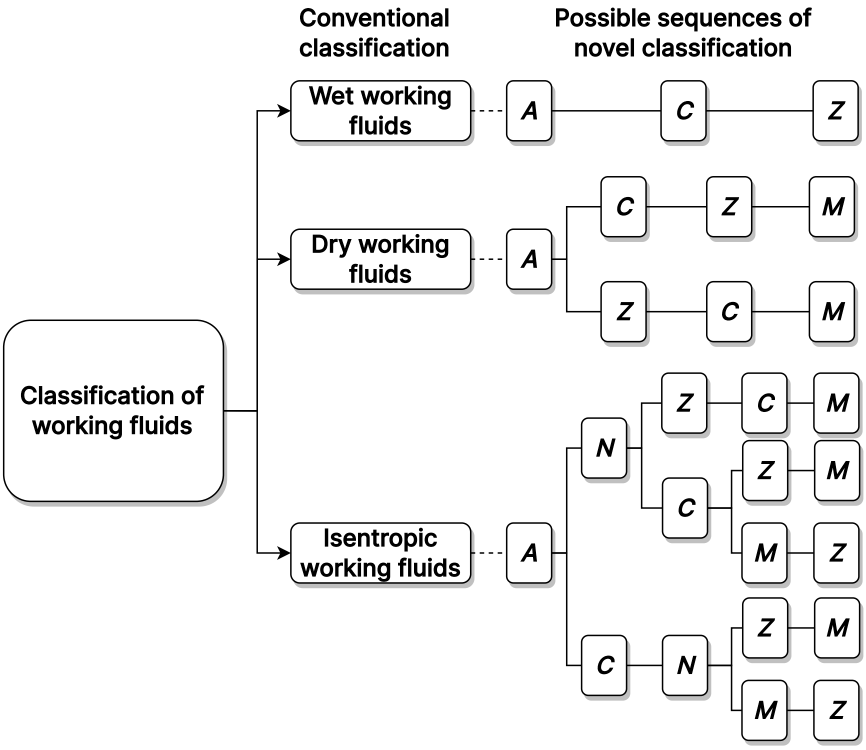

Fig. 2.3. Working fluids classified into conventional and novel categories (adapted from [81]).

Although the traditional method of classifying working fluids using the slope of the saturated vapor curve in a $T - s$ diagram can differentiate between wet, dry, and isentropic types, this approach is far from enough to distinguish between isentropic and dry working fluids accurately. Therefore, a novel method offers a more detailed classification based on sequences of entropy characteristics, outlined in five specific points [81, 82], which is depicted in Fig. 2.3. The five specific markers on the phase diagram are defined as follows. The label 'A' marker is the triple point at the intersection between the liquid and solid phases. Label 'Z' marker is the triple point found at the intersection between the solid and vapor phases. The 'C' label represents the critical point. Label 'M' and 'N' markers, which are secondary characteristic points, indicate the location on the saturated vapor curve characterized by local entropy maxima and minima, respectively. These exemplary markers are indicated in Figs. 2.2 and 2.3. Classes are marked by the sequence of these points, ordered by their entropy values, as seen in 2.2(a)-(c) as an exemplary. Theoretically, five points can be ordered in 5!=120 different ways, but for some constraints, like 'A' should be before 'C'), only eight classes can be defined (see Fig. 2.3). Moreover, by employing varying temperature ranges (with a fixed evaporating temperature and a lowered condensing temperature of the cycle), transitions of novel classification can occur within a working fluid. An example of such a fluid is butane, as described in [85]. In addition, possible paths for isentropic expansion process were investigated, starting at a specific point on the saturated vapor curve at the inlet to the expander and the isentropic expansion ending up in the saturated vapor region [85]. Two recent articles [83, 84] introduced an alternative classification method using the triangle area between the saturated vapor curve and the isentropic expansion path to categorize isentropic and dry working fluids. The illustration of the triangle area is depicted in Figs. 2.2(b) and 2.2(c). Working fluids are categorized based on the size of the triangle area: less than five kJ/kg for isentropic, between five and twenty-five kJ/kg for dry, and more than twenty kJ/kg for super dry working fluid.

2.3. Mathematical modeling simulation of selected ORC systems under subcritical conditions

This subchapter details the process and modeling simulation of different ORC systems (ORC, PE-ORC and TFC) that are investigated in this thesis. Also, it outlines the steps in the research calculations and explains the mathematical models used.

2.3.1. ORC, partially evaporated ORC, and trilateral flash cycle

An initial study theoretically examined how different working fluids and an increased operating temperature range of the expansion process affect the efficiency of ORC systems. Also, it investigated the effect on the efficiency of TFC as another subcritical power cycle, based on selected available working fluids. Subcritical thermodynamic cycles are defined as those in which all processes within the desired thermodynamic cycle operate below the critical pressure. The simplified designs of these cycles are likely to be similar, as depicted in Fig. 1.2(a). Nevertheless, their operational processes exhibit notable differences in the $T-s$ diagram, illustrated in Fig. 2.4, where ideal refers to the ideality of steps (strictly isobaric evaporator, isobaric condenser, isentropic expansion, and isentropic pump processes).

The difference between ORC, PE-ORC, and TFC lies in the condition at the beginning of the expansion process (see state 2 in Fig. 2.4). Specifically, this refers to vapor quality at an inlet to an expander, which can be in saturated vapor state (with a vapor quality x=1 or in a superheated condition for basic ORC), a two-phase condition (with a vapor quality 0<x_2<1 for PE-ORC), or a saturated liquid state (with vapor quality x_2=0 for TFC). This variation is primarily influenced by the heat exchanger process (1 $\rightarrow$ 2), such as a liquid heater and an evaporator. In this case, a liquid heater is necessary for ORC, PE-ORC, and TFC to raise the temperature of the working fluid (in pressurized liquid state) to the boiling temperature (saturated liquid phase) corresponding to the given pressure. In addition, PE-ORC and ORC systems require an additional heat exchanger, meaning the use of an evaporator to facilitate the phase change of the working fluid from liquid to vapor. For PE-ORC, the evaporator offers a partial evaporation process, resulting in a specific vapor quality with 0<x_2<1, indicating that the fluid is partially vaporized. On the other hand, in ORC systems, the evaporator ensures a complete evaporation process, achieving a saturated vapor state x_2=1, where the working fluid is completely evaporated. In many installed ORC systems, the inlet to the expander is kept to operate in superheated conditions. This necessitates using a superheater to raise the temperature beyond the point of saturated vapor. The explanation of the ORC with a superheater is described in the next chapter. It appears that the three heat exchangers are different. Having a liquid heat carrier (like thermal water), the liquid heater is a liquid-liquid type heat exchanger that needs to handle the viscous flow,

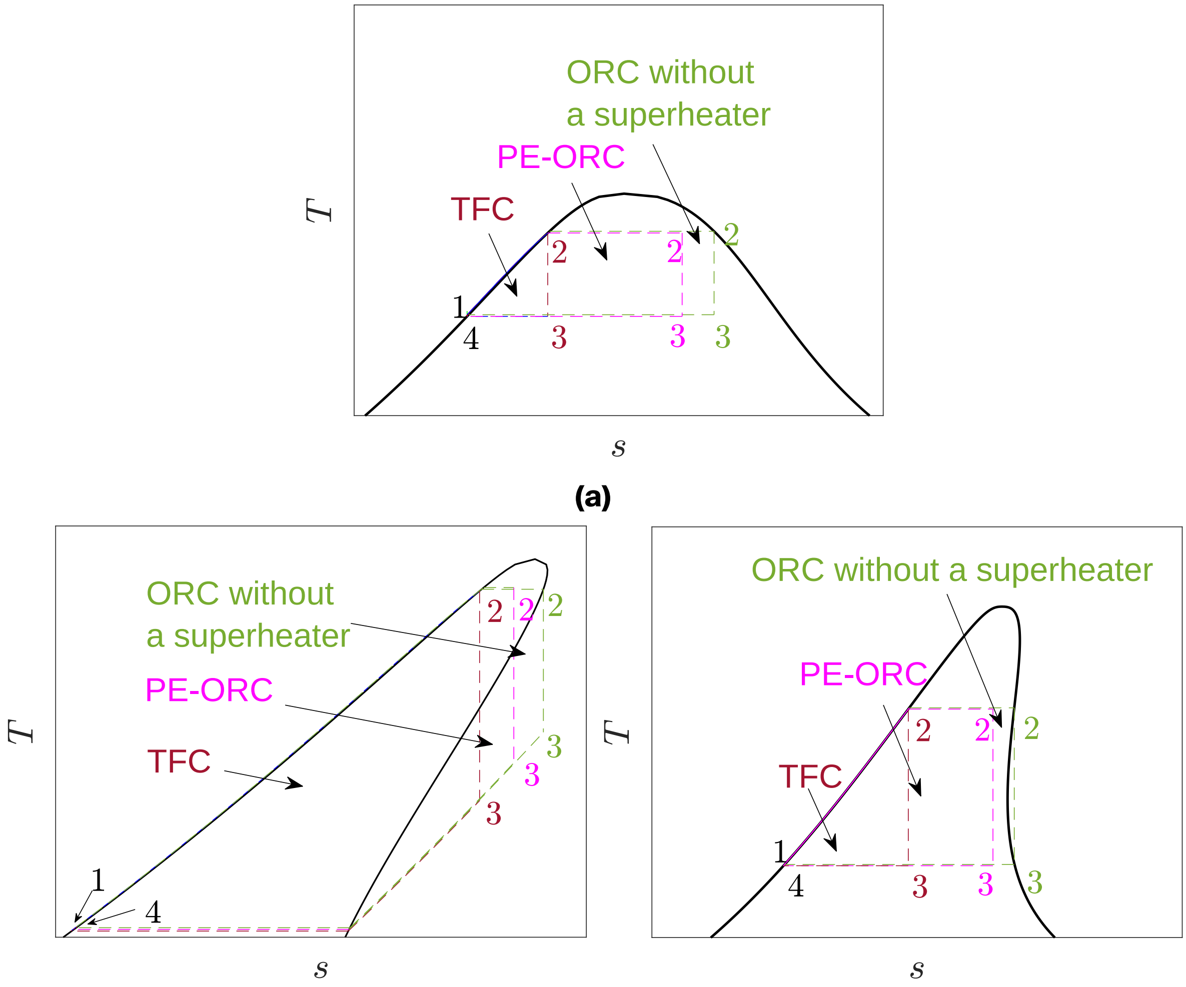

(a)

(b) **(c)**

Fig. 2.4. Selected subcritical thermodynamic cycles-basic ORC, PE-ORC, and TFC-in this investigation illustrated in typical **(a)** wet, **(b)** dry, and **(c)** isentropic working fluids in $T-s$ diagrams. These diagrams illustrate the operation of each cycle under ideal conditions, featuring isobaric heat exchanger process 1 $\rightarrow$ 2 for the evaporator, isentropic expansion process 2 $\rightarrow$ 3, isobaric heat exchanger process 3 $\rightarrow$ 4, and isentropic pump process 4 $\rightarrow$ 1.

but the size/volume and heat exchange surfaces would be relatively small. An evaporator is a different one; it needs to handle phase change, and therefore, it has to have larger dimensions.

In expanders, even when the pressure ratio and inlet temperature are kept constant, the selection of working fluid influences how the expansion process ends, as illustrated in process state 3 of Fig. 2.4 in ideal condition as an example. Using wet working fluid, similar temperatures can be expected at the end of the expansion process in ORC, PE-ORC, and TFC. However, when using dry working fluids, the state of the working fluid at the outlet from the expander is in superheated condition, but the temperature differs across all cycles, highlighting the different low-boiling working fluid expansion processes. Moreover, using isentropic working fluids typically results in comparable temperatures at the outlet from the expanders, though exceptions may exist. This exception are influenced by the slope of the saturated vapor curve, and differences become noticeable if the expansion process ends in a superheated state for ORC systems using isentropic working fluid. It is apparent and important to note that the vapor quality at the outlet from the expanders (x_3) across all cycles is different.

Furthermore, Fig 2.4 shows that the difference in state 3 of each cycle results in different paths of condensation processes to change the phase of the working fluid back into its liquid condition (state 4). In this case, cooling requirements increase from TFC to PE-ORC and reach the longest path for ORC, referring to the process 3 $\rightarrow$ 4). It is important to note that, in this context, the pumps across all cycles are likely to operate under identical pressure ratio conditions, as indicated in the process 4 $\rightarrow$ 1.

Based on the above mentioned condition, a set of modeling simulations for selected subcritical cycles could be introduced. Specifically, it details the operating temperature range within which these cycles function, which also refers to the operating temperature range of the low-boiling working fluid expansion process. For illustrative purposes, Fig. 2.5 shows the steps of modeling simulation using wet working fluid. Such an approach clarifies the operational parameters and exemplifies the application of wet working fluid in the simulation. The steps of modeling simulation in this manner are also adapted for dry and isentropic working fluids considering the operating thermodynamic processes that have been introduced in Fig. 2.4(b) and 2.4(c).

The cycle efficiencies of ORC, PE-ORC, and TFC are explored with the thermodynamic process operation defined by two parameters: an upper temperature (T_2) and a lower temperature (T_4). These parameters dictate the temperature range of the cycles, which also refers to the operating temperature range of the low-boiling working fluid expansion process. In the context of the ORC system, a key feature is that the expansion process begins when the working fluid is in a saturated vapor state, indicated by a vapor quality x_2=1. This thermodynamic state is visually represented in Fig. 2.5(a), where state point 2 is aligned with the saturated vapor curve, highlighting the precise starting condition of the expansion process in the ORC system. Moreover, TFC begins the expansion process from a saturated liquid state, where vapor quality is x_2=0. This different starting state is depicted in Fig. 2.5(b). For PE-ORC, various vapor qualities 0<x_2<1 at the inlet to the expanders are introduced. This variation allows for accommodating a range of operational conditions and exploring the performance of the PE-ORC system. Fig. 2.5(c) and (d) illustrate examples of calculation steps for PE-ORC systems, showcasing two different vapor qualities at the inlet to the expander in a $T-s$ diagram for demonstration purposes. Moreover, the vapor quality x_2 ranges from 0.1 to 0.9 with the increment vapor quality step Δx_2=0.1.

It is essential to note in Fig. 2.5 that what appears to be a single isobaric curve of the heating process for a pressurized liquid, process 1 $\rightarrow$ 2, is not a singular line. At first glance, the graph shows a single continuous curve representing the isobaric heating process of a pressurized liquid. However, this perceived curve comprises multiple distinct curves, each corresponding to a different temperature range within the heating process. These curves appear merged into one because

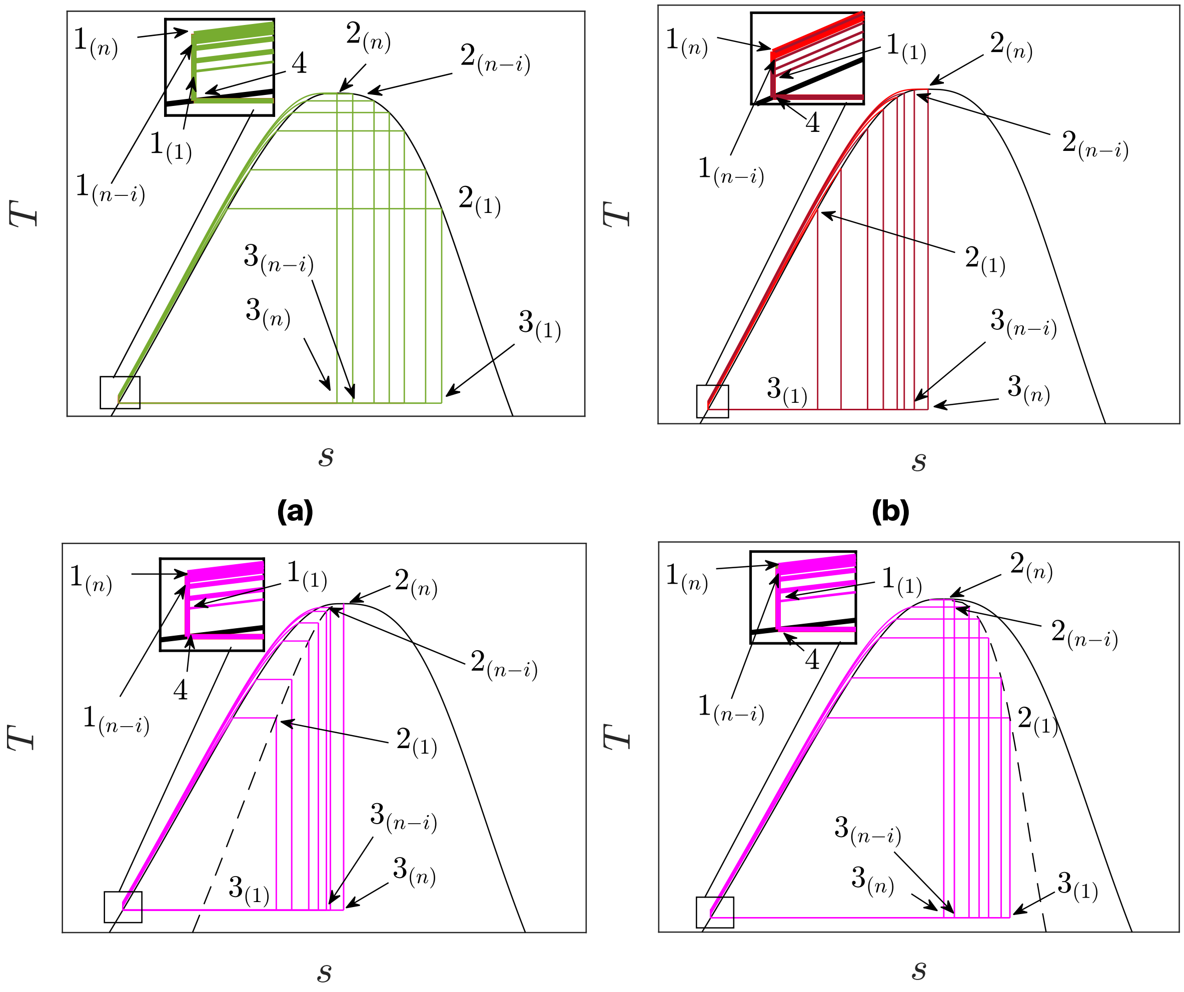

(a)

(b)

(c)

(d)

Fig. 2.5. The steps of thermodynamic modeling simulation as an example in this illustration using wet working fluid in $T-s$ diagram for (a) ORC, (b) TFC, (c) PE-ORC with 0<x_2<0.5, and (d) PE-ORC with 0.5<x_2<1 [86]. The modeling simulations focus on increasing the operational temperature range (in this case, it can also refer to increasing the operating temperature range of the cycle) of the low-boiling-point working fluid expansion process 2 $\rightarrow$ 3 in ORC, PE-ORC, and TFC. This adjustment aims to assess its impact on the cycle efficiency of each system. It should be noted that the isentropic expansion process depicted in this figure serves an illustrative purpose. It is used to compare the low-boiling working fluid expansion processes across ORC, PE-ORC, and TFC.

they are extremely close to each other. However, when each diagram is magnified, the individual curves become distinguishable, providing a clearer understanding of the process. A similar condition is also found in the pressurizing process 4 $\rightarrow$ 1, which initially appears as a single continuous curve under ideal conditions.

The modeling simulation of the thermodynamic cycle outlined earlier can be performed using various programming languages. This investigation used MATLAB to conduct the simulation and perform the calculations. To accurately simulate the thermal behavior of the working fluids within the cycle, the thermal properties were sourced from two reputable databases (i.e., CoolProp [87], and REFPROP 10.0 [88]). These databases are well-regarded for their comprehensive and precise data on the thermal properties of various substances, making them invaluable resources for this kind of modeling simulation. The simulation itself was methodically and systematically carried out from the initial step (labeled as step 1) to the final step (labeled as step n), following a predefined increment step (denoted as i), which is illustrated in Fig. 2.5. A detailed flow chart of the modeling simulation is provided in Fig. 2.6.

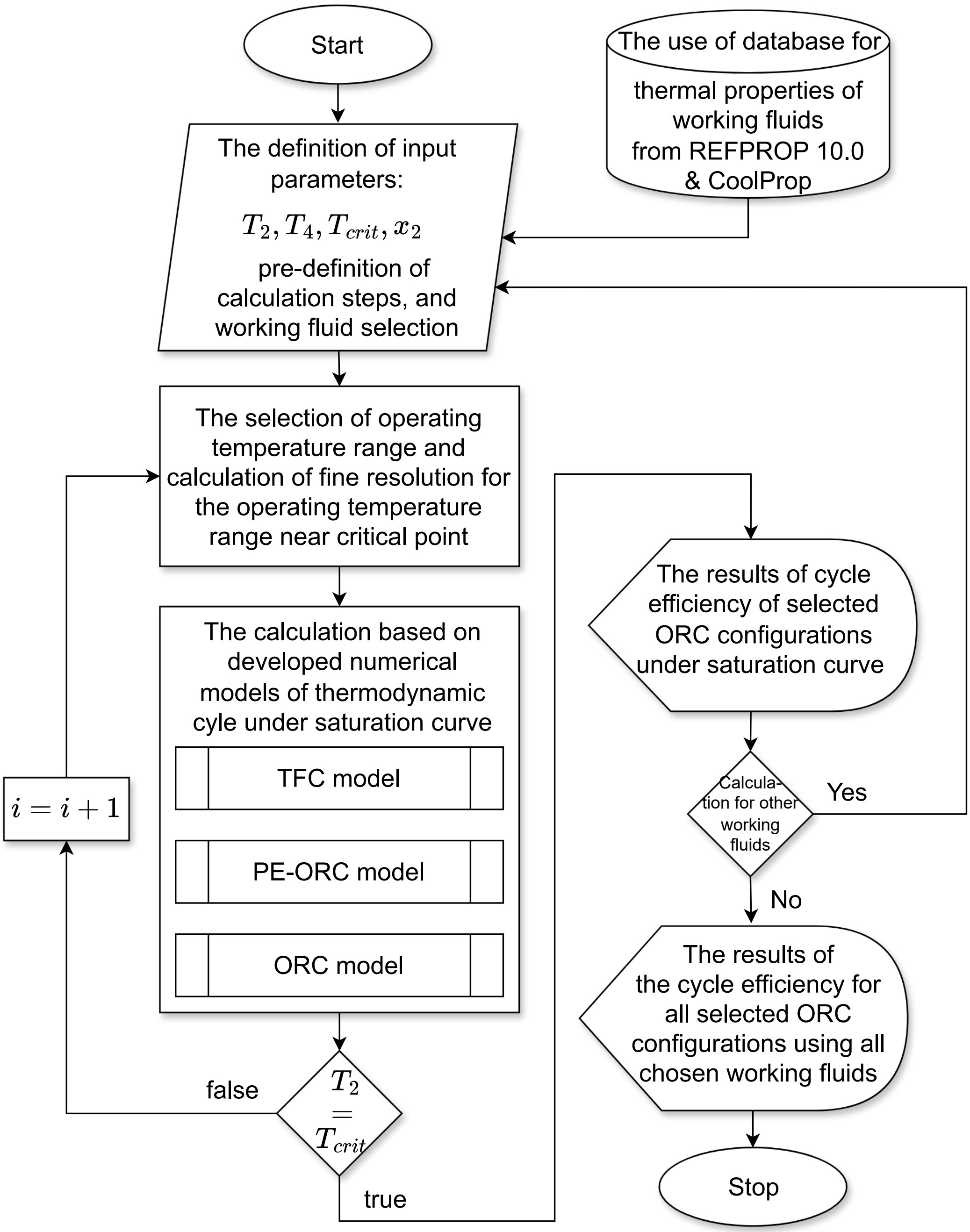

Fig. 2.6. A flow chart of modeling simulation for selected ORC systems under subcritical operating conditions.

2.3.2. General mathematical model of ORC systems and trilateral flash cycle

The process of mathematical modeling for the simulation relies on two fundamental principles, mass balance and energy balance, which are applied to each system component. These principles help accurately simulate the behavior and performance of the thermodynamic cycle. To comprehend how the mass of the working fluid is entering each component of the system, the mass balance is important. The rate of mass for working fluid in each component can be described using Eq. 2.1, where $\dot{m}$, m, and t refer to mass flow rate, mass, and time, respectively. In this study, the model incorporates a steady-state assumption for simulation. Under steady-state conditions, the mass flow rate of working fluid into each component equals the outlet, representing the mass flow rate balance described in Eq. 2.2.

$$\frac{dm}{dt} = \dot{m}_{\text{in}} - \dot{m}_{\text{out}} \tag{2.1}$$

$$\dot{m}_{\text{in}} = \dot{m}_{\text{out}} \tag{2.2}$$

In addition, the concept of energy balance within the simulation is quantified by the rate at which energy is transferred or transformed. This rate is detailed in Eq. 2.3, which outlines how energy interacts with each system component. Given that the simulation assumes a steady-state operation—where conditions do not change over time—the principle of energy conservation is described in Eq. 2.4. In this study, both kinetic ($v_{\text{in}}^2/2$) and potential (gz_{in}) energy are negligible. Therefore, the energy balance can be described as Eq. 2.5. The cycle operates under the assumption that each system component functions without any losses. Furthermore, the energy balance of each component in each cycle is listed in Table 2.1, where subscripts of 'wf' and 'is' refer to working fluid and isentropic. In Eqs. 2.3-2.5, E, $\dot{Q}$, $\dot{W}$, h, v, g, and z represent energy, heat transfer rate, energy transfer rate/power, specific enthalpy, velocity, gravitational acceleration, and height/elevation, respectively. In this case, the isentropic efficiencies of the expander ($\eta_{\text{EXP,is}}$) and the pump ($\eta_{\text{PMP,is}}$) are also introduced.

$$\frac{dE}{dt} = \dot{Q} - \dot{W} + \dot{m}_{\text{in}}\left(h_{\text{in}} + \frac{v_{\text{in}}^2}{2} + gz_{\text{in}}\right) - \dot{m}_{\text{out}}\left(h_{\text{out}} + \frac{v_{\text{out}}^2}{2} + gz_{\text{out}}\right) \tag{2.3}$$

$$\dot{Q} - \dot{W} + \dot{m}_{\text{in}}\left(h_{\text{in}} + \frac{v_{\text{in}}^2}{2} + gz_{\text{in}}\right) - \dot{m}_{\text{out}}\left(h_{\text{out}} + \frac{v_{\text{out}}^2}{2} + gz_{\text{out}}\right) = 0 \tag{2.4}$$

$$\dot{Q} - \dot{W} + \dot{m}_{\text{in}}h_{\text{in}} - \dot{m}_{\text{out}}h_{\text{out}} = 0 \tag{2.5}$$

For clarity, the specific configuration of the heat exchangers (liquid heater, partial evaporator, and evaporator) used to absorb the heat sources to increase the temperature and change the phase of the working fluid in each cycle is detailed in Table 2.2. This table uses a matrix format to describe the component used in each cycle's heat exchange process 1 → 2.

Moreover, the cycle efficiency of each thermodynamic cycle can be calculated using equations listed in Table 2.3. The overall efficiency of a thermodynamic cycle (η_{cycle}) is quantitatively assessed by examining the ratio of the cycle's net output

Table 2.1. Energy balance and implementation of components in selected thermodynamic cycles.

Component	Energy Balance	Implementation
Liquid heater (LH)	$\dot{Q}_{\text{LH}} = \dot{m}_{\text{wf}}(h_{2(x=0)} - h_1)$	TFC, PE-ORC, ORC
Partial evaporator (PE)	$\dot{Q}_{\text{PE}} = \dot{m}_{\text{wf}}(h_{2(0<x<1)} - h_{2(x=0)})$	PE-ORC
Evaporator (EVA)	$\dot{Q}_{\text{EVA}} = \dot{m}_{\text{wf}}(h_{2(x=1)} - h_{2(x=0)})$	ORC
Expander (EXP)	$\dot{W}_{\text{EXP}} = \dot{m}_{\text{wf}}(h_2 - h_{3,\text{is}})\eta_{\text{EXP,is}}$ $\eta_{\text{EXP,is}} = (h_2 - h_3)/(h_2 - h_{3,\text{is}})$	all cycles
Condenser (CDS)	$\dot{Q}_{\text{CDS}} = \dot{m}_{\text{wf}}(h_3 - h_4)$	all cycles
Pump (PMP)	$\dot{W}_{\text{PMP}} = \dot{m}_{\text{wf}}(h_{1,\text{is}} - h_4)/\eta_{\text{PMP,is}}$ $\eta_{\text{PMP,is}} = (h_{1,\text{is}} - h_4)/(h_1 - h_4)$	all cycles

Table 2.2. A configuration matrix of heat exchanger process 1 → 2 for each cycle.

Cycle	LH	PE	EVA	Energy balance in the process 1 → 2
TFC	x	-	-	$\dot{Q}_{\text{HE,TFC}} = \dot{Q}_{\text{LH}}$
PE-ORC	x	x	-	$\dot{Q}_{\text{HE,PE-ORC}} = \dot{Q}_{\text{LH}} + \dot{Q}_{\text{PE}}$
ORC	x	-	x	$\dot{Q}_{\text{HE,ORC}} = \dot{Q}_{\text{LH}} + \dot{Q}_{\text{EVA}}$

Table 2.3. Efficiencies of the cycle.

Cycle	Efficiency of the cycle
TFC	$\eta_{\text{TFC}} = (\dot{W}_{\text{EXP,TFC}} - \dot{W}_{\text{PMP,TFC}})/\dot{Q}_{\text{HE,TFC}}$
PE-ORC	$\eta_{\text{PE-ORC}} = (\dot{W}_{\text{EXP,PE-ORC}} - \dot{W}_{\text{PMP,PE-ORC}})/\dot{Q}_{\text{HE,PE-ORC}}$
ORC	$\eta_{\text{ORC}} = (\dot{W}_{\text{EXP,ORC}} - \dot{W}_{\text{PMP,ORC}})/\dot{Q}_{\text{HE,ORC}}$

power to the heat rate of the heat sources used as input. This parameter represents the efficiency with which the cycle converts thermal energy from the heat sources into usable mechanical or electrical power. Each cycle uses heat sources differently, affecting how heat is transferred from those sources to the working fluid, as described in Table 2.2. Also, it is essential to note that the choice of working fluid and the expansion process plays a crucial role in determining the efficiency of the cycle. Therefore, this study specifically examines and explores how different working fluids expansion processes impact the overall efficiency of the thermodynamic cycle.

2.4. Discussion and main contributions

This investigation evaluated the efficiency of different ORC systems using different organic working fluids: wet, isentropic, and dry. Propane, butane, isopentane, and Novec649 were chosen as representations of each working fluid. Propane is a typical wet working fluid, while butane and isopentane are isentropic working fluids. As HC working fluids, all three are increasingly gaining attention for their potential application in analyzed power cycles. For example, there is growing interest in the utilization of propane as a working fluid for thermodynamic cycles as propane offers good performance in terms of the efficiency of the cycle in several applications, including cold energy utilization [89, 90]. Due to the high flammability of these HC working fluids, Novec649 was selected as a safer alternative, which is notable for its non-flammability [91] and also functions as a dry working fluid. In this case, these four substances are chosen for illustrative purposes.

The modeling simulation maintained a constant lower temperature T_4=293.15 K while an upper temperature was 353.15 K<T_2<T_c. This upper temperature was increased in increment step i=1 K, as shown in Fig. 2.5. Close to the critical point, however, the increment step was reduced to between 0.1 K and 0.001 K to achieve higher resolution and a smoother curve. In the case of PE-ORC, the vapor quality was adjusted in increments of 0.1 to 0.9 using increment steps $\Delta\, x_2$=0.1. In addition, some parts of this study are also described in [86, 92] (which includes the variation T_4), in [6, 92] (using different temperature ranges and different working fluids), and in [93] (using carbon dioxide as an example of wet working fluid).

Fig. 2.7 shows the modeling simulation results for ORC, PE-ORC, and TFC in $\eta_\text{cycle} - T_2$ diagrams. This figure represents a side-by-side comparison of simulation results under varying operating conditions. This study investigated two scenarios: the first under ideal operating conditions, depicted in Figs. 2.7(a), 2.7(c), 2.7(e), and 2.7(g); the second under specific operating conditions, where the isentropic efficiency of both the pump and the expander is set as 0.8, which is illustrated in Figs. 2.7(b), 2.7(d), 2.7(f), and 2.7(h). Selecting an isentropic efficiency value of 0.8 is a common practice for several practical reasons. This value provides a realistic representation of performance, aligns with design and economic considerations, and serves as a useful benchmark. It seems that raising the operating temperature range of ORC, PE-ORC, and TFC might lead to higher cycle efficiency with certain operating temperature ranges (i.e., with certain low-boiling working fluid expansion processes). It can be proved using wet and isentropic working fluids up to the maximum efficiency of the cycle (see Figs. 2.7(a)-(d)), demonstrated by propane and butane, respectively. The efficiency of PE-ORC is observed in between ORC and TFC in $\eta_\text{cycle} - T_2$ diagram. An increase in vapor quality to the inlet to the expander in PE-ORC, represented by x_2 in Fig. 2.7(a)-(f), may improve the overall efficiency of the cycle. This condition is observed not just under ideal operating conditions but also under specific conditions, which involve adjusting the isentropic efficiency of both the pump and the expander.

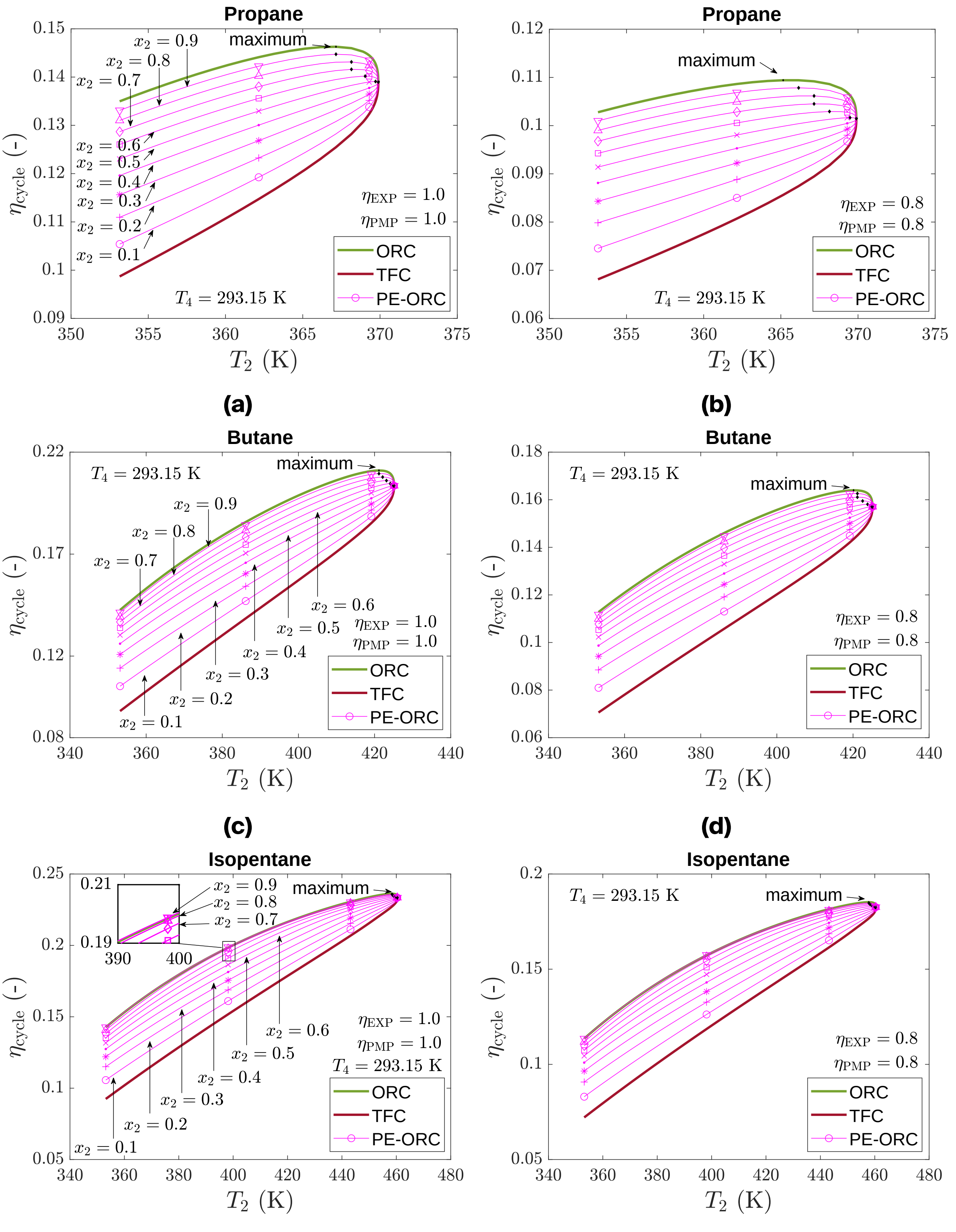

Fig. 2.7. The result of modeling simulation for different ORC systems (basic ORC without a superheater, PE-ORC, and TFC) using **(a)-(b)** propane as an exemplary of the wet working fluid, **(c)-(d)** butane as an exemplary of the isentropic working fluid, **(e)-(f)** isopentane an exemplary of the isentropic working fluid, and **(g)-(h)** Novec649 as an exemplary of the dry working fluid in $\eta_{\text{cycle}} - T_2$ diagram. It is important to note that the diagram on the left illustrates the thermodynamic operation under ideal conditions. In contrast, the diagram on the right accounts for the thermodynamic operation with an isentropic efficiency of 0.8 for both the expander and the pump. The result is continued on the next page.

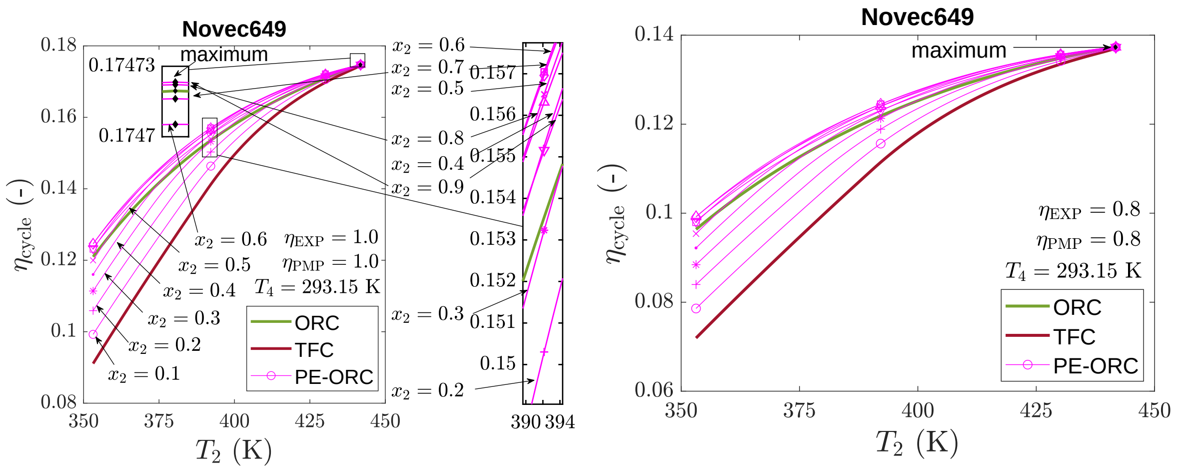

(g) **(h)**

Fig. 2.7. *(continued).*

According to Carnot cycle's efficiency principles, increasing the operating temperature range within a Carnot cycle leads to improved efficiency. For instance, when a lower temperature is T_{c}=293.15 K and an upper temperature is increased to T_{h}=1473.15 K, the Carnot efficiency increased, which is indicated by a red curve illustrated in Fig. 2.8. In addition, by assuming T_{h}=473.15 K and by reducing T_{c}<293.15 K, reaching cryogenic temperature results in a significantly improved efficiency from 0.38 to 1.00, indicated by blue line illustrated in Fig. 2.8. This approach also applies for different assumed T_{h} as 293.15 K, 673.15 K, 873.15 K, 1073.15 K, 1273.15 K, and 1473.15 K, which are indicated by blue lines. Using a similar approach, this study [94] also explored the effects of lowering the cold temperature in ORC and TFC while keeping the hot temperature constant. The study examined applications using low-temperature geothermal heat sources in combination with different cooling sources, such as air, water, dimethyl ether (DME), and liquefied natural gas (LNG). The utilization of liquid hydrogen could also be considered in this case as it is a promising energy carrier or energy storage material for the future. The results revealed a consistent trend in the cycle efficiency, similar to the pattern represented by the blue lines in Fig. 2.8.

A recent study [74] highlighted the highest thermodynamic efficiency of the ORC using certain working fluids, excluding super-dry ones, with very tilted $T - s$ diagrams focusing solely on ORC and TFC but not including PE-ORC. However, Fig. 2.7 also shows the peak efficiency of ORC. It extends the investigation to include PE-ORC, which is state-of-the-art, in this dissertation.

Furthermore, some obtained modeling simulation results demonstrated using selected working fluids in Fig. 2.7 show that the highest thermodynamic efficiency is achievable in both ORC and PE-ORC when the vapor quality is adjusted at the inlet to the expander, noted as x_2. It seems that the cycle efficiency increases when the operational temperature range is expanded to a certain range. Raising T_2 to a critical point increases the enthalpy change of the liquid heater (i.e., the isobaric path extends over the increased temperature in this case) but decreases the enthalpy change in the evaporation process. This effect occurs because the point be-

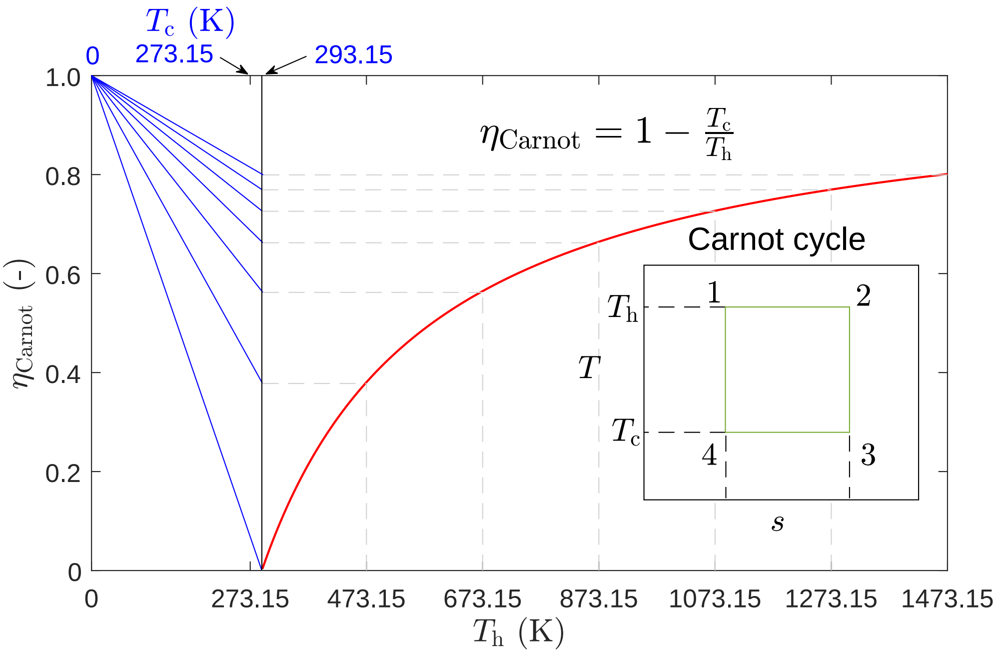

Fig. 2.8. The efficiency variation of the Carnot cycle with increased hot temperature and decreased cold temperature illustrated in the $\eta_{\mathrm{Carnot}} - T_h - T_c$ diagram, adapted from [92]. This diagram illustrates the operation of the Carnot cycle with the isothermal heat addition process 1 → 2, isentropic expansion process 2 → 3, isothermal heat rejection process 3 → 4, and isentropic compression process 4 → 1. The red curve illustrates how the efficiency of the Carnot cycle improves with an increased hot temperature while the cold temperature remains constant T_c=293.15 K. The blue lines illustrate how the efficiency of the Carnot cycle improves with a decreased cold temperature T_c<293.15 K while the hot temperature remains constant (indicated by the dashed gray lines from certain cycle efficiencies).

tween the saturated liquid and vapor curves at the isobaric condition narrows with increasing temperature, indicating a bell-shaped curve, as previously mentioned. In addition, when using the same pressure ratio and reducing the vapor quality at the inlet to the expander leads to a decrease in the enthalpy change in the expander and, subsequently, the condenser. Therefore, this observation indicates that under these conditions, the cycle efficiency of the PE-ORC is lower compared to ORC. Moreover, the cycle efficiency of TFC is the lowest in this case.

Nevertheless, the cycle efficiency of ORC, PE-ORC, and TFC might differ when using dry and other isentropic working fluids, as demonstrated by Novec649 and isopentane, respectively. Figs. 2.7(c)-(h) show that PE-ORC can achieve higher cycle efficiency than ORC under certain operating conditions, potentially reaching the highest cycle efficiency in both ideal and specific scenarios. When examining the case with isopentane under ideal conditions, the cycle efficiency of PE-ORC is higher than ORC, marked by vapor quality at the inlet to the expander x_2=0.9, which is indicated within the magnified rectangle $\eta_{\mathrm{cycle}} - T_2$ diagram in Fig. 2.7(e). This cycle efficiency is also found when the cycle is examined by adjusting the isentropic efficiencies of the expander and pump to the value of 0.8. The cycle efficiency difference between the PE-ORC with x_2=0.9 and ORC is, in this case, relatively low. However, in the scenario which uses Novec649, within the temperature range T_2=390-394 K, PE-ORCs with vapor quality values ranging from 0.4 to 0.9, exhibit higher cycle efficiencies than ORC, as illustrated in a detailed view of Fig. 2.7(g). Among these, the PE-ORC with x_2=0.6 records the highest cycle efficiency under ideal conditions within the temperature range T_2=390-394 K. Upon closely examining the area near the critical point, the highest cycle efficiency for PE-ORC is observed at x_2=0.9 under ideal operating conditions, as depicted in Fig. 2.7(g). Further analysis, specifically using Novec649 and considering the isentropic efficiencies of the expander and pump equal to 0.8, reveals a consistent trend: PE-ORCs maintain higher cycle efficiency compared to both ORC and TFC.

The cycle efficiency of PE-ORC may vary and can be potentially higher than ORC and TFC when using isopentane and Novec649. Therefore, further investigations focused on dry working fluids, specifically examining the working fluids from a siloxanes family. In that case, hexamethyldisiloxane (MM), octamethyltrisiloxane (MDM), decamethyltetrasiloxane (MD2M), dodecamethylpentasiloxane (MD3M), and tetradecamethylhexasiloxane (MD4M) was chosen as a good demonstration and representative working fluids. The difference in saturated liquid-vapor curve between these working fluids is given in a $T-s$ diagram illustrated in Fig. 2.9(a). The saturated curve tends to shift slightly to the left on a $T-s$ diagram, indicating higher boiling points for more complex molecules at a given pressure (i.e., the complexity increases from MM to MD4M). Moreover, the isobaric lines under the saturated curve become longer from MD4M to MM, indicating that more heat/cooling is required for evaporation/condensation. Moreover, the critical point rises when moving from MM to MD4M.

Figs. 2.9(b)-(f) present and compare the outcomes of modeling simulations for MM, MDM, MD2M, MD3M, and MD4M, respectively. These simulations were conducted under conditions where the isentropic efficiency of both the expander and the pump was fixed as 0.8. In scenarios using dry working fluids, the expansion process ends in the superheated zone, identified by the isobar at the pressure of the condenser. This endpoint of the expansion lies well above the minimum temperature of the cycle (T_4), leading to a shorter expansion phase as illustrated in Fig. 2.4(b). It is worth noting that designating T_4=293.15 K could result in vacuum pressure, and a vacuum pump can address this issue. Moreover, the absence of a recuperative heat exchanger in the standard ORC setup means that not all input heat is converted to work; some is instead dissipated through isobaric cooling, diminishing efficiency. This factor significantly affects the isentropic efficiency of the expander in all cycles under review. In the same operational pressure ratio and at a certain operating temperature range, TFC is found to be more efficient than ORC and PE-ORC. While this cycle efficiency contrast may not be evident with MM, it becomes visible with MDM, MD2M, MD3M, and MD4M, as shown in Figs. 2.9(c)-(f). Notably, there appear to be points where the cycle efficiency of ORC, TFC, and possibly PE-ORCs intersect in $\eta_{\text{cycle}}-T_4$ diagram. At various operating temperature ranges, similar overlaps in the cycle efficiency among ORC, PE-ORC, and TFC also appeared in [86].

Furthermore, instances where PE-ORCs achieve higher cycle efficiency compared to ORC and TFC across various working fluids are recorded in Table 2.4. This comparison takes into account an operating temperature range for T_4 from T_b to

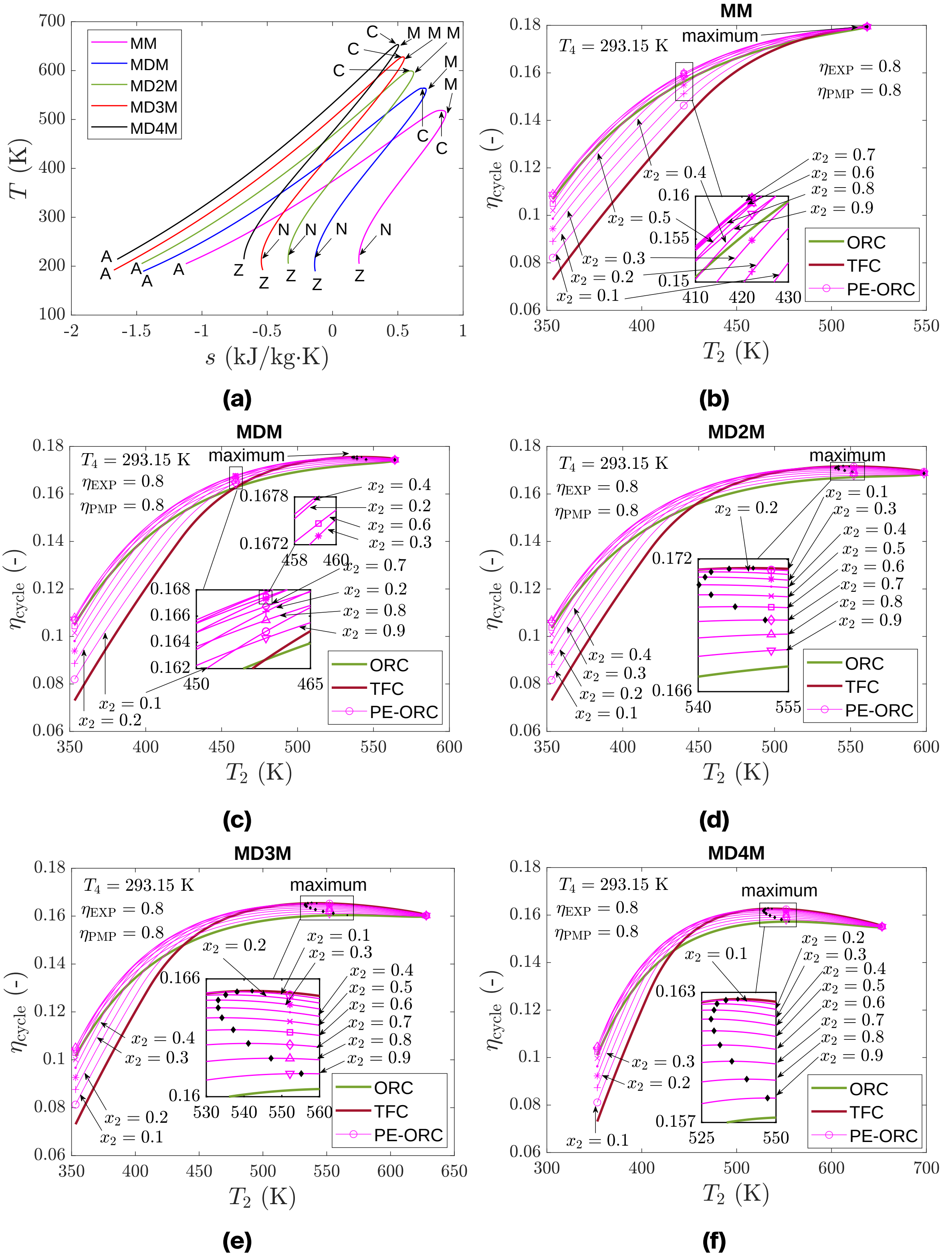

(a) (b) (c) (d) (e) (f)

Fig. 2.9. Comparison of selected dry working fluids (MM, MDM, MD2M, MD3M, and MD4M) (a) in $T-s$ diagram and their result of modeling simulation using (b) MM, (c) MDM, (d) MD2M, (e) MD3M, and (f) MD4M in $\eta_{\text{cycle}}-T_2$ diagram. It is important to note that due to the proximity of point N to point Z, even some isentropic siloxanes (MM, MDM, MD2M, MD3M) behave like dry working fluids in most parts of the relevant temperature range. These working fluids are also classified as dry working fluids according to other alternative classifications [83, 84].

Table 2.4. A list of isentropic and dry working fluids where cycle efficiency of PE-ORC potentially higher than TFC and ORC.

Name of working fluid	**Type** [81]	T_c (K) [88]	T_b (K) [88]	**Case** [2] [86]
Hexamethyldisiloxane (MM)	ANZCM [1]	518.75	373.66	Medium
Octamethyltrisiloxane (MDM)	ANZCM [1]	564.09	425.63	High
Decamethyltetrasiloxane (MD2M)	ANZCM [1]	599.40	467.59	High
Dodecamethylpentasiloxane (MD3M)	ANZCM [1]	628.00	503.02	High
Tetradecamethylhexasiloxane (MD4M)	AZCM	653.20	532.85	High
Octamethylcyclotetrasiloxane (D4)	AZCM	586.50	448.89	High
Decamethylcyclopentasiloxane (D5)	AZCM	618.30	484.10	High
Dodecamethylcyclohexasiloxane (D6)	AZCM	645.78	518.11	High
Hexane	ANZCM	507.82	341.87	Low
Heptane	ANZCM	540.13	371.53	Medium
Octane	ANZCM	568.74	398.79	Medium
Nonane	ANZCM [1]	594.55	423.91	Medium
Decane	ANZCM [1]	617.70	447.27	High
Undecane	ANZCM [1]	638.80	468.93	High
Dodecane	AZCM	658.10	489.44	High
Isopentane	ANCMZ	460.35	300.98	Low
Isohexane	ANCMZ	497.70	333.36	Low
Neopentane	AZCM	433.74	282.65	Low
Cyclohexane	ANZCM [1]	553.60	353.87	Low
Ethylbenzene	ANCMZ	617.12	409.31	Low
Novec649	AZCM	441.81	322.20	Medium
M-xylene	ANZCM	616.89	412.21	Low
O-xylene	ANZCM	630.26	417.52	Low
P-xylene	ANZCM [1]	616.17	411.47	Low
Methyllinoleate	ANZCM [1]	799.00	628.84	High
Methyllinolenate	ANZCM [1]	772.00	629.13	High
Methyloleate	ANZCM [1]	782.00	627.17	High
Methylpalmitate	AZCM	755.00	602.27	High
Methylstearate	AZCM	775.00	629.56	High
R113	ANZCM	487.21	320.73	Low
R365mfc	ANZCM [1]	460.00	313.34	Low
RC318	AZCM	388.38	267.17	Low
Toluene	ANCMZ	591.75	383.75	Low

[1] It is important to note that although these substances appear to be isentropic working fluids (ANZCM types) based on ACZMN points, these isentropic working fluids behave like dry ones in most parts of the relevant temperature range due to the proximity of the point N to Z. These working fluids are also classified as dry working fluids according to other alternative classifications [83, 84].

[2] This classification was based on qualitative analysis. To obtain more precise and reliable results, further quantitative analysis is needed.

T_b+40 K and for T_2 from T_b+80 K to T_c. In this study, T_c and T_b refer to the critical and the normal boiling temperature of working fluids, respectively. These temperatures are provided in Table 2.4. The temperature at the inlet to the pump, denoted as T_4=T_b, is selected to assess performance at atmospheric pressure, eliminating the need for a vacuum pump application. It is possible to have temperatures lower than T_b and below atmospheric pressure, but it must not fall below the temperature of solidification, which is set at 10 K above the triple point temperature for safety reasons. Also, the application of a vacuum pump can be carefully considered. For cooling temperatures under 273.15 K, various cooling sources mentioned previously, such as liquefied natural gas, liquefied dimethyl ether, liquefied hydrogen, and other cryogenic substances, can be utilized effectively.

The 'case' in the fifth column of Table 2.4 refers to a classification where the cycle efficiency of PE-ORCs is potentially higher than TFC and ORC with regard to the working fluids. The criteria used for classifying the efficiency of potential working fluids in relation to ORC and TFC is based on their cycle efficiency intersections in the $\eta_{cycle} - T_2$ diagram. 'Low' indicates scenarios where ORC and TFC do not intersect, yet PE-ORC's efficiency may still surpass both, as seen with isopentane in Fig. 2.7(e)-(f). 'Medium' denotes cases where ORC and TFC intersect, but the region where PE-ORC's efficiency exceeds that of ORC and TFC is small, exemplified by MM in Fig. 2.9(b). 'High' signifies situations with an ORC and TFC intersection where the extent of PE-ORC's superior cycle efficiency over ORC and TFC is significant, as illustrated by MDM, MD2M, MD3M, and MD4M in Figs. 2.9(c)-(f). It is worth noting that adjusting the operating temperature range of the cycle in this modeling simulation leads to the change in the case of having higher cycle efficiency of PE-ORCs than TFC and ORC. Moreover, it is important to note that the classifications of 'low,' 'medium,' and 'high' were not quantitatively defined. Instead, these categories were derived from observed performance patterns and expert judgments. To better understand the boundaries between these classifications, further investigation is needed. This future research should include examining the potential transitions between classes (classification chains of the working fluid) by altering the lower endpoint temperature.

Table 2.5. Selection of working fluids based on the cycle efficiency of ORC, PE-ORC, and TFC.

Type of working fluids	Possible maximal cycle efficiency
Wet	ORC
Isentropic	ORC or PE-ORC
Dry	PE-ORC or TFC

Furthermore, the results discussed above indicate that designing PE-ORC or TFC systems to achieve higher cycle efficiency than an ORC without a superheater is feasible by using typical dry working fluids. Moreover, peak cycle efficiency in both

PE-ORC and TFC systems can be expected. The classification, selection of these working fluids, and their peak/higher cycle efficiencies are summarized in Table 2.5. The selection of working fluid is beneficial for initial studies because it offers a basic knowledge of the suitable working fluids to use for improving the efficiency of energy conversion systems, especially in the case of thermal power generation. In addition, the understanding of how different types of working fluids (wet, isentropic, and dry) perform in various operational conditions paves the way for more targeted and efficient system design. This knowledge facilitates the refinement of ORC, PE-ORC, and TFC systems for a wider range of applications, from industrial waste heat recovery to renewable energy and cold energy utilization.

2.5. Conclusions

In this chapter, a theoretical investigation through modeling simulations has been conducted to analyze the efficiency of selected different ORC systems under subcritical operating conditions (e.g., ORC, PE-ORC, and TFC) influenced by the temperature operating range of the low boiling working fluid expansion process, the vapor quality at the inlet to the expansion process, and different types of working fluids. The methodology of modeling simulation has been introduced and described along with the mathematical model description.

PE-ORC acts as an intermediate cycle between ORC and TFC, with partially evaporated conditions, also meaning its expansion process begins in a two-phase condition where the vapor quality, x_2, ranges between 0 and 1. This contrasts with ORC, which operates under fully evaporated conditions (x_2=1 or superheated condition), and TFC, which starts from a fully liquid state x_2=0. In addition, part of the main contributions from this chapter is described in Thesis 1.

Thesis 1. *The theoretical modeling simulation result shows that under subcritical operating conditions, the cycle efficiency of partially evaporated organic Rankine cycle (PE-ORC) is not always located between that of organic Rankine cycle (ORC) with the saturated vapor state of the working fluid at the inlet to the expander and trilateral flash cycle (TFC or trilateral ORC) in the cycle efficiency and temperature of the working fluid at the inlet to the expander ($\eta_{\text{cycle}} - T_2$) diagram. The observation using dry and some isentropic working fluids shows that PE-ORCs have the potential to achieve higher cycle efficiency than both ORC and TFC, especially when the modeling simulation assumes a certain isentropic efficiency for both the pump and expander. This observation highlights the importance of choosing the appropriate working fluid for specific subcritical power cycles, offering new insights into the selection process. In designing the PE-ORC or TFC with higher cycle efficiency, it is suggested to design the cycle using dry working fluids.*

The publications by the author that are related to Thesis 1 are [6, 86, 92, 93, 94].

Furthermore, according to the principle of Carnot cycle efficiency, increasing the operating temperature range of the cycle should enhance its overall cycle efficiency. Using this theoretical approach, part of the main contributions from this chapter is described in Thesis 2.

Thesis 2. *Increasing the operating temperature range of the low-boiling working fluid expansion process in the organic Rankine cycle (ORC) with the saturated vapor state of the working fluid, partially evaporated organic Rankine cycle (PE-ORC), and trilateral flash cycle (TFC or trilateral ORC) with various types of working fluids may improve the cycle efficiency under subcritical operating conditions; however, this improvement is specific to certain operating temperature ranges. When the temperature of the working fluid to the expander inlet is fixed, and the temperature of the working fluid from the expander outlet is below 273.15 K, the cycle efficiency of the ORC, PE-ORC, and TFC is increased. Nonetheless, when increasing the temperature of the working fluid to the expander inlet near the critical point, the maximal cycle efficiency (i.e., a peak cycle efficiency) can be observed in the cycle efficiency and temperature of the working fluid at the expander inlet (*$\eta_{\text{cycle}} - T_2$*) diagram. This observation implies that any increase in the temperature of the working fluid to the expander inlet beyond this point (the temperature when the maximal cycle efficiency is achieved) may result in a decrease in efficiency. This trend in cycle efficiency can be observed not only in ORC but also in PE-ORC and TFC. In scenarios involving isentropic and dry working fluids, the cycle efficiency of PE-ORCs or TFC may be over the maximal cycle efficiency of ORC with saturated vapor state of the working fluid at the inlet to the expander under both ideal and certain conditions.*

The publications by the author that are related to Thesis 2 are [6, 86, 92, 93, 94].

This investigation serves as a benchmark from a classification to a selection of working fluids in designing different ORC systems under subcritical operating conditions.

3

Analysis of low-boiling working fluid expansion process in different ORC systems from subcritical to transcritical operating conditions

According to a study described in Chapter 2, if the temperature of the working fluid entering the expander is increased up to its critical point, a peak in cycle efficiency can be observed. However, raising the temperature further, above the critical point, alters the operation of the heat exchanger. Operating conditions change from under subcritical pressure to supercritical pressure. In the heat exchanger, the temperature of the working fluid increases and the phase is changed from liquid to supercritical state. The working fluid is then expanded in the expander from a supercritical state to either a superheated state, a saturated liquid, or a two-phase state. In that case, the system is called a transcritical power cycle (TPC) or transcritical ORC. There is a growing interest in the study and development of TPC [11]. Moreover, an article [7] examined the performance of TPC and compared it with ORC. The comparison was limited to specific operational conditions and explored with various working fluids, including R134a, R245fa, Solkatherm SES36, n-pentane, MDM, and toluene. It seems that there is still room for investigation in the cycle efficiency variation of different ORC systems under subcritical and transcritical operating conditions, which is influenced by the temperature range of the low-boiling working fluid expansion process (which can be defined as the pressure ratio range), the type of the working fluid, and the vapor quality. Therefore, in order to comprehend the basic knowledge of this topic, an extended study is required.

Chapter 3 aims to prove that the transition of both ORC and PE-ORC systems into TPC by increasing the temperature and pressure of working fluid to the inlet of the expander results in improved cycle efficiency. Also, it aims to analyze and compare the cycle efficiency of different ORC systems under subcritical and transcritical operating conditions, which are affected by the increased temperature operating range (i.e., increased pressure ratio range) in low-boiling working fluid expansion processes, vapor quality, and the type of working fluid. The methodology of modeling simulation and boundary conditions are introduced as follows.

3.1. Mathematical modeling and simulation of different ORC systems from subcritical to transcritical operating conditions

The model of different ORC systems under subcritical operating conditions has been introduced in Chapter 2, including ORC, PE-ORC, and TFC. In this subchapter, additional methodology for mathematical modeling and simulation for ORC with a superheater and TPC is described.

3.1.1. ORC with a superheater and transcritical power cycle

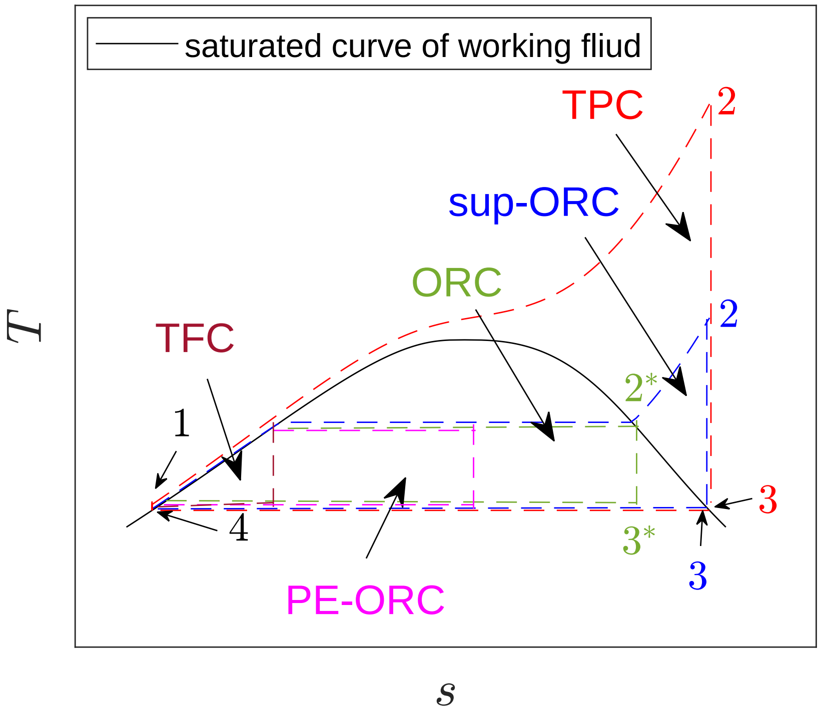

Fig. 3.1. Several ORC systems under subcritical operating conditions (sup-ORC, ORC, PE-ORC, and TFC) and under transcritical operating conditions (TPC) in a $T-s$ diagram. This figure illustrates the operation of each cycle under ideal conditions, featuring isobaric heat exchanger process 1 → 2 for heating and changing the state of the working fluid, isentropic expansion process 2 → 3, isobaric heat exchanger process 3 → 4 for condenser, isentropic pump process 4 → 1. The process 2* (green) → 2 (blue) refers to a superheater.

An additional subcritical power cycle, an ORC with a superheater (sup-ORC), is introduced, which is illustrated in Fig. 3.1. For representative illustration, the basic ORC process is described as a closed cycle of 1 → 2* → 3* → 4. The isentropic expansion process of basic ORC is indicated by process 2* → 3* under two-phase conditions. In order to avoid a two-phase expansion process, in that case, a superheater plays a crucial role by raising the temperature of the working fluid from its saturated vapor state to a superheated state at the inlet to the expander. This transition is depicted in Fig. 3.1, where the process of heating from saturated vapor to superheated condition is marked by a blue dashed line 2* → 2 (superheating

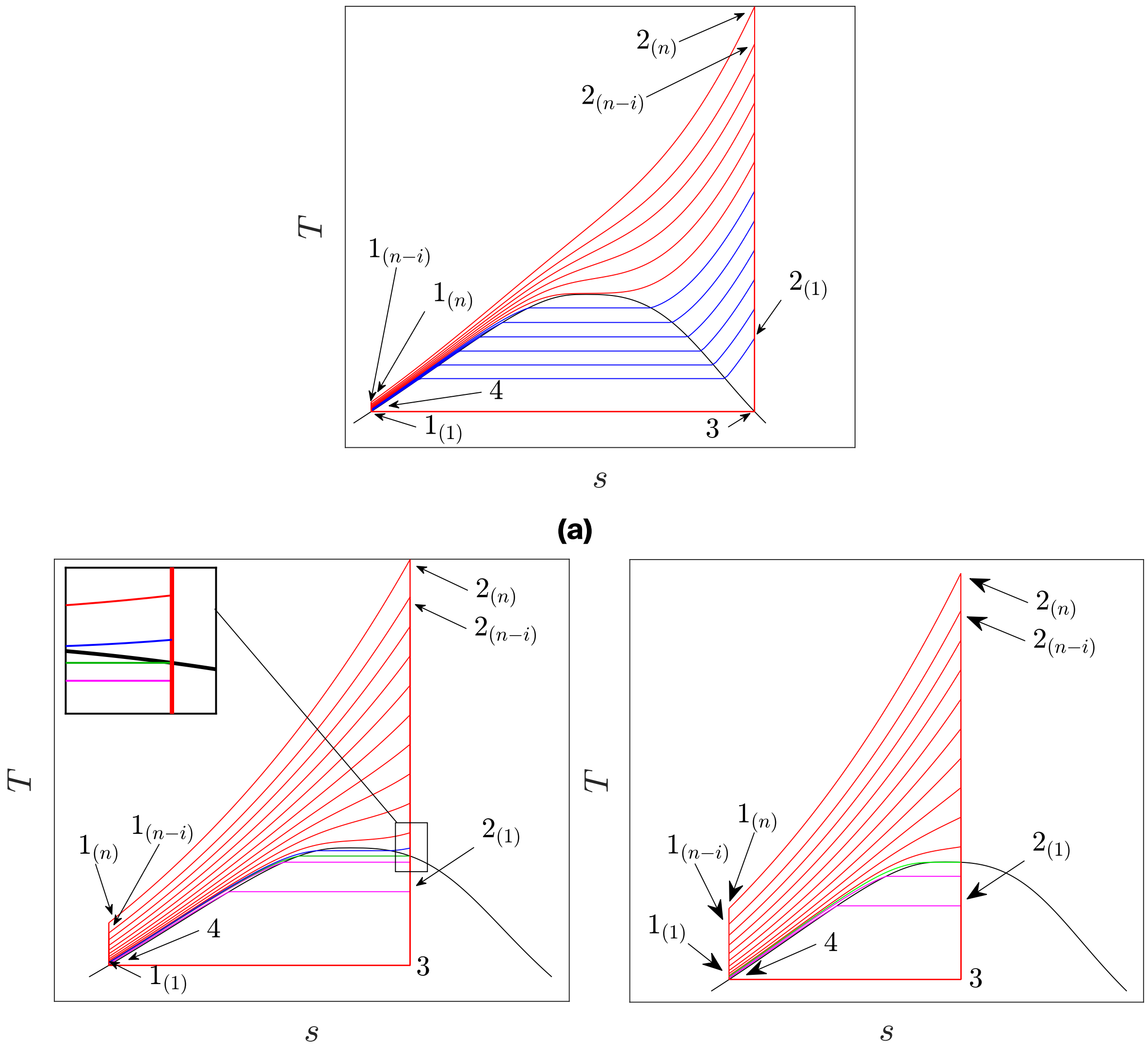

(a)

(b) **(c)**

Fig. 3.2. The steps of thermodynamic modeling simulation as an example in this illustration using wet working fluid in $T - s$ diagram, where **(a)** isentropic expansion processes ending in saturated vapor state (x_2=1), **(b)** isentropic expansion processes that result in a two-phase state indicated by specific entropy values, and **(c)** isentropic expansion processes that pass through the critical point, adopted from [6, 93]. The colors of the lines indicate different types of thermodynamic power cycles: red for TPC, green for ORC without a superheater, blue for sup-ORC, and magenta for PE-ORC. The modeling simulations focus on increasing the operational temperature range of the cycle (in this case, it can also refer to increasing the operating temperature range of the cycle) of the low-boiling-point working fluid expansion process 2 → 3 from different ORC systems (ORC, PE-ORC, sup-ORC) to TFC. This adjustment aims to assess its impact on the overall cycle efficiency of each system. It should be noted that the isentropic expansion process depicted in this figure serves an illustrative purpose in comparing the low-boiling working fluid expansion processes across different ORC systems and TPC.

process). In the following step, the expansion process occurs under dry or superheated conditions, process 2 → 3, as indicated by the blue dashed line. After the

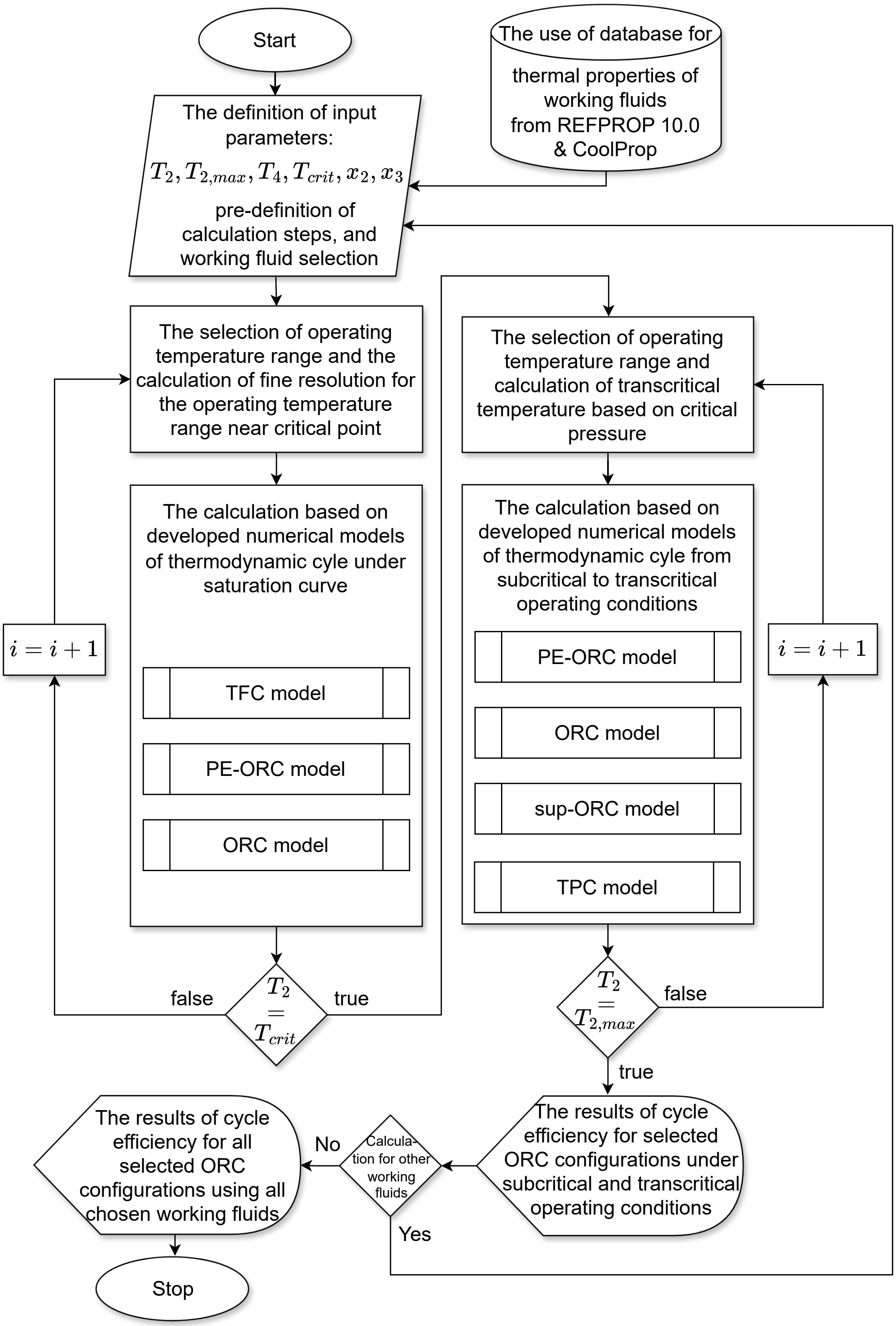

Fig. 3.3. A flow chart of modeling simulation for ORC systems under subcritical and transcritical operating conditions.

expansion process, the working fluid is condensed back into liquid form. For a basic ORC system, the working fluid moves through the condenser, which is indicated by process 3* $\rightarrow$ 4 in the $T-s$ diagram. However, for sup-ORC, there is an additional cooling step due to the reduction of the wetness (i.e., an increase in the vapor quality). This step extends process 3 $\rightarrow$ 3*, condensing the fluid before it reaches state 4. It is important to note that in some cases, the temperature at state 2 for sup-ORC may exceed the critical temperature, even though the corresponding isobaric pressure of the superheater remains below the critical pressure. The following processes are liquefication in the condenser and pumping the liquid working fluid in the pump, which is described by processes 3 $\rightarrow$ 4 and 4 $\rightarrow$ 1, respectively.

In contrast, TPC operates under different conditions, which means that the temperature of a working fluid is always raised in the isobaric process above its critical temperature, resulting in a phase where the fluid exceeds the thermodynamic parameters of the critical point. The isobaric heat exchange process in TPC occurs above the critical pressure to the supercritical region. This process is shown by the red marking 1 $\rightarrow$ 2 in Fig. 3.1. Following this, the isentropic expansion process occurs from supercritical condition to superheated state, a transition illustrated by process 2 $\rightarrow$ 3 with a red dashed line. Although for illustrative purposes, point 3 is shown ending in the saturated vapor state, in practical scenarios, the expansion process might actually end in a superheated region. The following processes are the liquefication in the condenser and pumping of the liquid working fluid in the pump, which are described as processes 3 $\rightarrow$ 4 and 4 $\rightarrow$ 1, respectively.

The previously outlined process serves as a foundation for introducing a range of modeling simulations, from subcritical cycles to TPC, under specific operating conditions. In this simulation, the focus is on wet and isentropic working fluids. These working fluids are chosen because their properties closely align with the saturated vapor line that suits this simulation (which is the boundary condition of this study). The simulation process is visually represented in Fig. 3.2. It begins by setting an upper temperature (T_2) and a constant lower temperature (T_4) as the temperature range of the cycles. An upper temperature (T_2) is systematically varied by a specific increment (ΔT_2). A key aspect of this simulation is the guidance provided by the isentropic expansion process. This means that if the upper temperature increases, the simulation may proceed through a transition from subcritical cycles (PE-ORC, ORC, and sup-ORC) to TPC. Each cycle is differentiated by color in Fig. 3.2, making it easy to follow the transitions. In addition, the simulation makes the isobaric heating process 1 $\rightarrow$ 2 particularly clear. This is a crucial step in the simulation, highlighting how the temperature of the working fluid is increased in the heat exchanger. Moreover, a detailed flow chart of the modeling simulation is provided in Fig. 3.3.

3.1.2. General mathematical model of ORC systems and transcritical power cycle

The simulation in this chapter was carried out from the initial step (labeled as step 1) to the final step (labeled as step n), following a sequence of incremental steps (indicated by i) as depicted in Fig. 3.2. The principles of mass and energy balance used in this study, as outlined in the previous chapter, are already described by Eqs.

2.1-2.5. In this context, it is important to note that both kinetic energy ($v_{\text{in}}^2/2$) and the potential energy (gz_{in}) are considered negligible. The energy balance for each component of ORC without a superheater and PE-ORC has previously been detailed, as shown in Table 2.1. For the components specific to the ORC with a superheater and TPC, such as the expander, pump, and condenser, the same approach, which is outlined in Table 2.1, is applied. Nevertheless, the inclusion of a superheater in the ORC system introduces additional components, which are listed and detailed in Table 3.1.

Table 3.1. Energy balance and implementation of additional/replacement heat exchanger for sup-ORC and TPC.

Component	Energy Balance	Implementation
Liquid heater (LH)	$\dot{Q}_{\text{LH}} = \dot{m}_{\text{wf}}(h_{2(x=0)} - h_1)$	TFC, PE-ORC, ORC, and sup-ORC
Partial evaporator (PE)	$\dot{Q}_{\text{PE}} = \dot{m}_{\text{wf}}(h_{2(0<x<1)} - h_{2(x=0)})$	PE-ORC
Evaporator (EVA)	$\dot{Q}_{\text{EVA}} = \dot{m}_{\text{wf}}(h_{2(x=1)} - h_{2(x=0)})$	ORC and sup-ORC
Superheater (SUP)	$\dot{Q}_{\text{SUP}} = \dot{m}_{\text{wf}}(h_{2(\text{sup})} - h_{2(x=1)})$	sup-ORC
Supercritical heat exchanger (SHE)	$\dot{Q}_{\text{SHE}} = \dot{m}_{\text{wf}}(h_{2(\text{sc})} - h_1)$	TPC
Expander (EXP)	$\dot{W}_{\text{EXP}} = \dot{m}_{\text{wf}}(h_2 - h_{3,\text{is}})\eta_{\text{EXP,is}}$ $\eta_{\text{EXP,is}} = (h_2 - h_3)/(h_2 - h_{3,\text{is}})$	all cycles
Condenser (CDS)	$\dot{Q}_{\text{CDS}} = \dot{m}_{\text{wf}}(h_3 - h_4)$	all cycles
Pump (PMP)	$\dot{W}_{\text{PMP}} = \dot{m}_{\text{wf}}(h_{1,\text{is}} - h_4)/\eta_{\text{PMP,is}}$ $\eta_{\text{PMP,is}} = (h_{1,\text{is}} - h_4)/(h_1 - h_4)$	all cycles

For TPC, using a supercritical heat exchanger (SHE) plays a key role as it is an essential component to harness the temperatures from the heat sources and to increase the temperature of working fluid above its critical pressure and temperature. When a heat transfer process operates under supercritical pressure (just above the critical point), it is crucial to account for the effects known as supercritical (or Widom) anomalies [95]. These anomalies can significantly impact the process and consequently affect the design of heat exchangers. This type of heat addition process is often referred to as pseudo-boiling because the properties of the fluid undergo rapid changes that, although not as abrupt, are similar to those seen in actual boiling [96, 97, 98]. As a result, the heat exchanger must accommodate quick changes in volume expansion, comparable to what occurs in subcritical evaporators during boiling. The design of the entire system must be adapted to manage these dynamic changes effectively.

To provide clear information, the design details of the heat exchanger, which heats and changes the phase of the working fluid in each cycle, are presented in Table 3.2. This table employs a matrix layout to outline the components in the process 1 → 2 across different cycles. The comparison of heat exchangers for sup-ORC and TPC is also given. Including a superheater in the ORC system introduces an additional heat transfer step in the process. In addition, the cycle efficiency of both sup-ORC and TPC can be calculated using the equations that are listed in Table 3.3.

Table 3.2. A configuration matrix of the heat exchanger process 1 → 2 for each cycle, including sup-ORC and TPC.

Cycle	LH	PE	EVA	SUP	SHE	Energy balance process 1 → 2
TFC	x	-	-	-	-	$\dot{Q}_{\text{HE,TFC}} = \dot{Q}_{\text{LH}}$
PE-ORC	x	x	-	-	-	$\dot{Q}_{\text{HE,PE-ORC}} = \dot{Q}_{\text{LH}} + \dot{Q}_{\text{PE}}$
ORC	x	-	x	-	-	$\dot{Q}_{\text{HE,ORC}} = \dot{Q}_{\text{LH}} + \dot{Q}_{\text{EVA}}$
sup-ORC	x	-	x	x	-	$\dot{Q}_{\text{HE,sup-ORC}} = \dot{Q}_{\text{LH}} + \dot{Q}_{\text{EVA}} + \dot{Q}_{\text{SUP}}$
TPC	-	-	-	-	x	$\dot{Q}_{\text{HE,TPC}} = \dot{Q}_{\text{SHE}}$

Table 3.3. Cycle efficiencies of selected thermodynamic power cycles including sup-ORC and TPC.

Cycle	Efficiency of the cycle
TFC	$\eta_{\text{TFC}} = (\dot{W}_{\text{EXP,TFC}} - \dot{W}_{\text{PMP,TFC}})/\dot{Q}_{\text{HE,TFC}}$
PE-ORC	$\eta_{\text{PE-ORC}} = (\dot{W}_{\text{EXP,PE-ORC}} - \dot{W}_{\text{PMP,PE-ORC}})/\dot{Q}_{\text{HE,PE-ORC}}$
ORC	$\eta_{\text{ORC}} = (\dot{W}_{\text{EXP,ORC}} - \dot{W}_{\text{PMP,ORC}})/\dot{Q}_{\text{HE,ORC}}$
sup-ORC	$\eta_{\text{sup-ORC}} = (\dot{W}_{\text{EXP,sup-ORC}} - \dot{W}_{\text{PMP,sup-ORC}})/\dot{Q}_{\text{HE,sup-ORC}}$
TPC	$\eta_{\text{TPC}} = (\dot{W}_{\text{EXP,TPC}} - \dot{W}_{\text{PMP,TPC}})/\dot{Q}_{\text{HE,TPC}}$

3.2. Discussion and main contributions

3.2.1. The effect of increased operating temperature and pressure ratio range in working fluid expansion process using wet working fluids

In this chapter, propane is retained as the representative wet working fluid. The model simulation is conducted at a constant lower temperature T_4=231.03 K, corresponding to the boiling point of propane at atmospheric pressure. This boiling point is selected to assess the cycle efficiency without the necessity of integrating specialized vacuum pumps into the system. However, it is possible to design a cycle below this temperature, but a proper design of the vacuum pump needs to be carefully taken into account. Setting T_4=231.03 K is also beneficial to assess the efficiency of the system designed for utilizing cold energy. In that case, the system uses the cold energy as a heat sink. Moreover, the model simulation sets an upper-temperature range starting from 291.04 K, which is 60 K higher than T_4, extending up to 500 K. This upper limit of 500 K was carefully chosen to remain below the ignition point of propane, in line with the findings of a recent study [99] that investigated the critical factors influencing ignition of propane.

Fig. 3.4 presents the result of the modeling simulation using propane as a wet working fluid. These results were obtained under the assumption of isentropic efficiencies of both the pump and the expander equal to 1, indicating the ideal conditions. It shows that by raising the temperature of the working fluid at the inlet to the expander, the cycle efficiency of the system may be enhanced. This improvement is observed in the transition from subcritical power cycles (ORC, PE-ORC, and sup-ORC) towards TPC, which is illustrated by the shift in the line color of cycle efficiency from blue or magenta to red in Fig. 3.4. An interesting observation from the results displayed in Fig. 3.4 is the presence of equal efficiency points (EEPs) using different systems. At temperatures T_4=231.03 K and T_2=369.84 K, a sup-ORC with $x_{\text{3,is}}$=0.9 reaches an efficiency 0.236, identical to that of ORC. More EEPs are observed not only in subcritical cycles but also in TPC, as it is highlighted by the magnified rectangles in Fig. 3.4.

Furthermore, the modeling simulation was carried out with $x_{\text{3,is}}$=1.0 and other specific vapor qualities. From this approach, three novel descriptors related to the characteristics of the working fluid can be observed to offer insight for selecting and optimizing the design based on chosen working fluids. The descriptors are outlined as follows:

- The marker ’SS’ refers to EEP where a sup-ORC with $x_{\text{3,is}}$=1.0 and specially configured PE-ORC with a specific $x_{\text{3,is}}$ reach identical cycle efficiency at a certain temperature in $\eta_{\text{cycle}} - T_2$ diagram. The specific point corresponds to a specific configuration of the cycle where an ideal expansion path intersects precisely with a critical point on the $T - s$ diagram, as it is illustrated in Fig. 3.2(c). As an example using propane illustrated in Fig. 3.4, at temperatures T_4=231.03 K and T_2=ca. 339.16 K, a PE-ORC with $x_{\text{3,is}}$=0.7842 archives the same cycle efficiency 0.236 as a sup-ORC with $x_{\text{3,is}}$=1.0, when both simulate under ideal conditions.
- The marker ’TT’ refers to EEP where sup-ORC or TPC with $x_{\text{3,is}}$=1.0 with a specific $x_{\text{3,is}}$ (which corresponds to a specific configuration of the cycle where an ideal expansion path intersects precisely with a critical point on the $T - s$ diagram, as illustrated in Fig. 3.2(c)) reach identical cycle efficiency at a certain temperature in $\eta_{\text{cycle}} - T_2$ diagram. As an example using propane illustrated in Fig. 3.4, at temperatures T_4=231.03 K and T_2 of around 441.23 K, a TPC with $x_{\text{3,is}}$=0.7842 archives the same cycle efficiency ca. 0.319 as a TPC with $x_{\text{3,is}}$=1.0 when both simulate under ideal conditions.

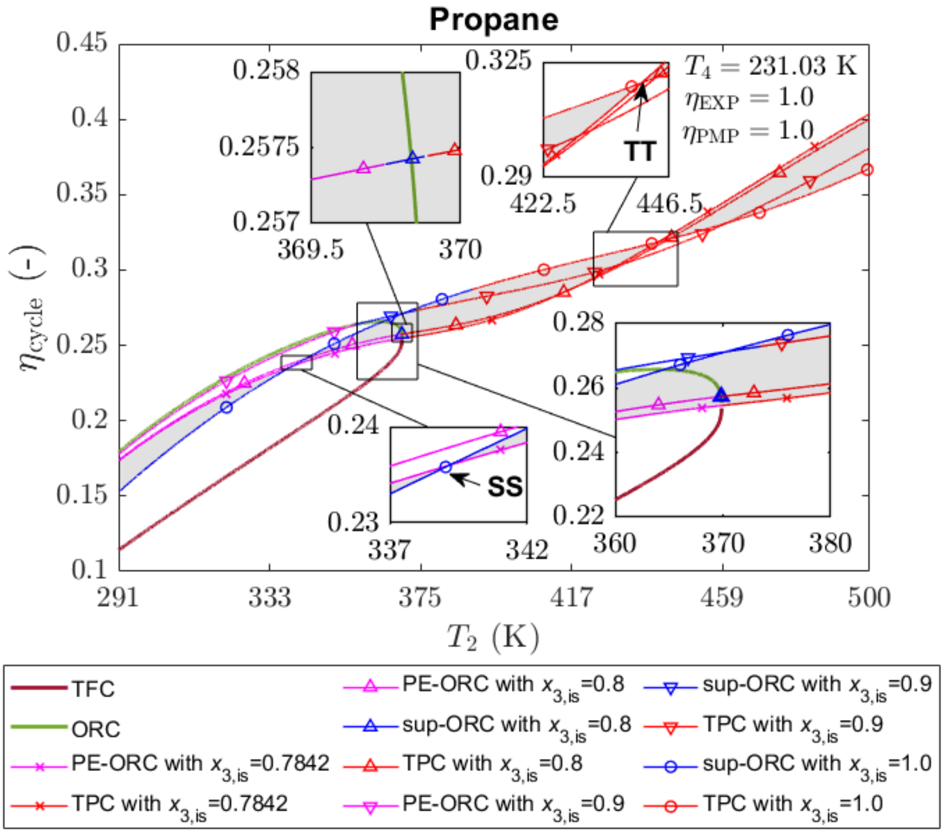

Fig. 3.4. Cycle efficiency of ORC, PE-ORC, sup-ORC, and TPC under ideal operating condition using propane as the wet working fluid in $\eta_{\text{cycle}} - T_2$ diagram, adopted from [6, 92]. It is worth noting that for a detailed comparison of cycle efficiency in selected different ORC systems operating below the saturated vapor-liquid curve (e.g., ORC, PE-ORC, and TFC), refer to [86].

- An 'ideal identity' band marks the zone where PE-ORC, sup-ORC, or TPC with $x_{3,\text{is}}$=1.0 could outperform other cycles with $x_{3,\text{is}}$<1.0 within certain temperature ranges (between markers 'SS' and 'TT'). An example using propane is illustrated in Fig. 3.4, where a grey-shaded region illustrates this concept between temperatures T_2=339.16 K and T_2=441.23 K.

The three new descriptors, namely 'SS', 'TT', and 'ideal identity' band markers described above, are also observed for common wet working fluids such as R1234zf, R134a, RE143a, and R161 under ideal conditions. These findings have been documented in the publication [6]. In the study for R161 [6], the descriptor 'SS' falls within the supercritical range, positioned beyond the area enclosed by the cycle efficiency curves of TFC and ORC. The lowest temperature influences the placement of these points in the cycle. By setting this minimum temperature to a specific value — such as the average temperature of the environment, the triple point, or the melting point of the fluid in question — the temperatures at these points can effectively be treated as characteristics inherent to the material. In addition, when incrementally raising the temperature by T_4=40 K, in increment steps 10 K, the typical descriptors remain identifiable. This observation is detailed in the part of the study in [6].

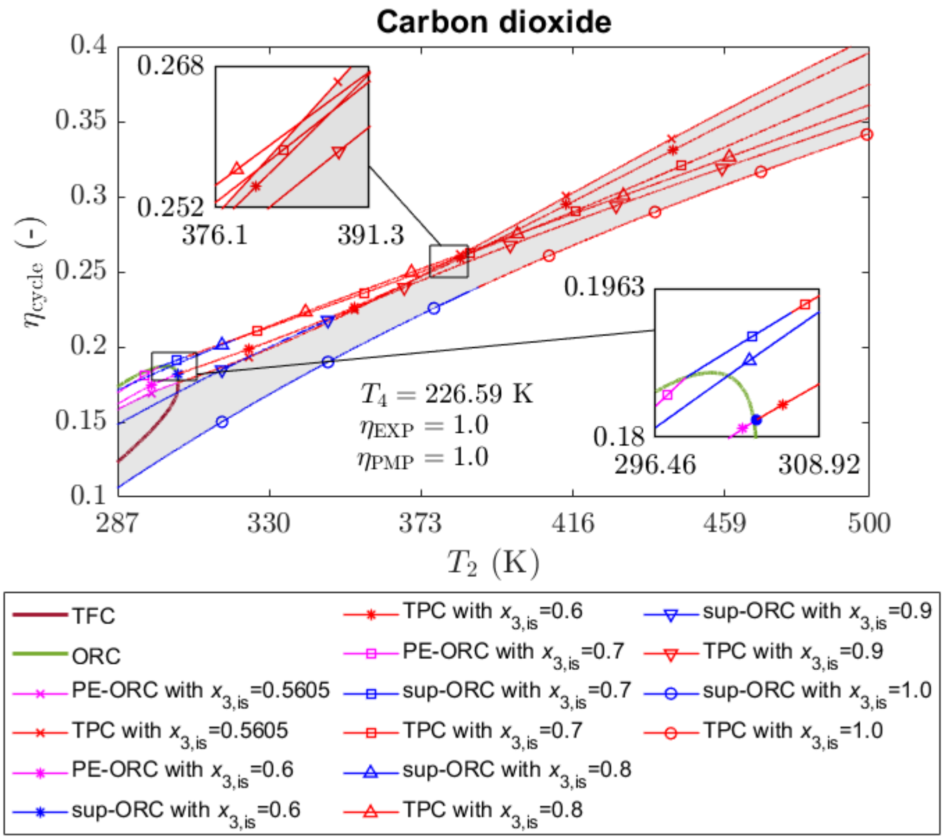

Fig. 3.5. Efficiency of ORC, PE-ORC, sup-ORC, and TPC under ideal operating condition using carbon dioxide as representative wet working fluid in $\eta_{\text{cycle}} - T_2$ diagram, adopted from [6, 93, 92]. It is worth noting that for a detailed comparison of cycle efficiency in selected different ORC systems operating below the saturated vapor-liquid curve (e.g., ORC, PE-ORC, and TFC), refer to [86].

Furthermore, it seems that typical wet working fluids do not have the typical topology and shape of their 'ideal identity' band. As it can be seen in Fig. 3.5, there is a different observation when the modeling simulation employed carbon dioxide as the wet working fluid. The markers 'SS' and 'TT' can not be located, also there is a different shape of the 'ideal identity' band, which is indicated by the grey-shaded region in Fig. 3.5. A similar phenomenon was observed when the simulation used water as a wet working fluid described in [6]. Moreover, the part of the study in [6] notes that when the temperature T_4 is gradually increased by 40 K, using increments 10 K, the typical descriptors (both 'SS' and 'TT') in carbon dioxide and water still become unidentifiable, and the 'ideal identity' band remains in different shape and topology compared to propane and other wet working fluids such as R1234zf, R134a, RE143a, and R161. A summary of the results is given in Table 3.4. It is important to note that although the type of the working fluid remains the same, the 'TT' and 'SS' points illustrated in $\eta_{\text{cycle}} - T_2$ diagram are not necessarily the same as it was observed using propane, carbon dioxide, and water as wet working fluids. This is due to the different course in the isobaric evaporation curve of the working fluid [92].

From the results using propane, carbon dioxide, and other working fluids de-

Table 3.4. Presence of novel descriptors under ideal conditions in selected working fluids, adopted from [6].

Working Fluid	EEP 'SS'	EEP 'TT'	An 'ideal identity' band
Propane	x	x	There is a zone where PE-ORC, sup-ORC, or TPC with $x_{3,\text{is}}$=1 could outperform other cycles with $x_{3,\text{is}}$<1 within a certain temperature ranges (between markers 'SS' below critical temperature and 'TT' above critical temperature), as illustrated in Fig. 3.4.
R1243zf	x	x	There is a zone where PE-ORC, sup-ORC, or TPC with $x_{3,\text{is}}$=1 could outperform other cycles with $x_{3,\text{is}}$<1 within a certain temperature ranges (between markers 'SS' below critical temperature and 'TT' above critical temperature).
R134a	x	x	There is a zone where PE-ORC, sup-ORC, or TPC with $x_{3,\text{is}}$=1 could outperform other cycles with $x_{3,\text{is}}$<1 within a certain temperature ranges (between markers 'SS' below critical temperature and 'TT' above critical temperature).
RE143a	x	x	There is a zone where PE-ORC, sup-ORC, or TPC with $x_{3,\text{is}}$=1 could outperform other cycles with $x_{3,\text{is}}$<1 within a certain temperature ranges (between markers 'SS' below critical temperature and 'TT' above critical temperature).
R161	x	x	There is a zone where sup-ORC or TPC with $x_{3,\text{is}}$=1 could outperform other cycles with $x_{3,\text{is}}$<1 within a certain temperature ranges (between markers 'SS' above critical temperature and 'TT' above critical temperature).
Carbon dioxide	-	-	There is a zone where sup-ORC and TPC with $x_{3,\text{is}}$=1 offer the lowest efficiency compared to other cycles, as illustrated in Fig. 3.5.
Water	-	-	There is a zone where sup-ORC and TPC with $x_{3,\text{is}}$=1 offer the lowest efficiency compared to other cycles.

scribed in [6] as examples of typical wet working fluids, it is important to highlight that the maximal cycle efficiency of ORC still can be located using different operating temperature ranges of the cycle. It is suggested that the maximal cycle efficiency of the ORC plays a crucial role in the design of a thermal power plant. When using typical wet working fluids, it is advisable to avoid approaching the critical point with TPC as their efficiency is lower compared to the maximal cycle efficiency of ORC. This recommendation also extends to certain configurations of PE-ORC and sup-ORC with T_2 near the critical point.

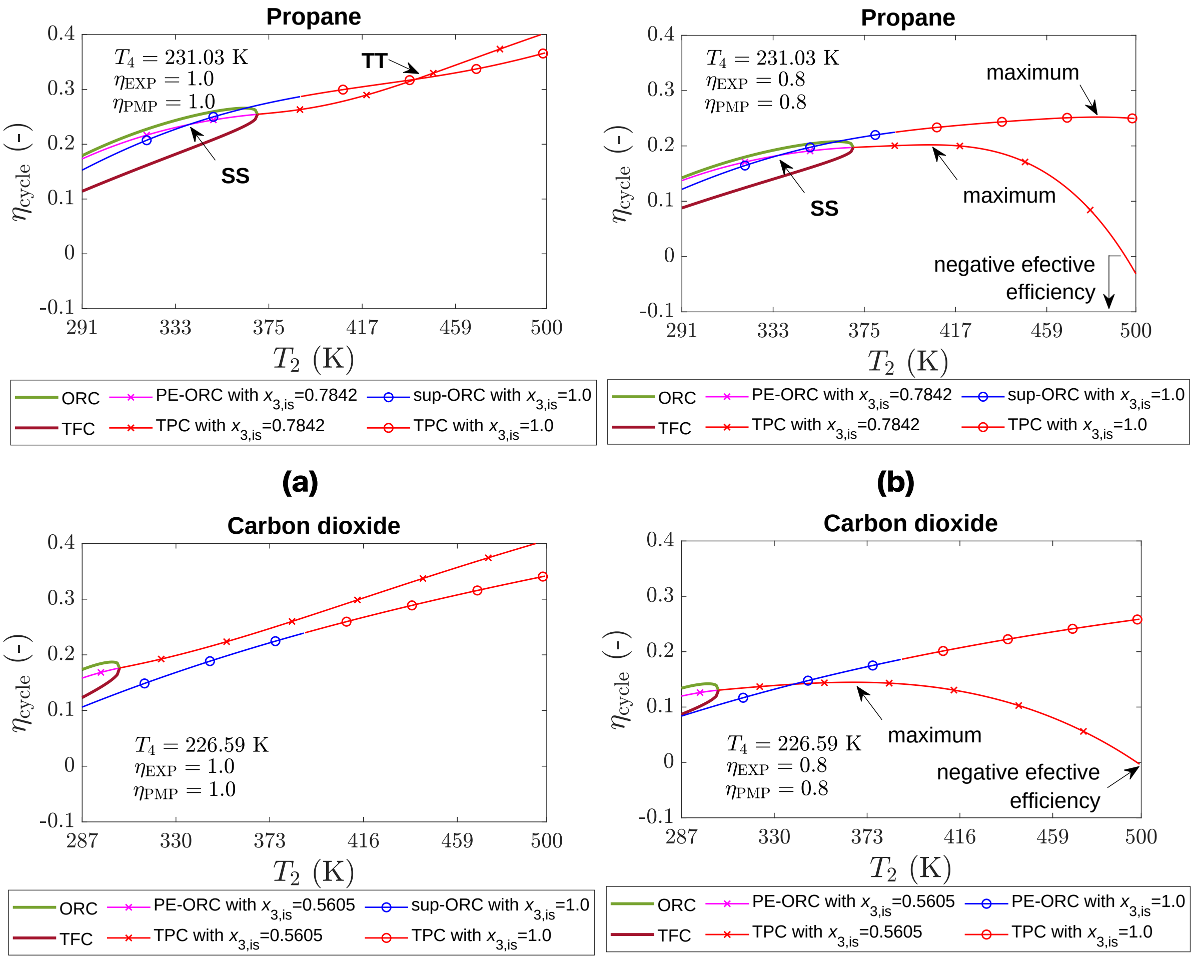

(a) **(b)**

(c) **(d)**

Fig. 3.6. The result of modeling simulation using **(a)-(b)** propane and **(c)-(d)** carbon dioxide, adopted from [6, 92]. It is important to note that the diagram on the left illustrates the thermodynamic operation under ideal conditions. In contrast, the diagram on the right accounts for the thermodynamic operation with an isentropic efficiency of 0.8 for both the expander and the pump. It is worth noting that for a detailed comparison of cycle efficiency in subcritical power cycles (e.g., ORC, PE-ORC, and TFC) operating below the saturated vapor-liquid curve, refer to [86].

This study expands its analysis by comparing ideal conditions with scenarios in which the isentropic efficiencies of both the pump and the expander are set to 0.8. The results and comparative analysis are depicted in Fig 3.6. Propane and carbon dioxide are selected for demonstration. The analysis includes ORC and TFC simulations along the saturation curve. The modeling simulations discussed in Figs. 3.2(a) and (c) were taken into consideration. The results presented in Figs. 3.6(a) and (c) are similar to the prior result under ideal conditions, offering a basis for comparison. In an ideal scenario, novel descriptors are identified. However, when adjusting for the isentropic efficiencies of the expander and pump at 0.8, the results of modeling simulation using propane differ in the topology and shape. In this scenario, only the 'SS' marker remains in $\eta_{\text{cycle}} - T_2$ diagram, as illustrated in 3.6(b). For carbon dioxide, under ideal conditions, these novel descriptors are absent. However, with isentropic efficiencies set to the value of 0.8, the EEP is recognized between the sup-ORC $x_{3,\text{is}}$=1.0 and TPC and $x_{3,\text{is}}$=0.5605, as depicted in Fig. 3.6(d).

It is important to understand that raising the temperature of the working fluid at the inlet to the expander does not guarantee higher cycle efficiency for TPC, which has been demonstrated by propane and carbon dioxide as exemplary. This evidence is shown in Figs. 3.6(b) and 3.6(d). It seems that the maximal cycle efficiency of TPC can be located in this case. Using propane, the maximal efficiency of TPC with $x_{3,\text{is}}$=0.7842 and $x_{3,\text{is}}$=1.0 can be observed in Fig. 3.6(b) between T_2=405 K and T_2=482.36 K, respectively. Moreover, using carbon dioxide, the maximal cycle efficiency of TPC with $x_{3,\text{is}}$=0.5605 can be found in Fig. 3.6(d) at T_2=ca. 367.22 K. Although 3.6(d) does not clearly show the maximal cycle efficiency of TPC with $x_{3,\text{is}}$=1.0, by increasing the T_2, this peak cycle efficiency can be identified at ca. 724.22 K. Nevertheless, it is crucial to note that cycle efficiency starts to decline after reaching these peak values. Moreover, it is important to note that Fig. 3.6(b) demonstrates the negative effective efficiency observed in the TPC process when the parameter $x_{3,\text{is}}$=0.7842, particularly at temperatures T_2>495 K. The term 'negative effective cycle efficiency' describes the operational efficiency of a cycle, assuming a constant mass flow rate through its components. It is calculated by determining the difference in enthalpy changes between the expander, where specific energy is generated, and the pump, where specific energy is used. This difference, reflecting the net output energy, is then compared to the heat input energy. Essentially, it measures the efficiency of the system by contrasting the useful output energy with the total input energy. This unusual condition arises if the energy required to operate the pump exceeds the energy produced by the expander. For instance, a situation can be considered where the operating condition is set with temperatures T_2=500 K and T_4=231.03 K, under the assumption that the pressure differences for both the pump and the expander are identical. Similar unusual phenomena were observed using other working fluids, which part of the study was described in [92].

3.2.2. The effect of increased operating temperature and pressure ratio range in working fluid expansion process using isentropic working fluids

This investigation broadens the scope of analysis by incorporating isentropic working fluids. It is important to note that the developed methodology does not apply to all isentropic fluids. For this investigation, butane and isobutane were selected as examples. The choice was based on their reasonable saturated vapor curve, whose shape is almost like that of a wet working fluid and aligns well with the parameters of this analysis. Both working fluids are categorized as HC and several studies are discussing the use of HC for ORC and other thermal power plants.

The modeling simulation using isentropic working fluid is likely similar to the prior investigation using the wet working fluid described above, which details the ideal conditions and isentropic efficiencies for both the pump and the expander to the value of 0.8. Here, the temperature T_4 is set at the boiling point under atmospheric pressure. The range for T_2 begins 60 K above the boiling point, extending up to 500 K. For isobutane specifically, the upper-temperature limit is capped at 460 K, a restriction dictated by the limitations within the available thermal properties library.

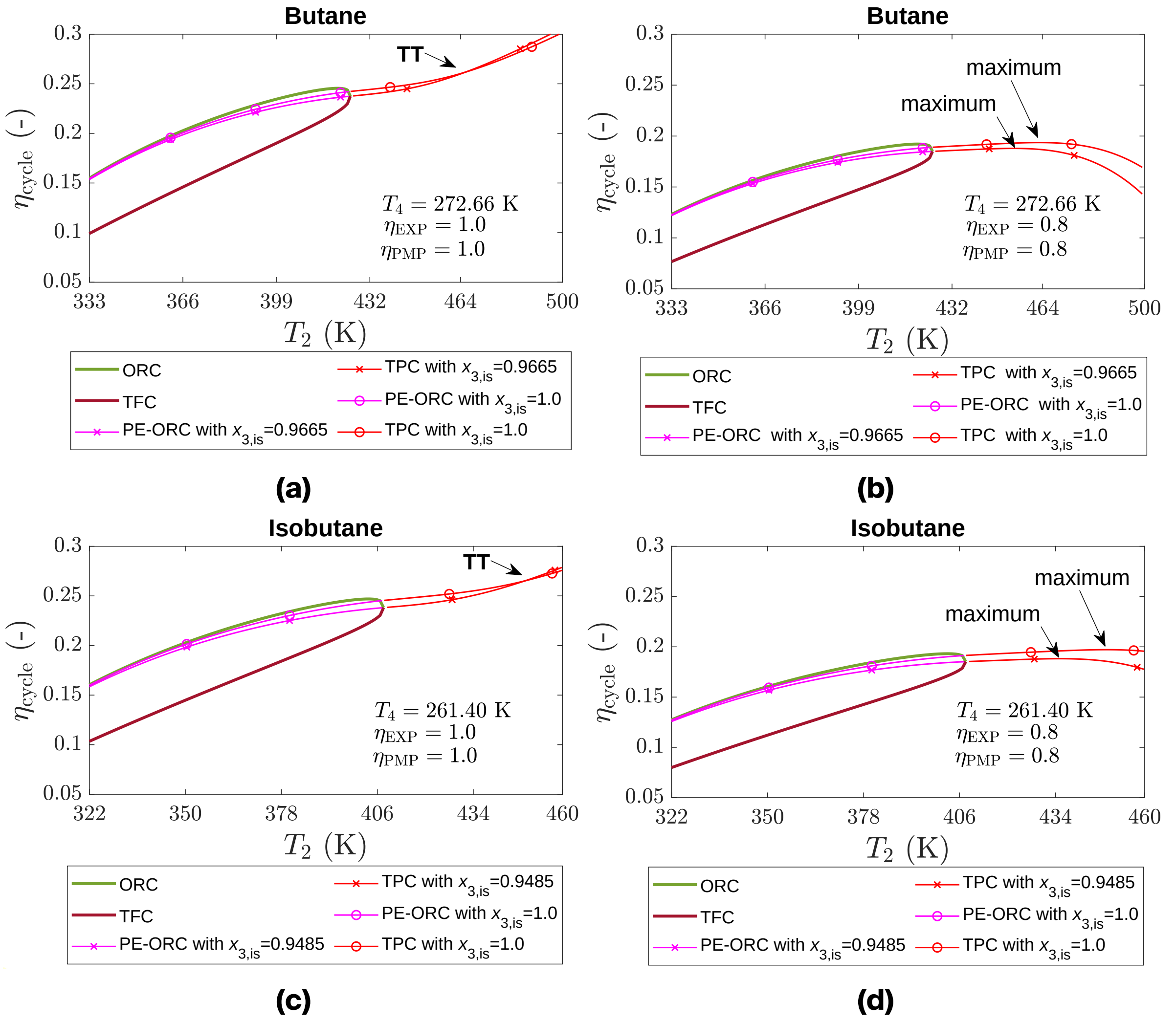

(a) **(b)**

(c) **(d)**

Fig. 3.7. The result of modeling simulation using **(a)-(b)** butane and **(c)-(d)** isobutane as exemplary of isentropic working fluids, adopted from [6, 92]. It is important to note that the diagram on the left illustrates the thermodynamic operation under ideal conditions. In contrast, the diagram on the right accounts for the thermodynamic operation with an isentropic efficiency of 0.8 for both the expander and the pump. It is worth noting that for a detailed comparison of cycle efficiency in subcritical power cycles (e.g., ORC, PE-ORC, and TFC) operating below the saturated vapor-liquid curve, refer to [86].

The results for both butane and isobutane are displayed in Fig. 3.7, showcasing the cycle efficiency of ORC and TFC along with the saturated curve. This analysis incorporated the modeling simulation details in Figs. 3.2(a) and (c). Under ideal conditions, the outcomes reveal similar circumstances where novel descriptors exist. However, it is important to note that the 'ideal identity' band, as depicted in Figs. 3.7(a) and (c) is quite narrow. Moreover, the 'SS' marker is not identifiable within the current operating temperature range. However, the findings suggest that by adjusting the temperature range, the existence of this EEP can indeed be pinpointed. In the case of butane, the inlet condition to the expander is very close to its critical point. However, these conditions are definitely located on the saturated vapor curve. Therefore, this process is classified as PE-ORC, although due to the very minor evaporation part, it is very similar to a TFC.

Furthermore, by setting the isentropic efficiencies of both the pump and expander at 0.8, the peak efficiency of the TPC can be determined. For instance, in this study, the maximal cycle efficiency for butane in the TPC, marked by $x_{3,\mathrm{is}}$=0.9665 and $x_{3,\mathrm{is}}$=1, corresponds to T_2=ca. 454.12 K and T_2=463.19 K, respectively. In the case of isobutane, the peak efficiencies for TPC at $x_{3,\mathrm{is}}$=0.9485 and $x_{3,\mathrm{is}}$=0.1 occur at T_2=434.82 K and T_2=448.82 K, respectively. A consistent trend is observed across both fluids: the cycle efficiency of TPCs declines after it hits this maximum point with further increases in the temperature of the working fluid to the inlet to the expander.

3.3. Conclusions

This chapter details a theoretical analysis through modeling simulations designed to assess the cycle efficiency of diverse subcritical cycles. It specifically explores the impact of increasing the working fluid's inlet temperature at the expander, a key factor that facilitates the transition from subcritical power cycles to TPC. The approach and process of these modeling simulations are outlined, together with an explanation of the mathematical models employed. This research acts as a foundational comparison for comparing the cycle efficiency of subcritical power cycles and TPC based on selected working fluids. Carnot cycle suggests that increasing the operating temperature range of a cycle could improve its overall efficiency. This concept proves to be valid across specific temperature ranges for both subcritical power cycles (ORC, PE-ORC, and sup-ORC) and TPC, utilizing a variety of working fluids. Moreover, the main contributions of this chapter are elaborated in Thesis 3 and Thesis 4, as detailed below.

Thesis 3. *Under ideal operating conditions (i.e., considering isobaric evaporation, isentropic expansion, isobaric condensation, and isentropic pump process), an increased operating temperature range of the low-boiling working fluid expansion process in the organic Rankine cycle (ORC), partially evaporated ORC, ORC with a superheater, and trilateral flash cycle likely enhances cycle efficiency. This approach also applies to the transcritical power cycle (TPC). Nonetheless, when taking the isentropic efficiency of the expander into account, a maximal cycle efficiency point for TPC can be observed. This maximal cycle efficiency of TPCs underscores the significance of selecting an optimal temperature range and pressure ratio of the low-*

boiling working fluid expansion process and type of thermodynamic power cycle, providing perspectives on the decision-making process for utilizing organic working fluids.

The publications by the author that are related to Thesis 3 are [6, 86, 92, 93].

Thesis 4. *In evaluating the cycle efficiency of various transcritical power cycle (TPC) configurations with different values of vapor quality from the expander outlet, using either wet or isentropic working fluids, an equal efficiency point (EEP) can typically be identified under ideal operating conditions (i.e., considering isobaric evaporation, isentropic expansion, isobaric condensation, and isentropic pump process). However, when employing carbon dioxide or water as working fluids, this EEP cannot be located. Moreover, a scenario may arise where the TPC exhibits negative efficiency, especially when considering higher operating temperature and pressure ratio ranges of the low-boiling working fluid expansion process, along with the isentropic efficiency of the expander. As an example, if the isentropic efficiency were set to the value of 0.8, this negative TPC efficiency would occur as the enthalpy change in the expander is lower than the enthalpy change in the pump. This example theoretically proves that increasing the operating temperature and pressure ratio range of the low-boiling working fluid expansion process does not guarantee an improvement in cycle efficiency.*

The publications by the author that are related to Thesis 4 are [6, 86, 92, 93].

4

Experimental study and artificial intelligent-based analysis of two-phase expander operating in ORC system

In engines or turbines, using a mix of liquid and vapor (two-phase condition) is usually avoided during the expansion process because of some common problems. These problems include liquid forming inside steam engines and the risk of damaging the blades in turbines by liquid droplets that are flowing with gas at high velocity. Despite these issues, recent studies suggest that certain types of engines, known as volumetric expanders (e.g., screw, scroll, piston, vane, and Wankel machines), might be good alternatives to other types of machines under two-phase conditions. These volumetric expanders can expand the mixture of liquid and vapor and can be successfully applied in the ORC systems. Moreover, ORC systems with two-phase expansion (PE-ORC) or TFC have demonstrated superior performance over conventional ORC systems, which has been theoretically described in Chapters 2 and 3. In addition, an organic flash cycle (OFC) introduces a design improvement by incorporating a separator within the cycle [100]. This separator in OFC is applied to separate the liquid phase from the vapor phase following the pre-heating of the working fluid at a certain temperature and pressure. While the vapor phase of the working fluid is directed into an expander, the liquid is set towards a throttle valve. This throttle valve can be replaced with a two-phase expander, which can result in improved OFC system efficiency [101].

Recent literature has seen growing interest from researchers in incorporating two-phase expanders due to their potential benefits. Some studies have explored the use of a scroll [102], screw [103], piston [52], and Wankel expanders for a thermodynamic power cycle under two-phase conditions. It seems that vane expanders have also been tested under two-phase conditions, but typically it is linked with refrigeration cycles. One particular study [104] focused on a vane expander working with a transcritical refrigeration cycle using carbon dioxide as a working fluid. The research noted some pressure fluctuations and identified a specific point where the pressure was noticeably inflected.

Chapter 4 aims to prove that a multi-vane expander can be employed for ORC systems operating under two-phase conditions. Also, it aims to investigate the performance of a two-phase multi-vane expander employed in an ORC system. The choice of focusing on a multi-vane expander is due to a noticeable lack of experimental studies on two-phase expanders, placing this investigation as a state of the art. Moreover, since 1996, the Department of Thermodynamics and Renewable Energy Sources at Wrocław University of Science and Technology has been conducting research on ORC systems utilizing multi-vane expanders [65]; therefore, to further this research at the department, multi-vane expander has been chosen. A preliminary study [58] also shows that a multi-vane expander can operate under two-phase conditions. Moreover, this chapter introduces a novel approach by combining experimental methods with artificial intelligence techniques. This innovative method represents a significant advancement, offering a sophisticated means to assess the condition and predict the performance of two-phase expanders. Such a method could enable early identification of potential issues or limitations within experimental setups, paving the way for more efficient and effective research and development in this field.

4.1. System description and research methodology

4.1.1. The description of experimental test-stand system

This research was conducted using an experimental system developed at the Laboratory of Thermodynamics and Thermal Properties of Materials, located at Wrocław University of Science and Technology, Poland. The heat source for the system is hot water taken from a gas central heating boiler. Moreover, two plate heat exchangers were used as an evaporator (with a heat transfer surface of ca. 7.5 m^2) and condenser (with a heat transfer surface of ca. 0.5 m^2), respectively. A modified version of a multi-vane air motor served as the expander in the setup, capable of producing a maximum output power of ca. 300 W. A multi-vane pump featuring the required input power of 185 W was used to pump the liquid working fluid through the test-stand components. The ORC test stand used R123 as the working fluid. The test-stand system was specially prepared for the present research. The general view of the test stand and its schematic are shown in Fig 4.1(a). A set of working fluid valves and a small double-pipe heat exchanger were installed in the system (between the evaporator and the expander). Some measurement systems, including sensors to assess vapor quality and a device to measure torque/rotational speed, were installed in the system. The focus of the investigation was to examine a multi-vane expander. The key technical specifications of the multi-vane expander are provided in Table 4.1, and the cross-section and general view of the expander are depicted in Fig. 4.1(a) and 4.1(b). The expander consists of a rotor, cylinder, eight vanes, two side covers, two bearings, and shaft sealing. Since the expander is the main concern, several measurements were conducted, including the pressure, vapor quality, and temperature at the inlet and at the outlet from the expander. The rotational speed of the expander and torque were also measured. All measurement devices used in this investigation are listed and detailed in Table 4.2.

Precise temperature and pressure sensors were installed in the test setup to en-

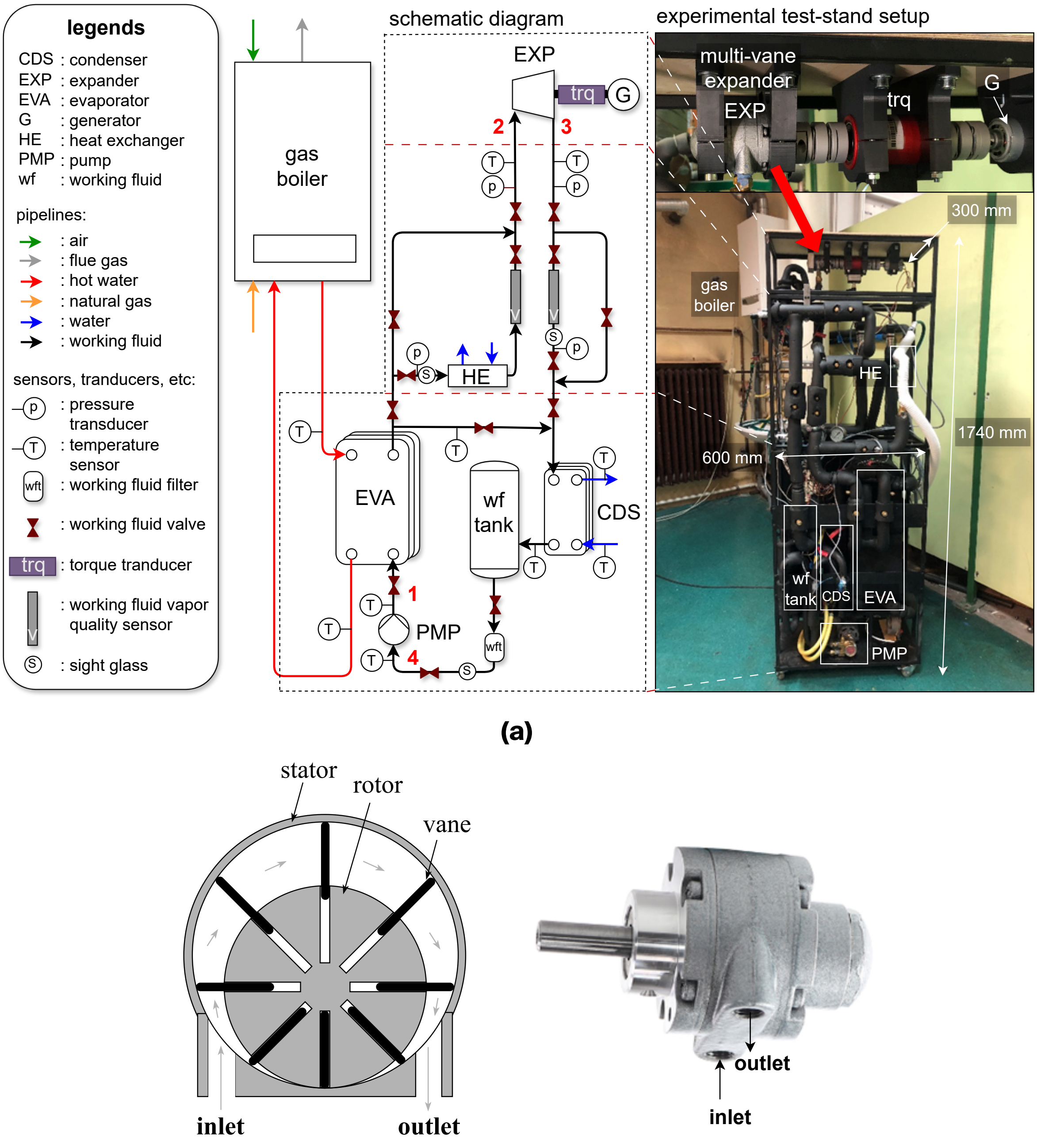

(a)

(b) **(c)**

Fig. 4.1. Illustration of **(a)** the experimental test-stand setup with schematic diagram, and a two-phase multi-vane expander in **(b)** structure diagram, and **(c)** the illustration showing the exterior of the expander without any view of its internal structure [105].

sure the high accuracy of measurements. Working fluid vapor quality sensors were installed in pipelines connecting the expander with the condenser and evaporator. These sensors, placed at the inlet to and the outlet from the expander, facilitate real-time measurement of vapor quality, thus enabling a more detailed assessment of the expander's performance. In addition, a torque transducer was installed in the system to measure the rotational speed and torque of the expander. The torque transducer was connected to the expander and a small generator via clutches. For experimental data management, all measurements were recorded and monitored using the LUMEL KD-7 recorder, serving as the central data acquisition station. To

Table 4.1. List of measurement devices used in this experimental investigation [105].

Description	Specification
Max. operating temperature	393.15 K
Max. output power	300 W
Max. pressure	7 MPa
Max. rotational speed	10,000 rpm
Number of vanes	8
Weight	0.91 kg
Dimension	56.4 × 108 × 62 mm

Table 4.2. List of measurement devices used in this experimental investigation [105].

Devices	Measured parameters	Specifications	Uncertainty
Pressure transducer	p	The model number is P499ACP-403C. It operates within T=233.15-353.15 K and p=0-1.5 MPa.	$\pm$ 1.00%
Temperature sensor	T	The models PT100 and PT1000 (classified as class A) are designed for operations with T<473.15 K.	$\pm$ 0.15 K
Torque transducer	τ and N	The DATAFLEX 16/50 model offers τ_{max}=50 Nm and can achieve N_{max}=10,000 rpm.	$\pm$ 0.10%
Vapor quality sensor	x	The model HBX-DX-HFC-SS-1/2 operates within T=213.15-353.15 K and can withstand p_{max}=10 MPa. It is designed for ambient temperatures ranging from 243.15 K to 323.15 K. This model is constructed from stainless steel.	$\pm$ 0.01
Rotameter	$\dot{V}$	The RDN-20 model is used for water with T=293 K at 0.1 MPa. This model offers the measurement $\dot{V}$<0.00027 m^2/s	$\pm$ 2.50%.

obtain a two-phase operating condition, a small double-pipe heat exchanger was introduced between the evaporator and the expander. This heat exchanger allowed for the cooling of the working fluid vapor with water as it passed through the inner pipe of the double-pipe heat exchanger. Such a setup enabled the creation of two-phase conditions for the working fluid at the inlet to the expander within a specific range of vapor quality, therefore facilitating more controlled experimental conditions. Moreover, a capacitive vapor quality sensor was utilized to determine the vapor quality in a two-phase flow between the double-pipe heat exchanger and the expander. The vapor quality sensor is also installed at the outlet from the expander. Moreover, the cooling water flow rate was measured using a rotameter which was installed at the outlet from the condenser.

4.1.2. The experimental study

Fig. 4.2 presents the representative process of an ORC test setup using blue lines. The numbers depicted in Fig 4.2 highlight the specific stages illustrated in Fig. 4.1. It illustrates the transition of the working fluid from a liquid to a two-phase state—part liquid and part vapor—as it moves through the evaporator, which is indicated by process $1 \rightarrow 2$. To achieve a two-phase state, by the time it reaches state 2, the fluid is slightly cooled by passing through a small double-pipe heat exchanger. Moreover, the working fluid continues the process $2 \rightarrow 3$ for a real expansion process, where it expands within a multi-vane expander. It is worth noting that the process $2 \rightarrow 3$,is refers to the isentropic expansion process. In this case, it is known as a wet isentropic expansion process, depicted by a dashed blue line, indicating the process occurs under wet conditions. Despite the real expansion process ending in a superheated (dry) state at point 3, it is possible to calculate the wet isentropic efficiency since part of the expansion happens in the two-phase condition. After expanding, the working fluid cools down and condenses, changing the phase to a liquid state (referring to condensation process $3 \rightarrow 4$). Following this, the fluid flows into the liquid tank. To complete the cycle in the closed-loop system, the working fluid is then pressurized by a pump from the liquid tank, which is indicated by process $4 \rightarrow 1$. In this case, the temperature of working fluid at the inlet to the pump was consistently kept at ca. 290.65 K.

The primary goal of this experiment was to assess the operational quality and operating conditions of a multi-vane expander under two-phase conditions. To achieve this aim, during the experiment, the heat source temperature was controlled between 318.15 K and 358.15 K, with adjustments made by 10.00 K steps using the boiler's controller settings. Despite these precise settings, periodic shifts were observed, causing temperatures to occasionally spike to as high as 361.93 K. Throughout the experiment, key thermodynamic parameters of the working fluids were recorded alongside other critical measurements, ensuring comprehensive monitoring of the test system's performance. The experiment maintained a constant heating water flow rate of ca. 0.04 kg/s, while the cooling water's flow rate was carefully regulated to ca. 0.14 kg/s, allowing for detailed analysis and control over the expander's testing conditions.

The main objective of the experiment was to analyze the quality and operational conditions of the expander when it is functioning under two-phase conditions. This

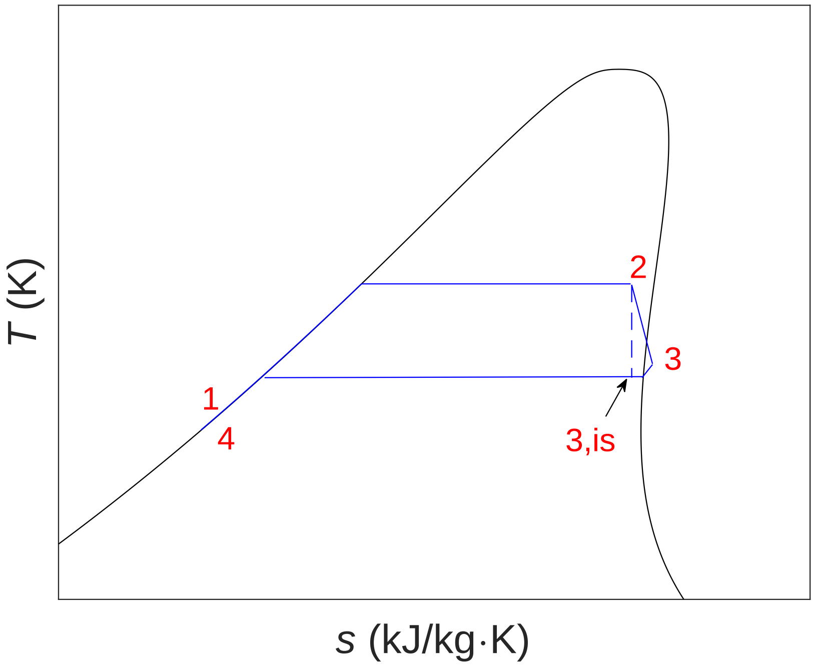

Fig. 4.2. Illustration of the process in the ORC test setup operating under a two-phase condition in the $T-s$ diagram adapted from [105]. The partial evaporation refers to process 1 $\rightarrow$ 2 and then followed by the isentropic expansion process 2 $\rightarrow$ 3_{is} and the real expansion process 2 $\rightarrow$ 3 are illustrated by the blue dashed line and the blue solid line, respectively. The liquefaction of the working fluid in the condenser refers to process 3 $\rightarrow$ 4. Then, the working fluid is pressurized in the process 4 $\rightarrow$ 1 is depicted by the blue solid line.

focus allows for the calculation of the expander's isentropic efficiency during the two-phase expansion process, also known as wet isentropic efficiency, based on the data collected from the experiment. By assuming that the mass flow rate of the working fluid remains constant at the inlet to and the outlet from the expander, it is possible to compute the estimated isentropic efficiency (η_{is}) in general using Eq. 4.1. It can also be used to estimate wet isentropic efficiency ($\eta_{\text{is,wet}}$). The wet isentropic efficiency evaluates how efficiently an expansion process operates when it starts in a two-phase (wet) state and ends in a vapor phase. It can also refer to a process where the substance stays in a two-phase condition throughout the expansion. In contrast, dry isentropic efficiency measures the efficiency of an expansion process that remains in a single phase, usually a superheated state, from start to finish. In this study, the calculation of enthalpy change was conducted using MATLAB, and the thermal properties of the working fluid were obtained from REFPROP 10.0 [88]. In addition, the measurement uncertainty is calculated using the method of partial derivatives, which is described in Eq. 4.2. This technique assesses the measurement uncertainty by looking into each contributing variable, taking into account the uncertainty associated with each variable to understand its collective impact on the total measurement uncertainty (u_{total}). Since the wet isentropic efficiency itself is determined by the ratio of enthalpy change, the primary factors are affected by temperature, vapor quality, and pressure of the working fluid. Therefore, the total measurement uncertainty for wet isentropic efficiency is influenced by the measurement uncertainty from temperature (u_T), vapor quality (u_x), and the pressure (u_p).

$$\eta_{\text{is}} = \frac{h_{\text{in,exp}} - h_{\text{out,exp}}}{h_{\text{in,exp}} - h_{\text{out,is,exp}}} \tag{4.1}$$

$$u_{\text{total}}(\eta_{\text{is,wet}}) = \sqrt{\left(\frac{\partial \eta_{\text{is,wet}}}{\partial T}\right)^2 u_{\text{T}}^2(T) + \left(\frac{\partial \eta_{\text{is,wet}}}{\partial x}\right)^2 u_{\text{x}}^2(x) + \left(\frac{\partial \eta_{\text{is,wet}}}{\partial p}\right)^2 u_{\text{p}}^2(p)} \tag{4.2}$$

4.1.3. Artificial intelligence for predicting wet isentropic efficiency of the two-phase expander

In this study, deep neural networks (DNNs) or deep learnings were utilized and developed within a MATLAB environment to predict the wet isentropic efficiency of a two-phase expander. DNN is a sophisticated data processing architecture that learns the relationships between input variables and their corresponding outputs by examining data from an established model. This predictive analysis was conducted based on the collected data from experimental research conducted on the ORC test setup as described earlier. The study took into account several indicators, such as pressure ratio, density ratio, vapor quality, temperature of the working fluid at the inlet to the expander, and the rotational speed of the expander.

A DNN consists of neurons that are linked together via weighted connections known as synaptic connections or synapses. Information flows and is processed across these connections. Each neuron receives input from neurons that came before it, processes this input by applying a specific transfer function, and then generates output that is forwarded to neurons that follow. The learning ability of a DNN stems from its capacity to iteratively adjust the weights of these synaptic connections based on the input and output data derived from the base model. This adjustment aims to minimize an error parameter, such as the mean square error (MSE) between the experimental data (Y_i) and predicted or validated data ($\hat{Y}_i$), described in Eq. 4.3. The training process, which fine-tunes the synaptic weights, continues until it fulfills a predetermined stopping criterion. This could be reaching a set number of training rounds, known as epochs. This iterative training and adjustment technique is critical for enhancing the DNN's accuracy in predicting or validating data, employing what is often called the no-stop training method.

$$MSE = \frac{1}{n}\sum_{i=1}^{n}(Y_i - \hat{Y}_i)^2 \tag{4.3}$$

This investigation employed feed-forward DNN (FFDNN) and cascaded forward DNN (CFDNN) with their structures depicted in Fig. 4.3. The FFDNN, a widely utilized structure within artificial neural networks, features a layered architecture, including an input layer, multiple hidden layers (more than three), and an output layer. The function of the input layer is to process external data (the independent variables), while the output layer produces the final results of the network (the objective functions). Positioned between these, one or more hidden layers play a pivotal role in learning capability. The number of hidden layers is critical for the accuracy of the model: too many layers may lead to overfitting, while too few can undermine the ability of the model to learn effectively. Overfitting happens when a model learns not only the underlying pattern in the training data but also the noise and random fluctuations. This typically results in the model memorizing the training data rather than generalizing from it. While adding more layers can increase computational times due to added complexity, the primary concern often remains with overfitting itself [106, 107]. In this study, three hidden layers were chosen to capture more complex features and representations which is a common practice in deep learning [106, 108]. The overall performance of a DNN model is significantly affected by the quality of input and output data, its structural design, and its parameters, all of which necessitate precise optimization. The CFDNN, similar to the FFDNN, introduces an additional mechanism where connections extend from the input layer and each preceding layer to all following layers. This architecture ensures that information flows not only from the immediately preceding layer but also directly from the input and all other preceding layers to each layer in the network. In Fig. 4.3, 'b' represents the bias, an essential parameter that adjusts the output in conjunction with the weighted inputs prior to applying the activation function. The bias facilitates the ability of the network to capture complex patterns more accurately. In addition, the weights in the network, crucial for modulating the signal strength between neurons, are fine-tuned during the learning process. The initial settings for both weights and biases were set to zero, emphasizing the role of the learning process in determining these values.

Some boundary conditions and initialization in this developed DNN are listed in Table 4.3. The developed DNN models employ two different training algorithms: Levenberg-Marquardt (LM) and Bayesian regularization (BR), resulting in four distinct model configurations (FFDNN with LM, CFDNN with LM, FFDNN with BR, and CFDNN with BR). The LM algorithm is chosen for its ability to speed up the training of the second-order methods without necessitating the computation of the Hessian matrix. On the other hand, the BR algorithm is utilized as an alternate training strategy, where it adjusts the weights and biases through LM optimization. Its main objective is to reduce the sum of squared errors and weights, identifying a balance that encourages the network to generalize well.

The architecture of the developed DNN includes three hidden layers and one output layer, each utilizing specific transfer functions. The first hidden layer and the output layer apply a linear transfer function, addressing the network's need to perform linear activations in scenarios involving regression analysis. This ensures that the network models the data relationships accurately for regression tasks. Meanwhile, the second and third hidden layers employ a log-sigmoid transfer function, beneficial for predictive modeling and extrapolation beyond the training data set. This non-linear function enables the network to identify and model complex data patterns, enhancing its predictive accuracy outside the trained range. Furthermore, the hidden layers were configured to contain between three to twenty neurons. The performance of the network was assessed using the root mean squared error (RMSE) and the coefficient of determination (R^2), as described in Eqs. 4.4 and 4.5. The final selection of neurons for each layer was determined through optimization, focusing on achieving the lowest RMSE during validation to ensure the best model perfor-

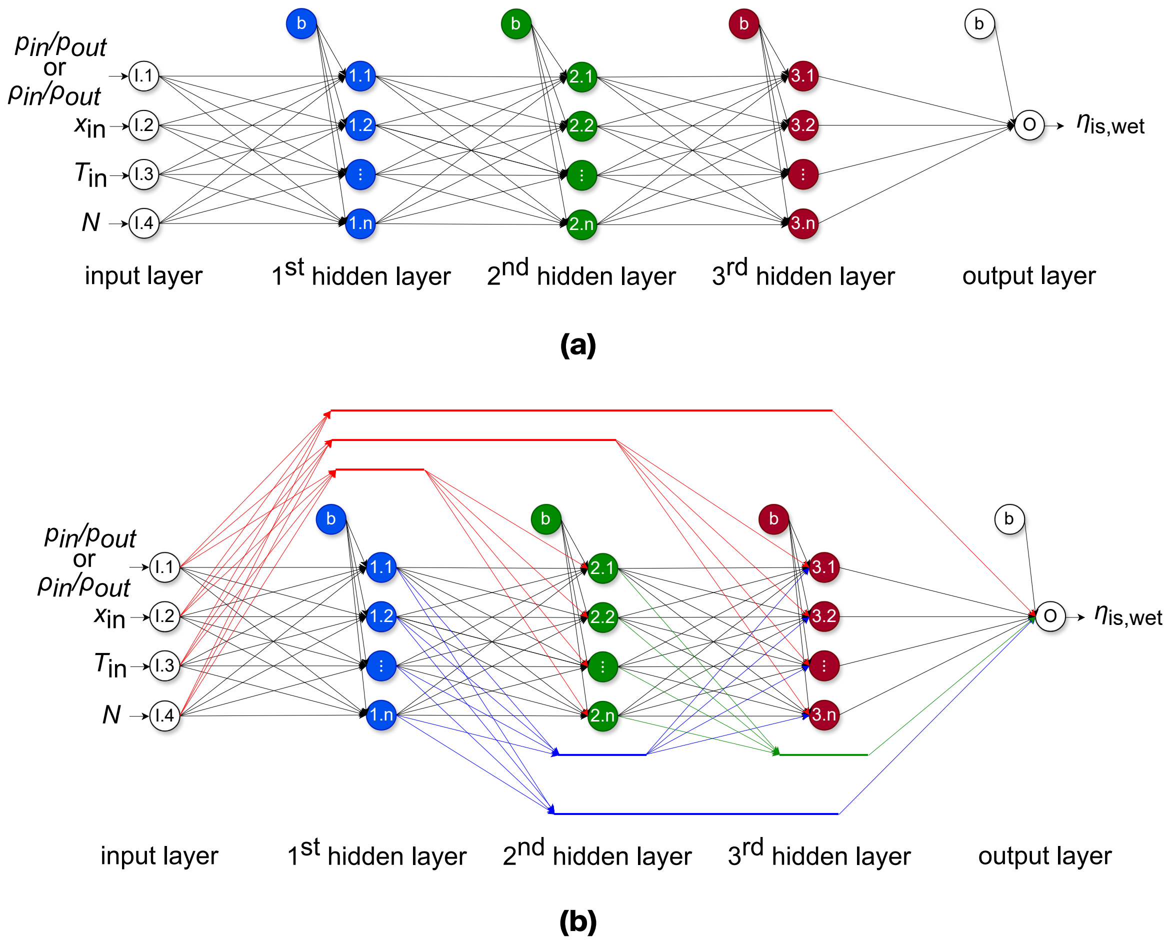

Fig. 4.3. Structure diagram of **(a)** FFDNN and **(b)** CFDNN with four input parameters (pressure ratio or density ratio, vapor quality, temperature at the inlet to the expander, and the rotational speed of the expander) and one output parameter (wet isentropic efficiency) [105].

mance.

$$R^2 = 1 - \frac{\sum_{i=1}^{n}(Y_i - \hat{Y}_i)^2}{\sum_{i=1}^{n}(Y_i - \bar{Y})^2} \tag{4.4}$$

$$RMSE = \sqrt{\frac{1}{n}\sum_{i=1}^{n}(Y_i - \hat{Y}_i)^2} \tag{4.5}$$

4.2. Discussion and main contributions

An initial experimental investigation [58] was conducted using a multi-vane expander to investigate its ability to handle the wet expansion process. The study showed that the expander operated effectively without significant issues. To further assess the wet isentropic efficiency of the two-phase multi-vane expander, measurement systems were installed, which has been described in the previous subchapter. This system enabled a detailed evaluation of how operating conditions affect the wet

Table 4.3. Boundary conditions of FFDNN and CFDNN [105].

Descriptions	Value
Experimental datasets	6,689
Percentage of experimental datasets for training	80%
Percentage of experimental datasets for validation	20%
Number of hidden layers	3
The transfer function of the first hidden layer	Linear
The transfer function of the second hidden layer	Log-sigmoid
The transfer function of the third hidden layer	Log-sigmoid
The number of neurons	3–20
Initial biases	0
Initial weights	0
Scalar mu	0
Algorithms	LM and BR
Performance index	MSE
Optimization criteria	RMSE in validation
Maximum epochs	1,000

isentropic efficiency of the expander, which is described in the following subchapter.

4.2.1. Experiment results

During the experiment, it was observed that the periodic drift heat source temperature ranged between 350.68 K and 361.93 K. As a result, the temperature of the low-boiling working fluid at the inlet to the expander showed fluctuations between 347.95 K and 358.15 K. In this study, both the heat source temperature and the temperature at the expander inlet showed periodic fluctuations every 7.5 to 8.0 minutes. During each cycle, the heat source temperature rose for approximately 4.3 to 4.9 minutes and then fell for about 2.9 to 3.1 minutes. Similarly, the temperature at the expander inlet increased for around 4.4 to 4.9 minutes and then decreased for about 2.9 to 3.2 minutes within each cycle.

During the experimental study, the vapor quality at the inlet to the expander was consistently maintained in the range between x_2=0.93 and x_2=0.98. Typically, the vapor quality at the outlet from the expander was observed between x_3=0.99 and x_3=1.00, although it occasionally decreased to x_3=0.98. It is worth noting that the expansion process generally began under two-phase conditions, but only a certain part of the expansion process proceeded in the two-phase region (not the entire process). During the experiment, the pressure ratio varied between $p_{\text{in}}/p_{\text{out}}$=5.67 and $p_{\text{in}}/p_{\text{out}}$=10.67, and the density ratio varied between $\rho_{\text{in}}/\rho_{\text{out}}$=7.4 and $\rho_{\text{in}}/\rho_{\text{out}}$=13.3.

In that case, it was observed that the wet isentropic efficiency of the expander varied from between $\eta_{wet,is}$=0.37 and $\eta_{wet,is}$=0.49. The relationship among the observed parameters (vapor quality, pressure ratio, and the wet isentropic efficiency) provides insights into the operational characteristic of the expander as depicted in Fig. 4.4. In this case, the measurement uncertainty for the pressure ratio is ca. ±1.41%, and the uncertainty for the wet isentropic efficiency is ca. ±0.045. The results illustrated in Fig. 4.4 indicate that analyzing the density ratio provides a clearer understanding of the variations in wet isentropic efficiency (along with the vapor quality) compared to using the pressure ratio. This is because the multi-vane expander, being a type of volumetric expander, operates based on changes in volume rather than pressure.

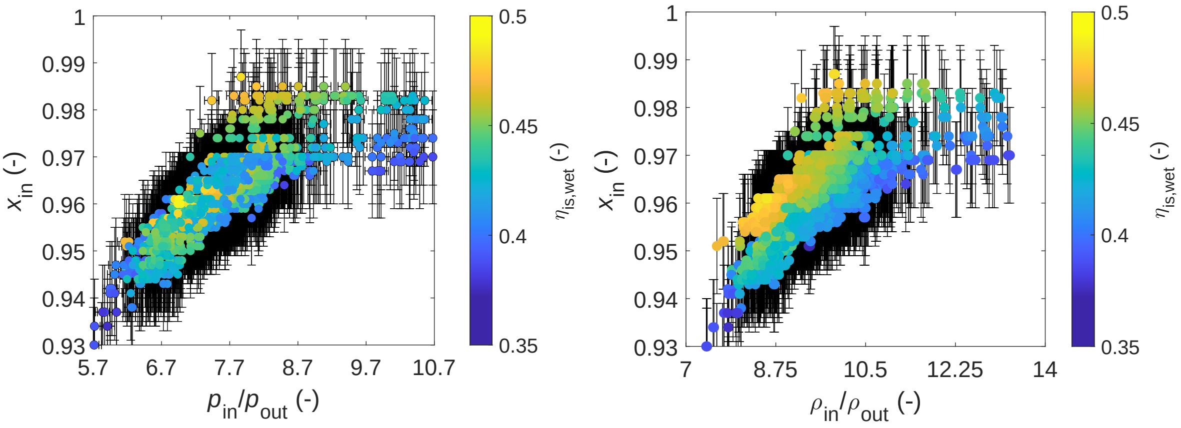

(a) **(b)**

Fig. 4.4. The experimental data and measurement errors in **(a)** the pressure ratio-based diagram, and **(b)** the density ratio-based diagram with vapor quality at the inlet to the expander, and the wet isentropic efficiency [105].

The experimental procedures required to analyze the performance map of a two-phase expander are inherently time-consuming. To streamline this process, configured DNNs have been applied to predict the wet isentropic efficiency of the two-phase multi-vane expander using a limited set of preliminary experimental data. This predictive approach serves two crucial purposes. Firstly, it helps to identify specific conditions that warrant further detailed investigation, which may lead to additional experiments. Secondly, it provides a means to preliminarily detect potential problems or limitations within the experimental setup. This early detection offers critical insights, allowing researchers to address issues before completing the entire scope of experimental work.

4.2.2. Predicted wet isentropic efficiency based on deep artificial networks

Since the pressure ratio is a commonly used parameter for expanders, this section will utilize a pressure ratio-based analysis. This approach is chosen to ensure that the explanation is easier to follow for readers and that predictions are more straightforward. By using a familiar parameter, the analysis will be more accessible, allowing for better comprehension and practical application of the results.

This investigation utilized a dataset comprising 6,689 experimental observations to develop a model aimed at predicting the wet isentropic efficiency of a two-phase multi-vane expander. The performance of the developed DNN models was assessed based on their ability to predict wet isentropic efficiency using several predefined input parameters. Each DNN model varied in complexity, with the hidden layers containing between three and twenty neurons. Through this approach, a total of 5,832 different combinations were tested across twelve configured DNN models for pressure ratio-based predictions and twelve configured DNN models for density ratio-based predictions. Each model was categorized according to one of three distinct sets of input parameters. This structured evaluation helped to determine the most effective neural network configurations for accurately predicting the performance of the expander.

The performance parameters of the optimal configured DNN models related to training and validation are detailed in Table 4.4. The results indicate that the four DNN configurations, which utilize the pressure ratio and vapor quality at the inlet to the expander, achieved an RMSE of training ranging from 0.0206 to 0.0210 and an R^2 value of training between 0.1700 and 0.2017. For validation, these models show an RMSE between 0.0196 and 0.0198 and an R^2 value from 0.2218 and 0.2351. These outcomes were obtained with the MSE of approximately 3.84 $\times$ 10^{-4}-3.91 $\times$ 10^{-4}. By incorporating additional input parameters, such as the temperature at the inlet to the expander and the rotational speed of the expander, the performance of the configured DNNs improves compared to models using just two inputs (pressure ratio and vapor quality at the inlet to the expander).

It is important to recognize that the discrepancy between the low RMSE and low R^2 values reveals a key insight: while the models are precise in their predictions (as indicated by the low RMSE), they do not explain much of the variability in the data (reflected by the low R^2). Additionally, the narrow range of RMSE values suggests that the DNN models have consistent prediction accuracy, likely converging to similar local minima during training. The low R^2 values underscore the need for a closer examination of the selected parameters and data quality to improve the model's overall performance.

By incorporating the temperature at the inlet to the expander, the RMSE during training can be reduced by up to 66.02%, and during validation, it can be lowered by up to 72.59% compared to DNN models using only two inputs. This addition also leads to a three to fourfold improvement in the R^2 value during both training and validation. Moreover, by adding both temperature and the rotational speed at the inlet to the expander, the RMSE during training can be further reduced by up to 67.96% and during validation by up to 72.08% when compared to using only the pressure ratio and vapor quality at the inlet to the expander. This enhancement also yields a similar three to fourfold increase in the R^2 value for both training and validation. All the improvements in RMSE and R^2 were achieved with the MSE, which is ca. 95% lower compared to the DNN models that only use the pressure ratio and vapor quality at the inlet to the expander as input parameters. The results indicate that incorporating additional input parameters significantly enhances the accuracy

Table 4.4. The RMSE, R^2, and MSE of the configured DNN models during training and validation [105].

Input parameters	**DNN model**	**Training function**	**Optimum RMSE (validation)** (-)	**RMSE (training)** (-)	R^2 **(validation)** (-)	R^2 **(training)** (-)	**MSE** (10^{-4}) (-)
p_{in}/p_{out} and x_{in}	FFDNN	LM	0.0197	0.0206	0.2232	0.1970	3.90
p_{in}/p_{out} and x_{in}	FFDNN	BR	0.0198	0.0207	0.2218	0.1925	3.91
p_{in}/p_{out} and x_{in}	CFDNN	LM	0.0196	0.0206	0.2351	0.2017	3.84
p_{in}/p_{out} and x_{in}	CFDNN	BR	0.0197	0.0210	0.2296	0.1700	3.87
p_{in}/p_{out}, x_{in}, and T_{in}	FFDNN	LM	0.0054	0.0070	0.9411	0.9066	0.30
p_{in}/p_{out}, x_{in}, and T_{in}	FFDNN	BR	0.0054	0.0072	0.942	0.9014	0.29
p_{in}/p_{out}, x_{in}, and T_{in}	CFDNN	LM	0.0055	0.0073	0.9397	0.8988	0.30
p_{in}/p_{out}, x_{in}, and T_{in}	CFDNN	BR	0.0054	0.0073	0.9425	0.8997	0.29
p_{in}/p_{out}, x_{in}, T_{in}, and N	FFDNN	LM	0.0055	0.0066	0.9389	0.9174	0.31
p_{in}/p_{out}, x_{in}, T_{in}, and N	FFDNN	BR	0.0055	0.0079	0.9404	0.8816	0.30
p_{in}/p_{out}, x_{in}, T_{in}, and N	CFDNN	LM	0.0055	0.0079	0.9389	0.8839	0.31
p_{in}/p_{out}, x_{in}, T_{in}, and N	CFDNN	BR	0.0057	0.0097	0.9358	0.8212	0.32

and the prediction.

Table 4.5. Comparison of the configured DNNs' performance [105].

Input parameters	DNN model	Training function	RMSE (total) (-)	R^2 (total) (-)	Epochs (-)	Number of neurons	Time (hours)
p_{in}/p_{out} and x_{in}	FFDNN	LM	0.0205	0.2093	10	[4,19,13]	0.84
p_{in}/p_{out} and x_{in}	FFDNN	BR	0.0205	0.2054	12	[4,19,16]	1.13
p_{in}/p_{out} and x_{in}	CFDNN	LM	0.0204	0.2152	15	[4,16,12]	1.19
p_{in}/p_{out} and x_{in}	CFDNN	BR	0.0207	0.1888	8	[4,17,7]	5.71
p_{in}/p_{out}, x_{in}, and T_{in}	FFDNN	LM	0.0067	0.9140	5	[4,10,16]	0.68
p_{in}/p_{out}, x_{in}, and T_{in}	FFDNN	BR	0.0069	0.9100	5	[4,13,7]	0.79
p_{in}/p_{out}, x_{in}, and T_{in}	CFDNN	LM	0.0070	0.9075	4	[4,18,15]	0.89
p_{in}/p_{out}, x_{in}, and T_{in}	CFDNN	BR	0.0070	0.9087	3	[4,3,20]	1.20
p_{in}/p_{out}, x_{in}, T_{in}, and N	FFDNN	LM	0.0064	0.9222	5	[4,10,19]	0.59
p_{in}/p_{out}, x_{in}, T_{in}, and N	FFDNN	BR	0.0075	0.9838	7	[4,5,9]	0.75
p_{in}/p_{out}, x_{in}, T_{in}, and N	CFDNN	LM	0.0074	0.8954	4	[4,14,6]	0.87
p_{in}/p_{out}, x_{in}, T_{in}, and N	CFDNN	BR	0.0091	0.8445	6	[4,18,4]	1.23

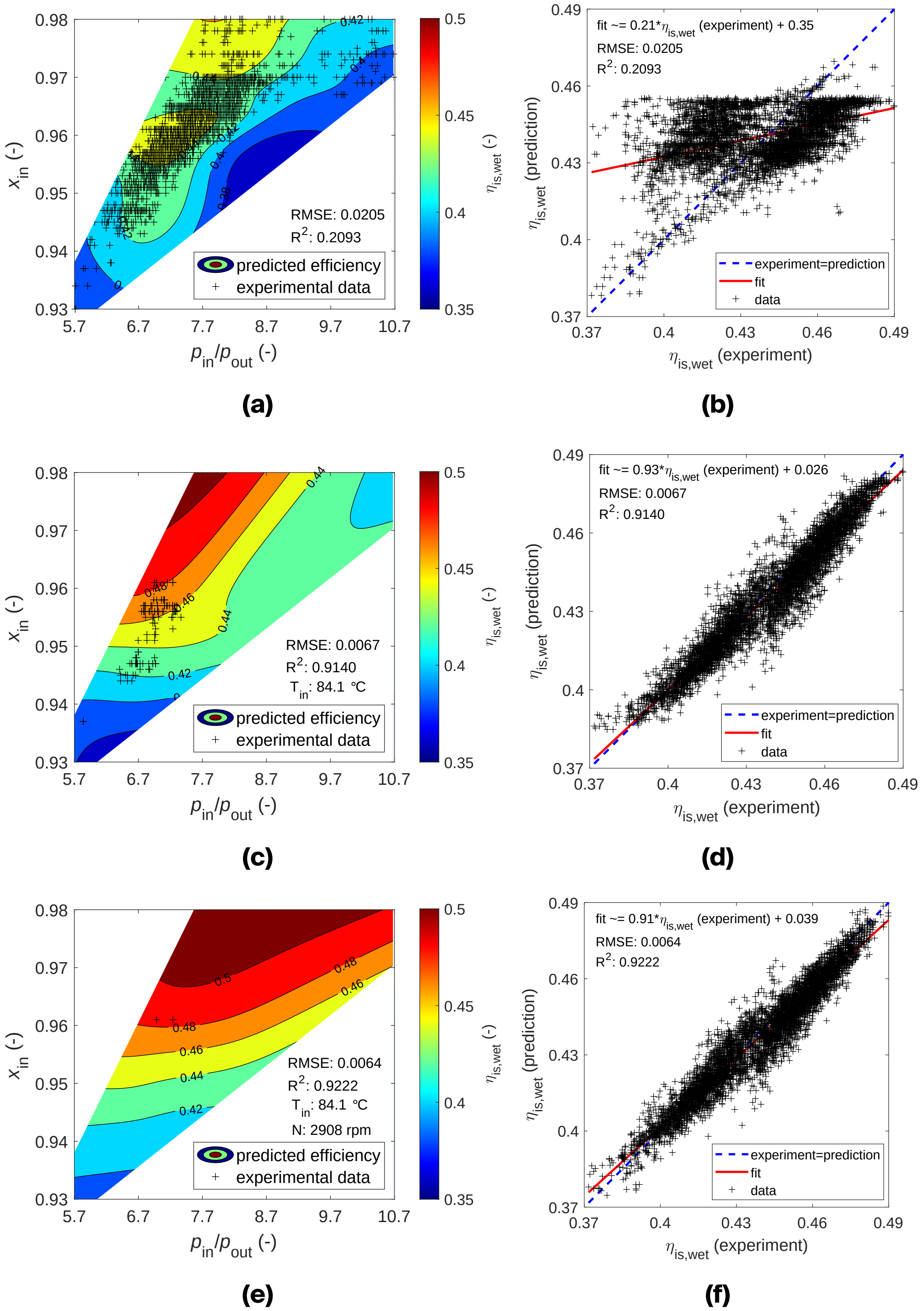

(a) **(b)**

(c) **(d)**

(e) **(f)**

Fig. 4.5. Pair of illustration as representative examples for performance map of predicted wet isentropic efficiency (right side) and the regression model (left side) of FFDNN using LM algorithm with **(a)** and **(b)** two input parameters, **(c)** and **(d)** three input parameters, and **(e)** and **(f)** four input parameters [105].

Furthermore, the performance parameters of the optimal configured DNN models in total are detailed in Table 4.5. According to Baumann's rule, the wet isentropic efficiency of a two-phase expander can be estimated using the dry isentropic efficiency and vapor quality [109]. Dry isentropic efficiency refers to the efficiency of an expansion process that consistently remains in a single phase, typically a superheated state. The results demonstrate the performance of four DNN configurations utilizing two input parameters - pressure ratio and vapor quality at the inlet to the expander that these models achieved an RSME (total) ranging from 0.0204 to 0.0207 and an R^2 value ranging from 0.1888 to 0.2152. When additional parameters such as temperature at the inlet to the expander and expander rotational speed are incorporated, there is a significant enhancement in the performance: RMSE can be reduced up to 68.78% and R^2 can increase up to four times compared to models that use only the initial two parameters. By incorporating rotational speed as an input, it is important to align the operating point with the optimal specific speed range indicated in the Balje diagram [20]. Operating within this optimal range ensures minimal mechanical and aerodynamic losses, resulting in higher efficiency for the expander. This alignment not only optimizes performance but also improves the accuracy of predicting wet isentropic efficiency.

Regarding model architecture, the optimal configuration used four neurons in the first hidden layer, followed by neurons in the second and third layers. It is worth noting that models incorporating three or four input parameters use fewer neurons than those using only two inputs. This reduction in neurons also leads to fewer required epochs for training ranging from 3 to 7, compared to more epochs needed for models with two inputs. This not only optimizes the model complexity but also significantly reduces computational time.

Furthermore, the choice of training algorithm affects computational speed. Models trained with the LM algorithm performed faster than those using the BR algorithm. Although the DNN model with three and four input parameters likely performs similar RMSE and R^2 in total, the computational times of the model with four inputs are 2.25-13.23% faster than those using three inputs.

The results indicate that the FFDNN utilizing the LM algorithm achieves superior performance over the FFDNN with BR and CFDNN with both LM and BR algorithms. This superiority is assessed based on low RMSE and high R^2 values. In that case, the FFDNN with the LM algorithm offers higher accuracy in predicting the wet isentropic efficiency compared to the other models tested. For visualization, the predicted wet isentropic efficiency using the FFDNN with the LM algorithm—incorporating inputs like pressure ratio, vapor quality, the temperature at the inlet to the expander, and expander rotational speed—is depicted in Fig. 4.5. This figure also includes the performance of the regression model. Additional details on these results and further performance metrics, which include FFDNN with BR and CFDNN with both LM and BR, are discussed elsewhere in this article [105].

Fig. 4.5 presents the performance maps of predicted wet isentropic efficiency and the regression using FFDNN models. In Figs. 4.5(a) and (b), which use only two input parameters (pressure ratio and vapor quality at the inlet to the expander), the performance maps and regression analysis show a low RMSE and R^2. Here, the fitting line (shown in red) diverges significantly from the experimental and predicted line (dashed blue), which is described by Eq. 4.6 [105]. The data distribution also indicates low accuracy, reflecting an undesirable trend that does not align well with the experimental data.

$$\eta_{\text{is, wet}}(\text{prediction}) = 0.21\eta_{\text{is, wet}}(\text{experiment}) + 0.35 \tag{4.6}$$

However, enhancements are evident when the temperature at the inlet to the expander is introduced as the third input parameter, depicted in In Figs. 4.5(c) and (d). The fitting line here closely matches the experimental and prediction line, described by Eq. 4.7 [105]. This close correlation is also supported by the data distribution, validating the accuracy of the model as it is close to the experimental data. Nonetheless, this analysis represents only a limited set of experimental data in Fig. 4.5(c), specifically at the temperature of 357.25 K, illustrating the validation of the model. There are a total of 103 possible combinations).

$$\eta_{\text{is, wet}}(\text{prediction}) = 0.93\eta_{\text{is, wet}}(\text{experiment}) + 0.026 \tag{4.7}$$

Further improvements are observed with the addition of the rotational speed of the expander as the fourth input parameter, as shown in Figs. 4.5(e) and (f). The fitting line here is nearly identical to that of the experimental and prediction line, which is described by Eq. 4.8 [105]. The distribution aligns closely with the fitting line, indicating a good match with the experimental data. Similar to the prior condition with three input parameters, this analysis is based on a few experimental data points, specifically at the temperature of 357.25 K and a rotational speed of 2,908 rpm, used for validating the predictions and providing illustrative examples out of a total 10,609 possible combinations.

$$\eta_{\text{is, wet}}(\text{prediction}) = 0.91\eta_{\text{is, wet}}(\text{experiment}) + 0.039 \tag{4.8}$$

Furthermore, it is important to note that compared to using the pressure ratio-based prediction, using the density ratio-based approach demonstrates better predictive performance, as evidenced by lower RMSE values (0.0136-0.0148) and higher R^2 values (0.5832-0.6474). When the temperature of the working fluid at the expander's inlet is included, the density ratio-based DNN model further improves, achieving reduced RMSE values (0.0033-0.0034) and enhanced R^2 values (0.9780-0.9793). Moreover, incorporating the rotational speed of the expander as a fourth input parameter was examined, resulting in further performance enhancements. With the density ratio-based prediction, RMSE values range from 0.0034 to 0.0036 and R^2 values from 0.9748 to 0.9780. Using four input parameters yields nearly identical RMSE and R^2 values compared to using three input parameters while significantly reducing computing time by up to 49.70%. Further information related to density ratio-based prediction in detail can be found in this article [105].

4.3. Conclusions

This chapter presents an experimental study on a two-phase expansion system in an ORC test setup, equipped with a multi-vane expander. It outlines the boundary conditions and limitations specific to this study. The chapter also discusses the use of DNN to predict the wet isentropic efficiency, employing twenty-four different DNN configurations. The performance comparison of the DNN models has been described. The research provides foundational insight into how factors such as pressure ratio, density ratio, vapor quality, temperature at the inlet to the expander, and rotational speed influence the wet isentropic efficiency.

This chapter describes the experimental study and examines the prediction of isentropic efficiency under different operational conditions in a two-phase expansion system, which was assessed by DNN. In dry conditions (superheated state), the isentropic efficiency, referred to as dry isentropic efficiency, can be estimated based on the pressure ratio. According to Baumann's rule, the wet isentropic efficiency of a two-phase expander can be predicted with the dry isentropic efficiency and vapor quality. The main contribution from this chapter is described in Thesis 5 and Thesis 6. In this chapter, Thesis 6 demonstrates that while adding more inputs can stabilize prediction accuracy, strategic choice of parameters can optimize both accuracy and computational performance.

Thesis 5. *A low-boiling working fluid expansion process in an organic Rankine cycle system can be done under two-phase conditions with a multi-vane expander using 2,2-Dichloro-1,1,1-trifluoroethane (R123) as the working fluid. Under the vapor quality at the inlet to the expander* x_2*=0.93-0.98, pressure ratio* p_{in}/p_{out}*=5.67-10.67, density ratio* ρ_{in}/ρ_{out}*=7.4-13.3, and the temperature at the inlet to the expander* T_2*=347.95-358.15 K, the wet isentropic efficiency of the multi-vane expander* $\eta_{wet,is}$*=0.37-0.49 can be obtained with the measurement uncertainty ca.* $\pm$ *0.045.*

The publications by the author that are related to Thesis 5 are [58, 105].

Thesis 6. *Predicting wet isentropic efficiency can be done using deep learning or deep neural networks (DNNs), which are methods within the field of artificial intelligence. Low accuracy of prediction was observed when using only the pressure ratio and vapor quality at the expander inlet as input variables of DNN for determining the wet isentropic efficiency of low-boiling working fluid expansion processes. However, adding the temperature of working fluid to the expander inlet as an additional input parameter of the DNN significantly enhances the accuracy of the model, reducing the root mean squared error (RMSE) by up to 68% and increasing the coefficient of determination* R^2 *by up to four times compared to the initial DNN model (using pressure ratio and vapor quality at the inlet to the expander). It is worth noting that using density ratio-based prediction offers higher accuracy in predicting the wet isentropic efficiency of the expander compared to using pressure ratio-based prediction. Furthermore, introducing the expander rotational speed as a fourth input parameter of DNN maintains similar RMSE and* R^2 *values as the three-parameter model but improves computational efficiency, speeding up the prediction time by 2.25% to 49.70%.*

The publications by the author that are related to Thesis 6 are [105].

5

Adaptability analysis of volumetric expanders in selected different ORC systems utilizing low and medium temperature heat sources

An essential part of transitioning to sustainable energy, with the goals of meeting climate targets and lessening our dependence on fossil fuels, includes not only the increased exploitation of solar photovoltaic (PV) and wind power but also the effective utilization of low- and medium-temperature heat sources. The availability of these heat sources can vary, with some being predictable and others unpredictable. It is worth noting that some geothermal sources can provide a more consistent and permanent supply. Therefore, committed efforts are required to efficiently manage these heat sources. This approach is vital for developing an energy system that is both sustainable and robust.

ORC systems are effectively used to harness low-and-medium temperature heat sources. Several ORC designs have been developed, including regenerative, multistage, cascaded, and reheating cycles. However, choosing an appropriate working fluid is crucial for ORC systems because the type of fluid, along with its thermal properties, environmental impact, and safety considerations, significantly influences the design and operation of the cycle. This selection becomes particularly important as the performance of the ORC system can vary greatly with changes in the heat source.

A recent review article [110] highlighted advances in developing low-temperature ORC systems that utilize heat sources below 423.15 K. Moreover, another article[111] offered insights into the exergy assessment of ORC systems for waste heat recovery. Despite these advancements, literature reviews indicate a persistent gap in applying ORC technologies effectively at low temperatures. Chapter 5 aims to prove that the two-phase expansion system in an ORC configuration demonstrates increased adaptability to fluctuations in heat source temperatures, maintaining optimal efficiency across a wider range of operational conditions compared to single-phase systems. In that case, this chapter also focuses on exploring potential designs and the integration of heat sources that fall within low to medium-temperature ranges. Specifically, it will examine several volumetric expanders, including the incorporation of two-phase expanders within the ORC systems, aiming to optimize the use of such temperature ranges efficiently. Some thematic applications of using ORC with a two-phase expansion system to harness low-temperature waste heat are discussed. To deepen understanding, a further investigation was undertaken by incorporating the wet isentropic efficiency of the volumetric expander which is predicted using AI FFDNN with LM described in Chapter 4.

5.1. Brief description of fluctuating and intermittent heat sources

Fluctuating and intermittent heat sources can be analyzed and categorized based on characteristics such as variables and frequency. When referring to variables, this involves fluctuations in certain parameters within a heat source, which, in the context of thermodynamic power cycles (e.g., several ORC systems), typically involves changes in mass flow rate (in some cases, it can be $\dot{m}$=0), temperature, or both simultaneously. Understanding and managing these variables is crucial for maintaining stable and efficient system operation. In addition, it helps in predicting and controlling the behavior of the system under varying operating conditions. On the other hand, fluctuations based on frequency relate to the regularity and timing of changes occurring in the heat source over time. These variations can manifest over different timescales—ranging from days and hours to minutes and seconds, depending on the heat source. Analyzing these frequency patterns is vital for resource planning, system optimization, performance assessment, and decision-making to ensure that thermodynamic cycles perform efficiently.

Table 5.1 presents a list of various fluctuating and intermittent heat sources, including those derived from waste heat, renewable energy, and other categories. This list offers a brief overview of the different types and origins of heat sources that can be utilized for energy production. Given the significant variations in their availability and intensity, these sources require advanced management and optimization strategies to effectively convert them into usable energy. Table 5.1 serves as a valuable resource for identifying potential opportunities for energy recovery and enhancing sustainability across a range of industries and applications. Some fluctuating and intermittent heat sources may experience changes in mass flow rate and temperature, including periods when the unpredictable mass flow rate drops to zero. Moreover, water and air are valuable not only as cooling sources in energy systems but also as heat sources for power generation, especially in regasification systems that utilize cold energy. While air and water are abundant, their availability as thermal resources can be intermittent and vary widely based on climate and geographic location. Such variability needs to be accounted for when incorporating these resources into power plant operations to effectively optimize their thermal properties for energy production.

Table 5.1. An overview of fluctuating and intermittent heat sources, adapted from [13, 112].

Application	**Heat sources**	**Category**	**Variables**	T (K)	$\dot{m}$ (kg/s)	**Freq.**	**Refs**
Diesel engine	Exhaust	Waste heat	T & $\dot{m}$	393.15-773.15	0-0.4	Seconds	[112]
Gasoline engine	Exhaust	Waste heat	T & $\dot{m}$	393.15-973.15	0-0.1	Seconds	[112]
Cement clinker cooler	Exhaust air	Waste heat	T	423.15-623.15	$\sim$53.75	Minutes	[112]
Steel billet reheating	Off gas	Waste heat	$\dot{m}$	1073.15-1223.15	1.5-8	Minutes	[112]
Steel electric arc furnace	Off gas	Waste heat	T & $\dot{m}$	373.15-1023.15	5-32	Minutes	[112]
Solar thermal	Thermal oil	Renewable	T & $\dot{m}$	503.15-553.15	0-12	Hours-Days	[112]
Ocean thermal	Warm surface water or deep cooling water	Renewable	T & $\dot{m}$	ΔT= 5-15*	8.3-2020	Hours-Days	[113, 114, 115]
Geothermal	Geothermal fluid	Renewable	T & $\dot{m}$	353.15-623.15	0.001-229	Hours, Days, Months, Years	[116, 117, 118]
Several applications	Air	Environment	T & $\dot{m}$	ΔT=40*	>0.01	Hours, Days, Months, Years	[119, 120]
Several applications	Water	Environment	T & $\dot{m}$	ΔT=20*	>0.01	Days, Months, Years	[119, 121]

5.2. General description of the thermodynamic system

It is important to note that the developed numerical models used in this chapter are identical to those employed in Chapters 2 and 3. Moreover, the isentropic efficiency was predicted using the DNN model which has been validated using experimental data described in Chapter 4. This consistency ensures that the comparative analysis across different scenarios and conditions remains valid and reliable. Additional scenarios are explored and described in detail in the following subsubsections.

5.2.1. ORC with a two-phase expansion system and its possible integration

Recent developments in ORC systems have introduced several alternative designs aimed at efficiently harnessing intermittent and fluctuating heat sources. These designs are depicted in Fig. 5.1, which includes their operation on the $T-s$ (temperature-entropy) diagram, the layout of the designed system, and the common names of these systems.

One of such innovation is the PE-ORC system, which uses a two-phase expansion system. In this setup, the working fluid is heated to a certain temperature, achieving a vapor quality between 0 and 1 (the process $1 \rightarrow 3$ on the $T-s$ diagram). The fluid then undergoes an expansion process $3 \rightarrow 4$ while in a two-phase condition (i.e., the mixture of liquid and vapor). After expansion, the working fluid must be condensed back into a liquid phase, a process $4 \rightarrow 5$ in a condenser. Finally, the fluid is pressurized in the process $5 \rightarrow 1$ to complete the closed-loop cycle. Moreover, the methods for calculating the thermodynamic performance of the system, including changes in enthalpy, cycle efficiency, and output power, are detailed in Chapters 2 and 3. This includes step-by-step explanations of how these key performance indicators are derived, ensuring a comprehensive understanding of the system's operational efficiency. In addition, it is worth noting that using a dry or specific isentropic working fluid may enhance the cycle efficiency of the PE-ORC system, potentially outperforming traditional ORC systems. This concept has been discussed in prior chapters. Therefore, for illustrative purposes, Fig. 5.1 shows PE-ORC operating using dry working fluids in the $T-s$ diagram.

The challenge of working with heat sources that fluctuate in intensity or are intermittently available can also be tackled in ORC systems through two different approaches of using thermal energy storage (TES) [14], as follows:

- Direct TES system is a design where the thermal storage is integrated directly into the ORC and may be combined with various components such as evaporators, liquid heaters, and condensers. Several studies have explored potential configurations like TES-liquid heater, TES-evaporator, and TES-condenser setups. Nevertheless, there have been relatively few experimental studies conducted to validate these configurations.
- An indirect TES system is a design where the thermal storage is installed as a separate component within the ORC system. This approach is commonly

used in various solar thermal power plants. In these plants, the configuration typically involves two types of TES: hot and cold. The hot TES stores heat accumulated after thermal oil is heated by solar collectors, while the cold TES accumulates thermal oil after it has transferred its heat to the working fluid in the heat exchanger. In addition, there is potential for storing cooling energy from different sources, such as LNG, hydrogen, DME, or other cryogenic substances.

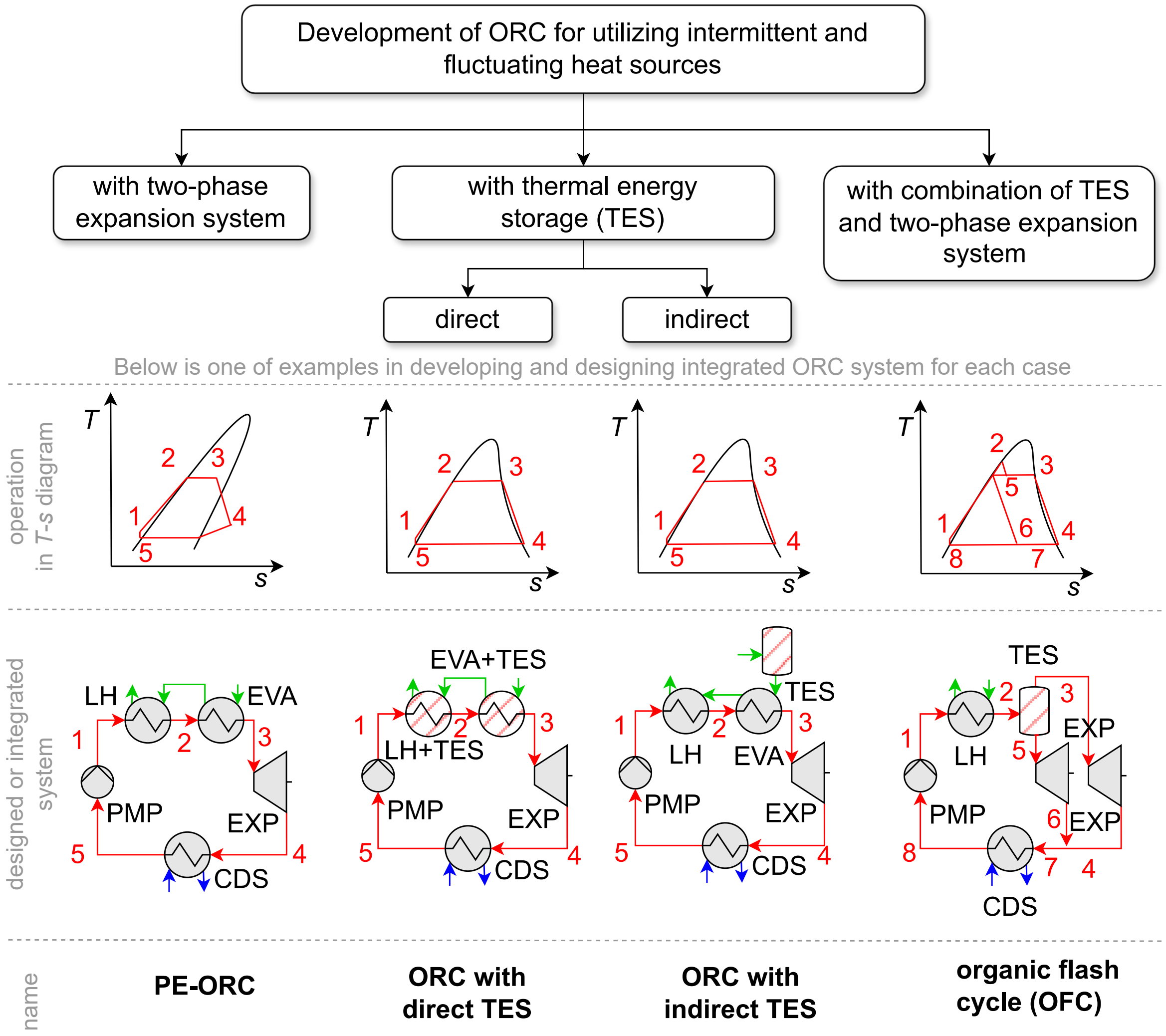

Fig. 5.1. Development of ORC using two-phase expansion to harness intermittent and fluctuating low-to-medium temperature heat sources which can be achieved directly, through thermal energy storage both directly and indirectly, or through a combined system, adapted from [13]. The components labeled in the illustration are LH (liquid heater), EVA (evaporator), EXP (expander), CDS (condenser), PMP (pump), and TES (thermal energy storage).

Several configurations of ORC with direct and indirect TES systems have been reviewed and discussed [14]. In addition, the review explored potential phase change materials (PCMs) that could be used for TES. Among the various types of PCMs reviewed, liquid-solid PCMs appear to be particularly well-suited for use in ORC applications. These materials facilitate efficient energy storage and release in terms of volume, making them advantageous for this type of system [17].

Furthermore, it is possible to integrate both two-phase expander and TES within the same ORC system. Typically, ORCs are designed to operate in a dry or superheated condition during the expansion process. To accommodate this, a separator can be installed before the expander to separate the working fluid into liquid and vapor phases. This setup is known as an organic flash cycle (OFC) [122], which one of the designs is depicted in Fig. 5.1. In this design, the vapor phase of the working fluid enters the expander, while the liquid phase is directed into a throttle valve. A study [101] suggested the possibility of replacing the throttle valve with a two-phase expander, which could generate more output power and improve the overall cycle efficiency of the system.

5.2.2. Carnot battery via a reversible ORC/heat pump

A more sophisticated system than ORC might be required to effectively harness intermittent and fluctuating heat sources. Recent literature reviews [123, 124] have highlighted Carnot battery technology, which incorporates a combination of heat engine, heat pump, waste heat recovery, the use of renewable energy, and TES. The Carnot battery works by converting electrical energy into thermal energy for storage, and later, this stored thermal energy is converted back into electrical energy. This approach could be a crucial step forward in decarbonizing the current energy infrastructure due to its capability to store energy, offering a flexible and efficient method for managing energy storage and conversion.

In the Carnot battery, the charging process involves converting electrical power to heat (i.e., the power-to-heat step) by a resistive heating system. Following this, the heat is stored with minimal losses in TES before converting back into electricity through a power cycle during the discharge phase. In order to enhance the efficiency of power-to-power in the Carnot battery, integrating heat pumps into the charging process could be one of the possibilities. However, it requires high temperature and high power heat pumps.

Carnot batteries can be classified based on the thermodynamic cycles they employ, such as Brayton, Rankine, and hybrid cycles. A study [125] indicates a notable distinction between Brayton-based systems and those based on the ORC, particularly in terms of energy consumption by the pump or compressor. Specifically, Brayton-based cycles require significantly more power to increase the pressure of the working fluid compared to ORC systems. In the context of using an ORC-based Carnot battery system, it can be developed as a standalone device where the heat pump (used for ”charging” the battery) and the heat engine (used for ”discharging” the battery) are functionally separate. This setup needs to incorporate all sub-components of both the heat pump and the heat engine, which leads to greater upfront investment expenses. Some efforts are being made to lower the costs associated with implementing such systems to address these financial challenges. In this case, it includes adopting simpler designs that reduce complexity and decrease the number of necessary components, ultimately leading to cost reductions. In this context, employing a Carnot battery via a reversible ORC/heat pump could be a viable solution. There are two potential designs for a reversible

Rankine cycle: one where a single device functions both as a compressor and an expander [126] and another where the compressor and expander are separate machines [127]. During the heat pump mode in both systems, a throttle valve serves as an expansion device. This expansion process can be advantageous for generating electricity. Therefore, this study explores the use of a Carnot battery with a reversible ORC/heat pump that utilizes a shared expander (which, for example, can be a multi-vane machine similar to the expander tested experimentally and comprehensively described in Chapter 4).

A block diagram of a novel reversible ORC/heat pump used in Carnot battery technology, along with the schematic diagram and operational details, is illustrated in Fig. 5.2. This system comprises two heat exchangers, a compressor, a liquid pump, and an expander connected to a generator/motor. Depending on whether it operates in heat pump or heat engine mode, the two heat exchangers can function either as evaporators or condensers. The carrier fluids for heating or cooling HE2 may be the same or different; in this study, air or water is used as the cooling carrier, while waste heat serves as the heating carrier.

HE1 functions as a condenser and HE2 as an evaporator in the heat pump mode. This process heats a secondary fluid to a specific temperature and stores the heat in a TES system. The operation of this system requires electricity, which could potentially be sourced from renewable energy like photovoltaic or wind turbines, to power the compressor and increase the pressure of the working fluid. Moreover, it can harness waste heat generated from various industrial processes. This heat pump operation corresponds to the system's charging mode. In addition, control valves are placed to assist the transition between reversible system modes and to control the flow of the process. The energy balance of each component in heat pump mode is calculated using enthalpy changes and described in Table 5.2. In this table, the subscripts of 'sf', 'wf', and 'wh' refer to secondary fluid, working fluid, and waste heat carrier fluid, respectively.

HE1 and HE2 are configured as counter-flow heat exchangers in the Carnot battery system architecture in order to achieve optimum efficiency. During the heat pump mode, the waste heat carrier fluid flows through HE2, causing the working fluid within the cycle to vaporize. Once the working fluid reaches a certain state (in this case, saturated vapor or vapor quality of x=1), a compressor is used to compress it in order to get the required thermodynamic characteristics. The compressor is powered by a motor, which in turn is driven by renewable energy sources such as photovoltaic or wind turbines. In this configuration, the motor can also serve as a generator—a device referred to as a motor-generator. The installation of a reversible motor-generator necessitates careful consideration of several factors, including shaft control and the physical configuration, especially since the compressor is inactive during the ORC mode. This arrangement may affect the efficiency of the reversible motor-generator, a subject that has led to several patented innovations [129, 130]. Furthermore, the compression process of the working fluid is illustrated by process $2 \rightarrow 3$ in Fig. 5.2(b). The heat pump then uses a secondary fluid to absorb heat, which causes the heat flow from the TES to increase. After the working fluid inside the cycle attains a saturated liquid state (or vapor quality of x=0), it is expanded using an expander and can be utilized in subsequent pro-

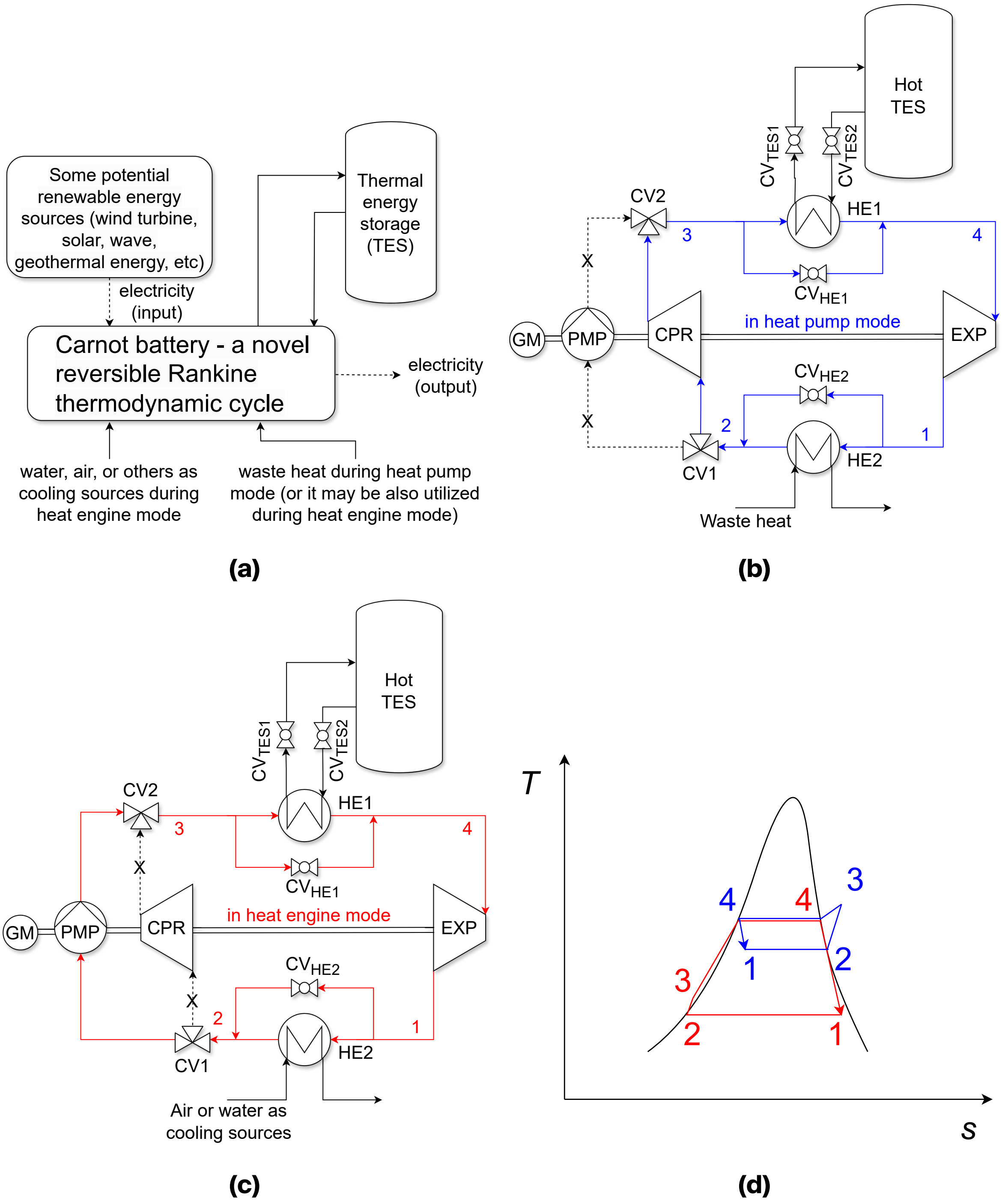

(a)

(b)

(c)

(d)

Fig. 5.2. Carnot battery via reversible ORC/heat pump in (a) block diagram, (b) schematic diagram of heat pump operation, (c) schematic diagram of ORC operation, and (d) its operation in $T - s$ diagram in both modes, adapted from [128]. The components labeled in the illustration are HE (heat exchanger), CV (control valve), EXP (expander), PMP (pump), CPR (compressor), and GM (generator/motor). The blue and red lines represent the operation of the heat pump and ORC mode, respectively.

cesses within a closed-loop system. Furthermore, the coefficient of performance (COP) of the Carnot battery in heat pump mode can be determined.

Table 5.2. Energy balance of the components during the heat pump mode referring to the operation in Fig. 5.2(b) and (d).

Components	**Energy balance**
HE1	$\dot{Q}_{\text{HE1}} = \dot{m}_{\text{wf}}(h_3 - h_4) = \dot{m}_{\text{sf}}\Delta h_{\text{sf}}$
HE2	$\dot{Q}_{\text{HE2}} = \dot{m}_{\text{wf}}(h_2 - h_1) = \dot{m}_{\text{wh}}\Delta h_{\text{wh}}$
Compressor (CPR)	$\dot{W}_{\text{CPR}} = \dot{m}_{\text{wf}}(h_{3,\text{is}} - h_2)/\eta_{\text{CPR,is}}$ $\eta_{\text{CPR,is}} = (h_{3,\text{is}} - h_2)/(h_3 - h_2)$
Expander (EXP)	$\dot{W}_{\text{EXP,heat pump}} = \dot{m}_{\text{wf}}(h_4 - h_{1,\text{is}})\eta_{\text{EXP,is,heat pump}}$ $\eta_{\text{EXP,is,heat pump}} = (h_4 - h_1)/(h_4 - h_{1,\text{is}})$
Coefficient of performance (COP)	$COP = \dot{m}_{wf}(h_3 - h_4)/(\dot{W}_{\text{CPR}} - \dot{W}_{\text{EXP,heat pump}})$

In the heat engine (power cycle) mode of the system, which employs air or water as cooling sources, the stored heat in TES may be used to produce electricity. In this mode, HE1 functions as the evaporator and HE2 as the condenser. This heat engine works using an ORC operating mode, where a pump is employed to increase the pressure of the working fluid, replacing the compressor used in the heat pump mode. The operations of the Carnot battery system are visually represented on $T-s$ diagram (see Fig. 5.2(c) and (d)), where the heat pump mode is depicted with blue lines and the heat engine mode with red lines. During the ORC mode, HE1 functions to evaporate the working fluid until it reaches saturated vapor state (or vapor quality of x=1), after which it moves into the expander. The process 3 $\rightarrow$ 4, as shown in Fig. 5.2(c), involves heating the liquid and evaporating it using an energy balance. The next stage is the expansion process, where the working fluid drives the expander according to a predetermined pressure and volumetric expansion ratio. Changes in enthalpy and isentropic efficiency can characterize this expansion process. In the following process, using the heat exchanger of HE2, the working fluid is then condensed using cooling sources (typically water or air) until it achieves a saturated liquid phase (vapor quality of x=0). Following this, the working fluid is prepared for pumping and recirculation within the system. The heat transfer process between the working fluid and the cooling sources in HE2 involves enthalpy changes. In the end, the overall cycle efficiency of ORC mode in the designed Carnot battery can be calculated. The energy balance of the components and the cycle efficiency of the ORC operating mode are described in Table 5.3. In this table, the subscript of 'cs' refers to cooling source carrier fluid.

Furthermore, the performance of the designed Carnot battery could be assessed using an overall power-to-power (P2P) efficiency, which is defined by Eq. 5.1. This calculation assumes that the efficiency of the thermal storage is ideal, meaning it is considered to be 1, indicating no thermal losses within the system [131, 128]. It is important to note that part of the description related to TES is described in detail in this article [128].

Table 5.3. Energy balance of the components during the ORC mode referring to the operation in Fig. 5.2(c) and (d).

Components	**Energy balance**
HE1	$\dot{Q}_{\text{HE1}} = \dot{m}_{wf}(h_4 - h_3) = \dot{m}_{\text{sf}}\Delta h_{\text{sf}}$
HE2	$\dot{Q}_{\text{HE2}} = \dot{m}_{\text{wf}}(h_1 - h_2) = \dot{m}_{\text{cs}}\Delta h_{\text{cs}}$
Pump (PMP)	$\dot{W}_{\text{PMP}} = \dot{m}_{\text{wf}}(h_{3,\text{is}} - h_2)/\eta_{\text{PMP,is}}$ $\eta_{\text{PMP,is}} = (h_{3,\text{is}} - h_2)/(h_3 - h_2)$
Expander (EXP)	$\dot{W}_{\text{EXP,ORC}} = \dot{m}_{\text{wf}}(h_4 - h_{1,\text{is}})\eta_{\text{EXP,is,ORC}}$ $\eta_{\text{EXP,is,ORC}} = (h_4 - h_1)/(h_4 - h_{1,\text{is}})$
Cycle efficiency of ORC	$\eta_{\text{ORC}} = (\dot{W}_{\text{EXP,ORC}} - \dot{W}_{\text{PMP}})/\dot{m}_{wf}(h_4 - h_3)$

$$P2P = COP_{\text{heat pump}} \cdot \eta_{\text{ORC}} \cdot \eta_{\text{TES}} = COP_{\text{heat pump}} \cdot \eta_{\text{ORC}} \tag{5.1}$$

In this study, the designed Carnot battery described above was calculated and simulated in MATLAB using the thermal properties of working fluid obtained from REFPROP 10.0 [88] and CoolProp [87]. Nine working fluids were selected based on the safety concern, the environmental effect (zero ODP and low GWP), and the operating temperature range between 273.15 and 383.15 K. These nine working fluids are dimethyl ether (RE170), butane (R600), butene, isobutane (R600a), isobutene, 1,1-difluoroethane (R152a), trans-1,3,3,3-tetrafluoropropene (R1234ze(E)), cis-1,3,3,3-tetrafluoropropene (R1234ze(Z)), and trifluoroiodomethane (R13I1). A study [132] has reported that R13I1 has no impact on stratospheric ozone depletion. This assessment focuses specifically on its effects on stratospheric ozone. In this study, the simulation temperature step was set at 1 K, and some boundary conditions are summarized in Table 5.4.

5.3. Discussion and main contributions

5.3.1. Discussion on the volumetric expander and its possible integration in ORC system for low and medium temperature heat sources

5.3.1.1. A case study of an integrated system of low-temperature geothermal heat sources and cold energy utilization

An ORC system utilizing a two-phase expansion system, referred to as PE-ORC, is particularly effective for harnessing low and medium-temperature heat sources. The PE-ORC system is characterized by its partial evaporation process, unlike a basic ORC that employs a full evaporation process. In the PE-ORC, the rate of heat exchange between the heat sources and the heat exchanger (which includes a liquid heater and a partial evaporator) might be lower than in a basic ORC, which uses

Table 5.4. Summary of boundary conditions in the designed Carnot battery [128].

Parameters	**Heat pump**	**ORC**
Pinch point temperature of HE1 and HE2 (K)	5	5
Temperature of the secondary fluid in HE1 (K)	348.15-358.15	348.15-358.15
Temperature of heat/cooling carrier fluid in HE2 (K)	328.15-343.15 (waste heat carrier fluid)	288.15-303.15 (cooling carrier fluid)
Isentropic efficiency of the expander (-)	<0.8	0.8
Isentropic efficiency of the pressure riser (-)	0.8 (compressor)	0.8 (pump)

a full evaporator and potentially a superheater. Given this configuration, assuming that the heat transfer rate from the heat source remains constant, the mass flow rate of the working fluid in the PE-ORC will likely be higher compared to that in a basic ORC. This adjustment in mass flow rate helps to compensate for the lower heat exchange rate in the PE-ORC, facilitating effective energy balance within the system. A study [103] reported that PE-ORC surpasses the ORC in exergy efficiency by as much as 80%. This significant increase in efficiency also suggests that the PE-ORC utilizes heat sources more effectively. Another study [133] reported that the output power of ORC by operating with a two-phase expansion system could be improved by up to 30%.

Part of the study in this chapter has been discussed in [15, 94]. It may be possible to extract the geothermal heat for power generation, which can be effectively transported over long distances using electrical grids. This transportation method is feasible even across islands, potentially through subsea grids. However, various challenges, such as the topography of the seabed, seismic activity, distance, installation complexities, maintenance requirements, and economic factors, can pose limitations at the installation site. Also, economic challenges may arise when constructing grids to distribute electricity among multiple small islands, such as those in geothermally active areas like Indonesia. As an alternative for future consideration, the use of energy storage methods, such as a cold battery that stores energy in liquid form at temperatures below 273.15 K, may provide a viable solution. In addition, many low-temperature geothermal sources remain untapped due to their limited economic viability. To address these challenges, the implementation of an integrated system could offer a viable solution for harnessing geothermal energy, which is depicted in Fig. 5.3.

In this context, dimethyl ether (DME or RE170) has been proposed as a cooling agent. DME can be produced from various sources, including coal, oil, natural gas, and biomass, through direct or indirect synthesis processes. From wood waste, the process involves several steps, including pyrolysis and gasification. Moroever, there is an opportunity to recover the waste heat generated during these processes to produce electricity, as illustrated in Fig. 5.3. Utilizing waste for DME production not only presents a strategic approach to waste management but also contributes to environmental benefits. For instance, organic waste such as biomass, household, and industrial waste can be processed into DME near geothermal plants (e.g., within 150 km). Besides DME, this process can also generate by-products like fertilizer, adding further environmental advantages to the use of DME in geothermal energy systems.

DME can be used as a working fluid within ORC that includes a two-phase expansion system [15]. The results demonstrate that the cycle efficiency can reach as high as 0.115 when the condenser temperature is set at 303.15 K, and the evaporator temperature goes up to 390.15 K. By reducing the condenser temperature further to 273.15 K, which allows the regasification of liquid DME to serve as a cooling source, the cycle efficiency can be increased from 0.115 to 0.142. Moreover, using DME as a cooling fluid in the cycle (in this case, DME is used in a separate system, serving two functions: as the working fluid for the ORC and as a cooling carrier fluid) leads to an increase in output power. A case study demonstrates the impact of temperature settings on output power in an ORC system. In the case of the heat transfer rate of 3.17 MW, the evaporator temperature is set to the value of 390.15 K, and the condenser temperature of 303.15 K, the system produces an output power of 0.45 MW. By reducing the condenser temperature further to 273.15 K, the output power can be increased to approximately 0.7 MW. This shows how lowering the condenser temperature can significantly enhance the power output.

Leveraging DME as a source of cold energy in the integrated system enhances both the operational temperature range and the overall cycle efficiency. Introducing other cooling sources such as liquefied natural gas (LNG), hydrogen, and other cryogenic substances to increase the efficiency of the geothermal cycle could be considered [94]. It is worth noting that each cold source has limitations in its characteristics, operating range, etc. Propane as a working fluid in this study could be a promising option for the LNG cold energy utilization at a certain operating temperature range, similar to the one found in an article [134]. The study [94] finds that a geothermal power generation system that uses DME both as a cold source and as the working fluid in the cycle significantly outperforms other cooling sources when the temperature of the condenser is maintained between 263.15 K and 273.15 K. Moreover, similar improvements in cycle efficiency are observed when liquefied natural gas (LNG) is used as the cooling fluid. Integrating LNG or DME into the geothermal system not only enhances the cycle efficiency of the system but also adds value to geothermal sources with relatively low potential, specifically those with temperatures below 363.15 K.

Further simulation modeling was conducted by considering the wet isentropic efficiency of the volumetric expander that was estimated using an AI model validated with experimental results discussed in Chapter 4. In that case, PE-ORC can used and designed to a integrated system of low-temperature geothermal heat sources and cold energy utilization. In this model, the PE-ORC uses R123 as the

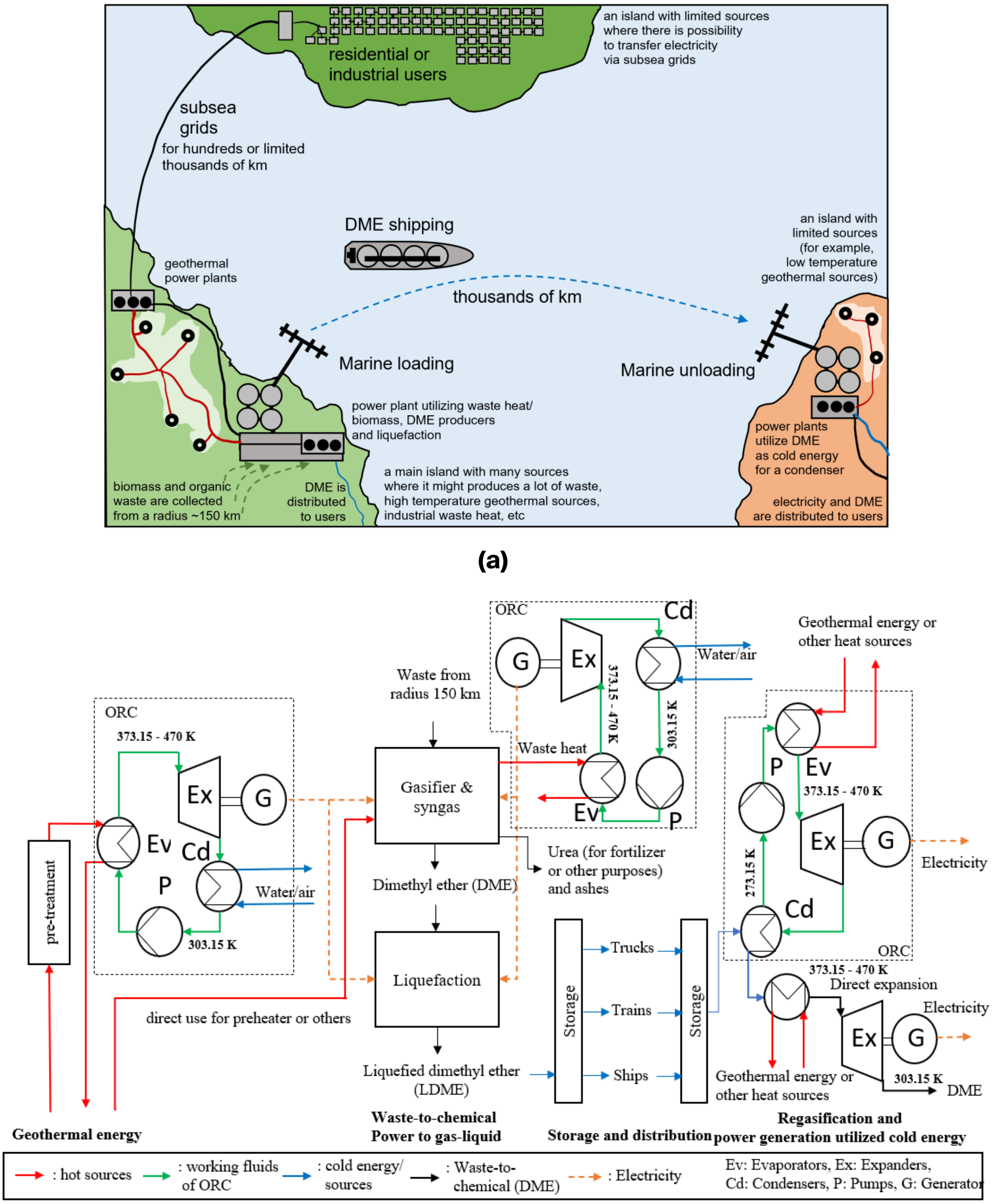

(a)

(b)

Fig. 5.3. An integration of geothermal, cold energy, and waste management system in **(a)** illustration scheme of the value chain, and **(b)** the schematic design, adopted from [15].

working fluid. Assuming the volumetric expander (i.e., a multi-vane volumetric expander) operates with $p_{\text{in}}/p_{\text{out}}$=6.7, x_2=0.95, and T_2=358.15, the validated AI model (the FFDNN with LM) can estimate wet isentropic efficiency $\eta_{\text{is,wet}}$=0.4011. FFDNN with LM was chosen for this simulation due to its high accuracy when using only three input parameters (see Chapter 4 in Fig. 4.5(c), 4.5(d), and Eq. 4.7). Therefore, the ORC efficiency in the integration with geothermal heat sources can be estimated, resulting in a drop to 0.05. It is important to note that this wet isentropic efficiency applies specifically to two-phase multi-vane expanders. Furthermore, assuming a constant mass flow rate of the working fluid, in this case [15], the PE-ORC generates a net output power of 0.58 MW using R123 (which is relatively higher than the above described).

5.3.1.2. Cold energy utilization in pharmaceutical industries

According to the International Energy Agency (IEA) [135], the demand for nitrogen is expected to grow significantly across various applications and industries by 2030 and 2050. Nitrogen, typically procured by manufacturers in liquid form, is essential for numerous processes. To utilize this nitrogen, it must first be regasified, which involves adjusting its temperature and pressure to suitable conditions for use. This process requires heat to convert the liquid nitrogen into its gas state.

Regasification can be achieved through several methods. One common method is simple vaporization, where the nitrogen is converted to gas without any additional utilization of the cold energy. As an alternative approach, the cold energy released during regasification can be captured and used directly for other purposes. Another innovative approach involves using this cold energy as a cooling solution in power generation systems—a technique that can also be applied to other cryogenic liquids such as liquid natural gas, liquid hydrogen, and liquid DME described above.

Part of this chapter includes a discussion, as outlined in [136], focusing on the application of ORC technology in the pharmaceutical industry. Data sourced from a pharmaceutical facility in Hungary showed the monthly consumption of liquid nitrogen, suggesting continuous production. The study aims to explore the potential of utilizing the cold energy released during liquid nitrogen regasification for electricity generation. In this setup, an ORC system is designed to utilize the cold energy as a heat sink, with air serving as the heat source, as illustrated in Fig. 5.4. The liquid nitrogen is pressurized to 3 MPa, with the mass flow rate adjusted based on the monthly consumption data obtained from the Hungarian pharmaceutical industry. Also, the air temperature is assumed based on the monthly mean temperature in Hungary. Propane (R290) is selected as the working fluid for its suitability in leveraging cold energy, as recommended in this article [134]. Moreover, a direct expansion system is also installed in order to generate more power. However, it is worth noting that the vaporizer is required before the nitrogen enters the direct expander.

The results presented in Fig. 5.5 indicate that net power generation from the system varies with changes in ambient air temperature, showing lower power outputs in winter compared to summer. In December, ORC could produce 8.5 kW of gross power and incorporate the direct expansion system; it can produce up to 39 kW. In contrast, in July, the potential gross output power increased to 24 kW (only ORC) and 67.45 kW (ORC and a direct expansion system). As a result, after accounting for the power consumed by the pump and blower/fan, the net electricity generation was 23.72 kW in December with a system efficiency of 13.16%, and 50.02 kW in July with a system efficiency of 15.93%. These variations highlight the dependency of the system's performance on seasonal temperature changes, af-

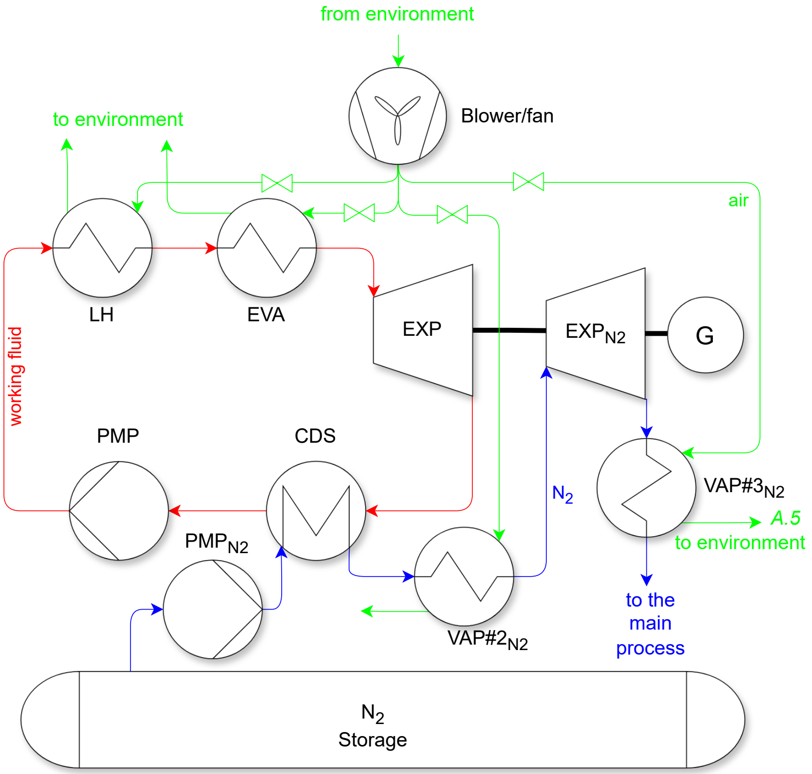

Fig. 5.4. A proposed design of cold energy utilization in the pharmaceutical industry, adapted from [136]. The components labeled in the illustration are LH (liquid heater), EVA (evaporator), EXP (expander), CDS (condenser), PMP (pump), VAP (vaporizer), and G (generator).

fecting the cycle efficiency and output of power generation. It is worth noting that the ORC operates under two-phase conditions, meaning the two-phase expander (e.g., volumetric type) is required.

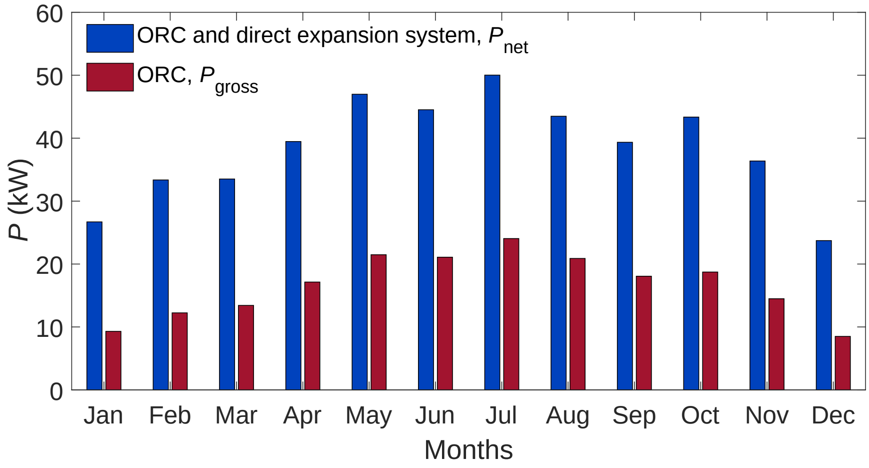

Fig. 5.5. Estimated monthly generated power for cold energy utilization in the pharmaceutical industry, adopted from [136].

Part of this study [136] includes an economic analysis based on the highest net power output observed in July. The investment costs were estimated based on the prices of the various system components. The methodology for estimating these costs, along with some boundary conditions, is detailed in [136]. The costs were adjusted with the current currency exchange rates and the chemical engineering plant cost index to reflect the costs accurately for the year of the calculation and then multiplied with the bare module factor (F_{BM}) [137]. Moreover, the economic analysis further breaks down the costs into several categories: the capital cost of the bare module (C_{BM}), the capital cost of the total module (C_{TM}), the specific investment cost (SIC), and the levelized cost of electricity (LCOE), all of which are outlined in Eqs. 5.2-5.5. To calculate the capital cost of the total module, you need to multiply the capital cost of the bare module by the total module multiplication factor (F_{TM}). According to a study [137], this factor is estimated to be 1.18 which accounts for contractor fees, auxiliary facilities, integration and installation costs, project expenses, and other related costs. In this analysis, the reference year is 2022, the annual discount rate (d) is 6.08%, and the lifespan of the installed system is 20 years. The operating time (t) is estimated to be 254 working days. Moreover, the cost of operation and maintenance (C_{t}) can be calculated using a rate of 0.01 EUR per kWh.

$$C_{\text{BM}} = \sum_{i=1}^{n} C_{\text{p,i}} \cdot F_{\text{BM}} \tag{5.2}$$

$$C_{\text{TM}} = F_{\text{TM}} \sum_{i=1}^{n} C_{\text{BM,i}} \tag{5.3}$$

$$SIC = \frac{C_{\text{TM}}}{P_{\text{net}}} \tag{5.4}$$

$$LCOE = \frac{C_{TM} + \sum_{i=1}^{year} \frac{C_t}{(1+d)^i}}{\sum_{i=1}^{year} \frac{P_{\text{net}} \cdot t}{(1+d)^i}} \tag{5.5}$$

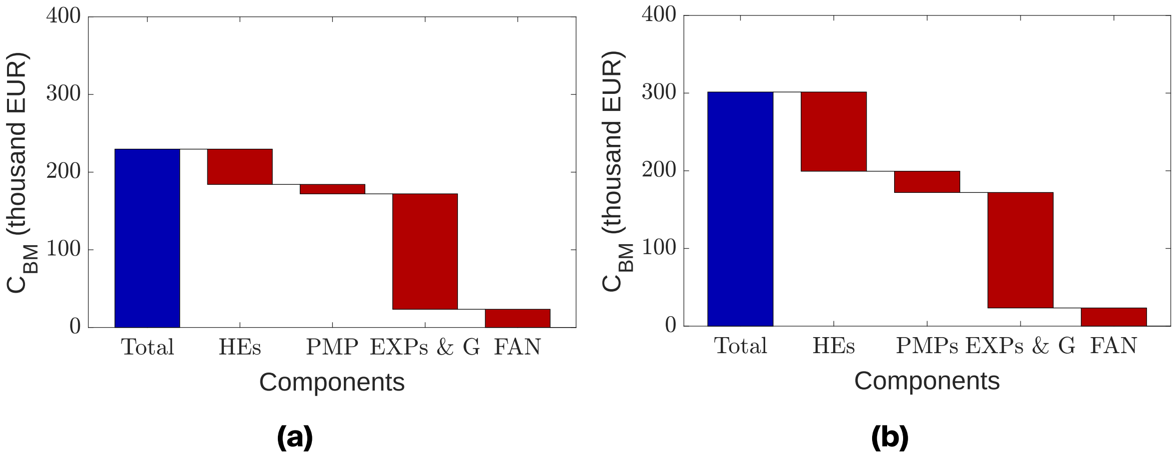

(a) (b)

Fig. 5.6. The capital cost of the bare module for (a) the case of reutilization of the components, and (b) using the new components, adopted from [136].

Table 5.5. A comparison of cost between two cases, adopted from [136].

Parameters	**With reutilization of components**	**New components**
C_{BM} (EUR)	229,627.72	301,394.12
C_{TM} (EUR)	270,960.71	355,645.07
SIC (EUR/kW)	5,417.02	7,110.03
LCOE (EUR/kW)	0.119	0.153

In order to explore cold energy utilization in the pharmaceutical industry with economically viable options, two approaches were considered in the study. The first approach involves redesigning and reutilizing existing components, such as vaporizers, while the second approach proposes replacing the existing system entirely with new components. The study assesses the cost-effectiveness of these two options to determine the most economical approach for implementing cold energy utilization in the pharmaceutical industry. The findings indicate that reutilizing existing components could lead to significant cost savings: up to 56.52 thousand euros on the cost of a bare module and up to 15.52 thousand euros by reusing the nitrogen pump. Additionally, this approach could reduce the capital cost for the bare module by 23.81%. Introducing completely new components for cold energy utilization is more expensive than reutilizing existing components. As detailed in Table 5.5, this option results in an investment cost of 7.11 thousand euros per kW and a total capital cost of 355.65 thousand euros. This approach also results in an LCOE that is 0.034 euros per kW higher than that achieved by reutilizing existing components. Overall, the study demonstrates that using ORC and direct expansion systems with all new components is 31% more expensive in terms of investment costs compared to an approach that reutilizes existing components. This significant difference highlights the economic benefits of optimizing and repurposing existing infrastructure for cold energy utilization in the pharmaceutical industry.

There is potential for further improvement by utilizing heat sources from industrial waste heat below 373.15 K, collected from nearby. In this case, a second ORC can be installed to utilize this industrial waste heat to heat the working fluid, with the heat sink being used to heat up the current ORC as described above. In this case, the second ORC system considers PE-ORC using R123 as the working fluid. Assuming the PE-ORC employing volumetric expander with the vapor quality at the inlet to the expander x=0.95, pressure ratio 6.7, and temperature at the inlet of the expander 348.15 K, the wet isentropic efficiency (predicted using an AI model, FFDNN with LM, validated with experimental data) can be obtained to the value of 0.4011. In that case, the cycle efficiency of PE-ORC can be estimated at 0.057. However, adding a PE-ORC system may increase both investment cost and LCOE. Therefore, further analysis is needed to make cold energy utilization more attractive to the pharmaceutical industry and investors.

5.3.1.3. Waste heat recovery in the paint shop of automotive factory

Waste heat is typically found from the hot surfaces of machinery and equipment, or it accumulates in mediums possessing high internal energy, eventually dissipating into the environment as lost heat. The release of waste heat is particularly irregular, mainly due to the periodic nature of industrial processes, and is characterized by variable outputs and thermal properties. This type of waste heat is also found in some automotive manufacturing facilities. A study [138] highlighted that different stages of automotive production—press, body, paint, final assembly, and processes involving suppliers and vendors—contribute 12%, 10%, 36%, 10%, and 32% respectively to total energy consumption. Notably, the paint shop is the largest consumer of energy within these processes.

Efforts to recover waste heat in automotive paint shops have led to various proposed techniques. However, in practice, the design of heat confinement in baking ovens often proves inadequate. Consequently, considerable heat loss occurs, which not only wastes energy but also significantly raises the air temperature in the working area, creating an uncomfortable environment for factory personnel. To mitigate this, some factories may consider installing chillers to cool the workspace, although this solution increases energy consumption due to the high power requirements for operating the chillers. An ORC system presents a viable alternative, potentially minimizing waste heat release into the working space and reducing overall power consumption. In addition, implementing a combined technology, such as a TES device with a thermodynamic power system, offers a promising solution. This approach enables the recovery and reuse of waste heat, enhancing energy efficiency and workplace conditions in automotive paint shops.

In the preliminary study [139], R1233zd(E) and R1234ze(E) were selected as the working fluids for the ORC system. The expander's inlet conditions were set to be saturated. Given that R1233zd(E) and R1234ze(E) are characterized as isentropic working fluids, the expander operates under superheated conditions. Moreover, only some solid TES materials were chosen for the analysis. The results of this study indicate that the ORC system can effectively recover waste heat from baking ovens, with the temperature range of the TES-evaporator set between 343.15-373.15 K. This process yields a net output power ranging from 53-89 kW, achieving a cycle efficiency between 0.067-0.110. These findings suggest the feasibility of implementing such an ORC system for waste heat recovery in automotive paint factories. It seems that using an ORC with a two-phase expansion system, also known as PE-ORC, could optimize the utilization of heat sources in this scenario. However, further investigation into this possibility is still necessary.

Further modeling simulation was conducted considering the wet isentropic efficiency of the volumetric expander taken from the AI prediction model that has been validated using experimental data (see Chapter 4. The FFDNN model was employed to predict the wet isentropic efficiency. The waste heat recovery can be done using PE-ORC with x_2=0.95, and in that case, the efficiency of waste heat utilization can be improved. However, considering the R123 as the working fluid in the system, the results show that the cycle efficiency of ORC drops to η_{ORC}=0.057.

5.3.2. Discussion on two-phase expansion system in a reversible ORC/heat pump

5.3.2.1. A case study of district heating system

A district heating system typically consists of a centralized facility that generates heat and distributes it to residential buildings via a network of insulated pipes. This heat is often produced by burning fossil fuels or biomass. Given increasing environmental regulations and rising demand for heat and energy, incorporating industrial waste heat and renewable energy sources like solar thermal or geothermal energy into district heating is becoming increasingly attractive. In some areas, available heat sources may only produce low temperatures. To bridge this gap, a heat pump is used to elevate the temperature to meet peak demand loads. These heat pumps are operational only during specific periods and are often idle during the summer months (the district heating is not used during summer). Therefore, in this case, the heat source is considerably excess heat. To enhance the efficiency and utilization of these heat sources, the district heating system could be adapted to also function as a power generation system. This modification would allow the system to produce electricity instead of heat during the less demanding summer period, optimizing the use of available resources.

Part of this study, as described in [140], explores a viable solution for a low-temperature district heating (LTDH) system that incorporates a heat pump and ORC system. There is an increasing interest in utilizing low-temperature heat sources from renewable energy, including solar thermal, geothermal, waste heat, and biomass, for LTDH systems. A reversible ORC/heat pump system featuring a two-phase expander is introduced as an innovative design alternative for managing the operation and heating demand loads of LTDH systems, as shown in Fig. 5.7.

The study assumes that the base demand of the LTDH system uses geothermal heat for at least 5,000 hours annually and operates intermittently, as depicted in Figure 5.7(a). To satisfy peak demand, the heat pump is required to run for at least 3,000 hours, while gas combustion covers an additional 2,000 hours. Given the yearly total of 8,760 hours, there are 3,760 hours during which no heating is required, and during these hours, geothermal energy remains untapped. The idea suggests that during these off-peak periods, geothermal energy could be harnessed to generate electricity using the ORC. The reversible ORC/heat pump design, detailed in Fig. 5.7(c)-(d), offers a promising approach. It is proposed to operate for 3,000 hours as a heat pump and for 3,760 hours as an ORC, thereby enhancing the versatility and competitiveness of this integrated system in the LTDH framework.

In this study [140], DME and R152a were selected as working fluids for a reversible system. The methodology and specific boundary conditions are detailed within this article [140]. A key aspect of the study was the comparison between reversible systems using a throttle valve and those employing a two-phase expander in the heat pump mode. The results indicated that the reversible ORC/heat pump system using R152a as the working fluid could reject up to 234.45 MWh in the heat pump mode, which is 4.32 MWh more than the configuration using DME. Using a throttle valve in a heat pump typically requires more energy due to the lack of energy utilization for power generation. For instance, the energy consumption for operating the heat pump was 53.66 MWh for R152a (with a COP of 3.51) and 47.12

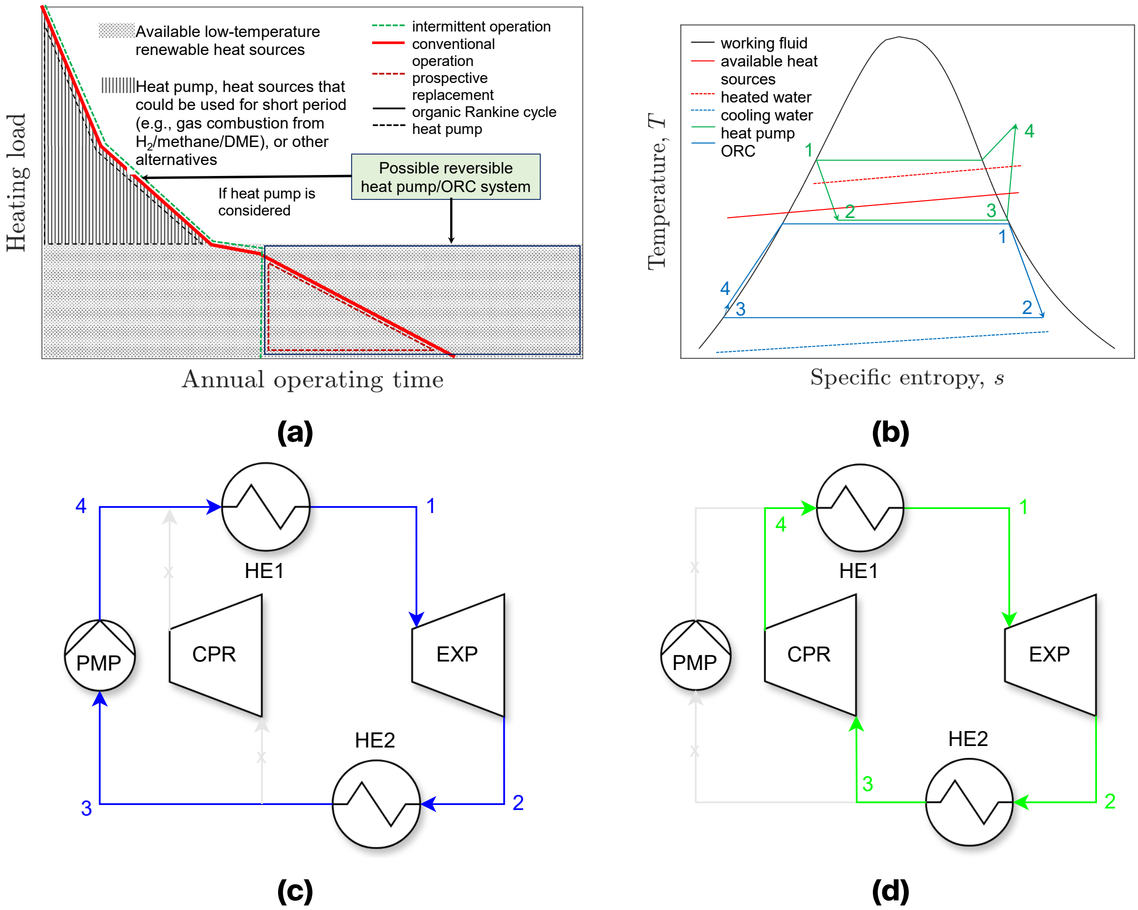

Fig. 5.7. A novel reversible ORC/heat pump in (a) the annual operation time and heating load diagram, (b) the operation in $T-s$ diagram, (c) the design in ORC mode, and (d) in heat pump mode, adopted from [140].

MWh for DME (with a COP of 4). By replacing the throttle valve with a two-phase volumetric expander integrated with a generator, the energy consumption could be reduced by 7.82 MWh for R152a and 5.59 MWh for DME. Moreover, the COP of the heat pump mode could improve to 4.11 for R152a and 4.54 for DME. By switching the reversible ORC/heat pump to ORC mode during the summer to utilize excess heat for electricity generation, the system using R152a could produce 22.45 MWh of energy, and the system using DME could generate 22.20 MWh. Under these conditions, the cycle efficiency in ORC mode could reach 7.39% for R152a and 7.47% for DME. Overall, this study demonstrates that a district heating system employing a reversible ORC/heat pump system consumes less energy overall. Specifically, the total net energy usage of the system was calculated to be 23.39 MWh for R152a and 19.32 MWh for DME, showcasing the energy efficiency benefits of integrating a two-phase expander over a traditional throttle valve in these systems.

The further simulation, in this case, utilizes the wet isentropic efficiency of a multi-vane volumetric expander, derived from an AI prediction model (FFDNN with LM) and validated by experimental results discussed in Chapter 4. In this district heating system, R123 is selected as the working fluid. For heat generation, a PE-ORC system is employed, with x_2=0.95. Assuming that geothermal heat is taken from 353.15 K and water is heated to 373.15 K using a heat pump, where the pinch point temperature is 5 K, the cycle efficiency of the PE-ORC is 0.057, and the COP is 9.18. These results were obtained when considering the wet isentropic efficiencies of the volumetric expander during PE-ORC mode and heat pump mode are 0.4011 (taken form the FFDNN with LM) and 0.3, respectively. Also, The results show that using a two-phase expander in the heat pump to replace the throttle valve can reduce energy consumption by up to 0.47 MWh. When the PE-ORC system is employed to utilize geothermal heat during summer, it can generate up to 7.88 MWh of energy. However, these results are somewhat low due to the influence of the low wet isentropic efficiency of the two-phase multi-vane volumetric expander.

5.3.2.2. A case study of Carnot battery

A reversible ORC/heat pump system can be effectively integrated into Carnot battery technology, which is recognized for its ability to store energy for future use. In this case, daily TES is preferred over seasonal or large TES to minimize heat transfer losses. As detailed in the studies referenced in [128, 141], the performance map of a Carnot battery utilizing a reversible ORC/heat pump is explored. Nine working fluids were evaluated based on factors such as their operating temperature range, GWP, ozone ODP, toxicity, and others. Given DME's promising performance in other applications, as previously mentioned, it is also selected as the representative working fluid for Carnot battery technology via a reversible ORC/heat pump system. Fig. 5.8 presents the result of the performance map for the Carnot battery using DME as a working fluid.

Fig. 5.8(a) shows that the Carnot battery achieves a COP of 21.207 when it is operating with a waste heat carrier fluid temperature at 328.15 K and a cooling carrier fluid temperature at 303.15 K. It is worth noting that while commercial heat pumps typically achieve a COP=4-5, a heat pump with COP=20 is generally not available on the market. Further adjustments in temperatures result in varying COP levels, as follows:

- When the temperature of cooling carrier fluid remains at 303.15 K but the temperature of waste heat carrier fluid increases to 343.15 K, the COP decreases by 39.29%.
- Maintaining the temperature of waste heat carrier fluid at 328.15 K while reducing the temperature of cooling carrier fluid to 288.15 K results in a 50.75% reduction in COP.
- A combined adjustment where the temperature of waste heat carrier fluid increases from 328.15 K to 343.15 K and the temperature of cooling carrier fluid decreases from 303.15 K to 288.15 K leads to a substantial COP reduction of 62.67

Furthermore, Fig. 5.8(b) demonstrates the effects of these temperature changes on the ORC mode efficiency within the Carnot battery system, as follows:

- With the temperature of waste heat carrier fluid at 328.15 K and the temperature of cooling carrier fluid at 303.15 K, an ORC mode efficiency of 0.072 is achieved.

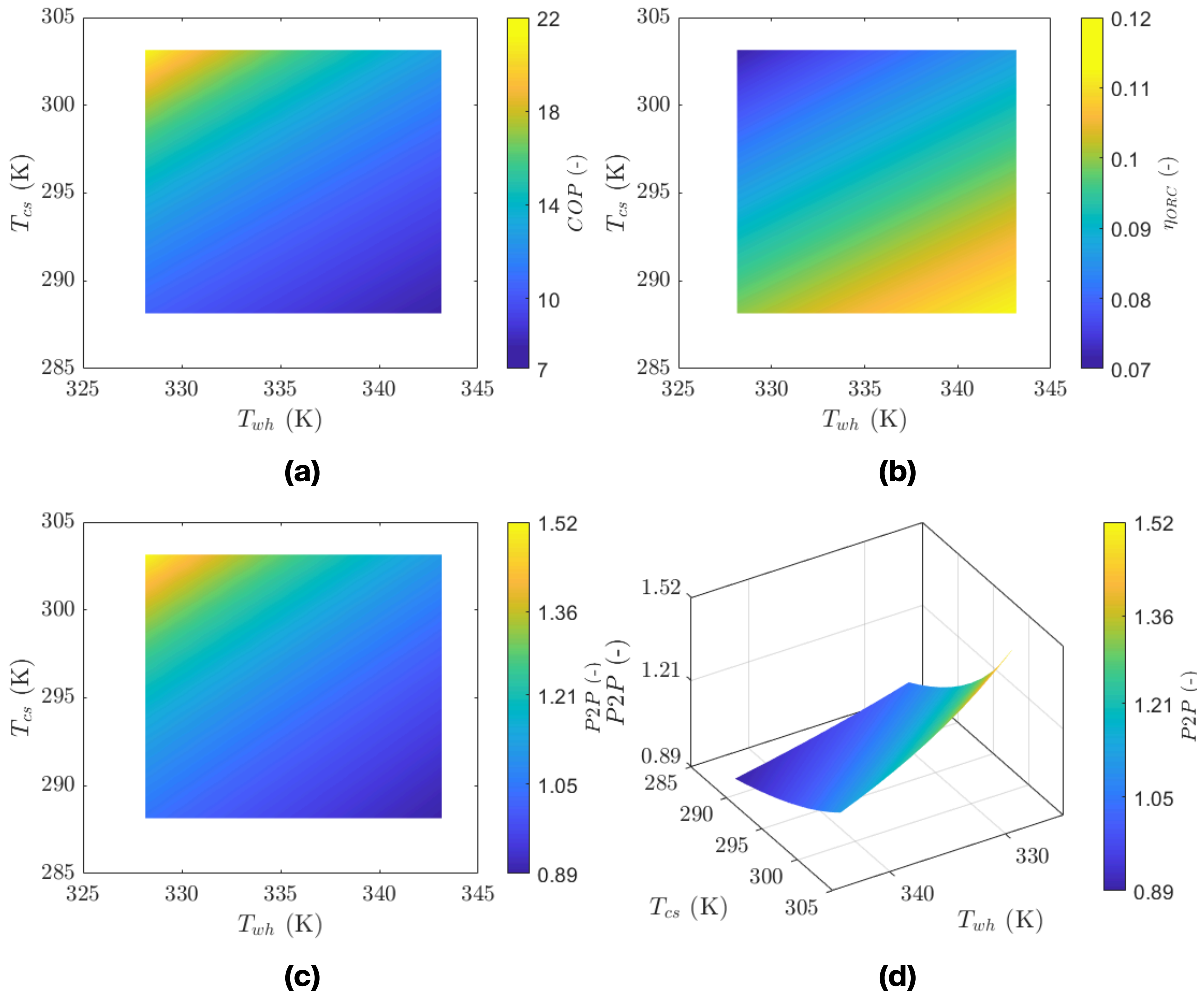

(a) (b) (c) (d)

Fig. 5.8. Obtained performance map of Carnot battery via a reversible ORC/heat pump system using DME in **(a)** heat pump mode illustrated in $T_{wh} - T_{cs} - COP$ diagram, **(b)** ORC mode illustrated in $T_{wh} - T_{cs} - \eta_{ORC}$ diagram, **(c)** P2P in $T_{wh} - T_{cs} - P2P$ diagram (2D view), and **(d)** P2P in $T_{wh} - T_{cs} - P2P$ diagram (2D view), adopted from [128].

- By keeping the temperature of cooling carrier fluid constant at 303.15 K but raising the temperature of waste heat carrier fluid to 343.15 K results in a significant 20.72% increase in ORC efficiency.
- By keeping the temperature of waste heat carrier fluid at 328.15 K and lowering the temperature of cooling carrier fluid to 288.15 K results in a substantial ORC efficiency increase of 39.23%.
- An increase in the temperature of waste heat carrier fluid from 328.15 K to 343.15 K coupled with a decrease in the temperature of cooling carrier fluid from 303.15 K to 288.15 K enhances the ORC mode efficiency by 57.51%.

Based on the COP and the cycle efficiency of the ORC mode, the P2P ratio can be calculated for the Carnot battery system. The data indicates that with a waste heat carrier fluid temperature of 328.15 K and an ORC cooling temperature of 303.15 K, a P2P performance of 1.518 is achieved. However, adjustments in temperature affect this performance, as follows:

- With the temperature of cooling carrier fluid maintained at 303.15 K but the temperature of waste heat carrier fluid increased to 343.15 K, the P2P decreases by 26.71%.
- By maintaining the temperature of waste heat carrier fluid at 328.15 K while lowering the temperature of cooling carrier fluid to 288.15 K, 31.42% P2P reduction can be obtained.
- Furthermore, by increasing the temperature of waste heat carrier fluid from 328.15 K to 343.15 K while simultaneously decreasing the temperature of cooling carrier fluid from 303.15 K to 288.15 K, a substantial decrease in P2P by 41.21% is observed.

The results indicate that by increasing the temperatures of both the cooling source and the waste heat carrier fluids, an increase in the P2P ratio can be obtained. This pattern of gradual improvement across the diagonal path is consistent even when different working fluids are used. A comparative analysis of the COP, the cycle efficiency of ORC operaing mode, and the P2P of the Carnot batter via a reversible ORC/HP system is visually represented in Fig. 5.9, highlighting the different temperature ranges and the selected working fluids that affect the performance of the system.

A comparative result of performance evaluation for Carnot battery in heat pump operating mode shows that R152a, RE170, and R13I1 demonstrate higher COP compared to other working fluids, which is illustrated in Fig. 5.9(a). However, it is noted that R13I1 has the lowest cycle efficiency in ORC operating mode, then followed by RE170. In contrast, R1234ze(Z), isobutane, and butene show higher cycle efficiency in Carnot battery operation in ORC operating mode than the other fluids tested, which is depicted in Fig. 5.9(b). In terms of P2P, which is illustrated in Fig. 5.9(c), R152a and R13I1 outperform the other working fluids evaluated for use in Carnot battery technology. Notably, the Carnot battery using R152a achieves the best overall P2P among the substances examined, with R152a consistently showing higher P2P results than R13I1 across various tests. It seems that Carnot battery via a reversible ORC/heat pump system utilizing R152a as the working fluid surpasses all other tested fluids, achieving the highest recorded P2P of 1.575. This suggests that R152a is a particularly effective option for Carnot battery technology under the evaluated conditions. Moreover, R13I1 and RE170 also show promising with P2P ratios of 1.541 and 1.518, respectively. It indicates that both are viable options for achieving efficient power-to-power conversions in Carnot battery systems via a reversible ORC/heat pump system.

Part of this study, published in [128], includes a comparative analysis of the Carnot battery's performance using Baumann's rule applied to the isentropic efficiency of the expander in the heat pump operating mode. The results show a difference in COP when Baumann's correlation is used versus when it does not range from 2.46% to 9.42%. The most significant COP difference was observed with R1234ze(E) as the working fluid, while the smallest difference was noted with R1234ze(Z). Moreover, the study compares P2P differences in the Carnot battery employing various working fluids, with and without the application of Baumann's correlation. These differences ranged from 2.46% to 14.06%. The greatest P2P difference was found with the Carnot battery using R1234ze(E) as the working fluid.

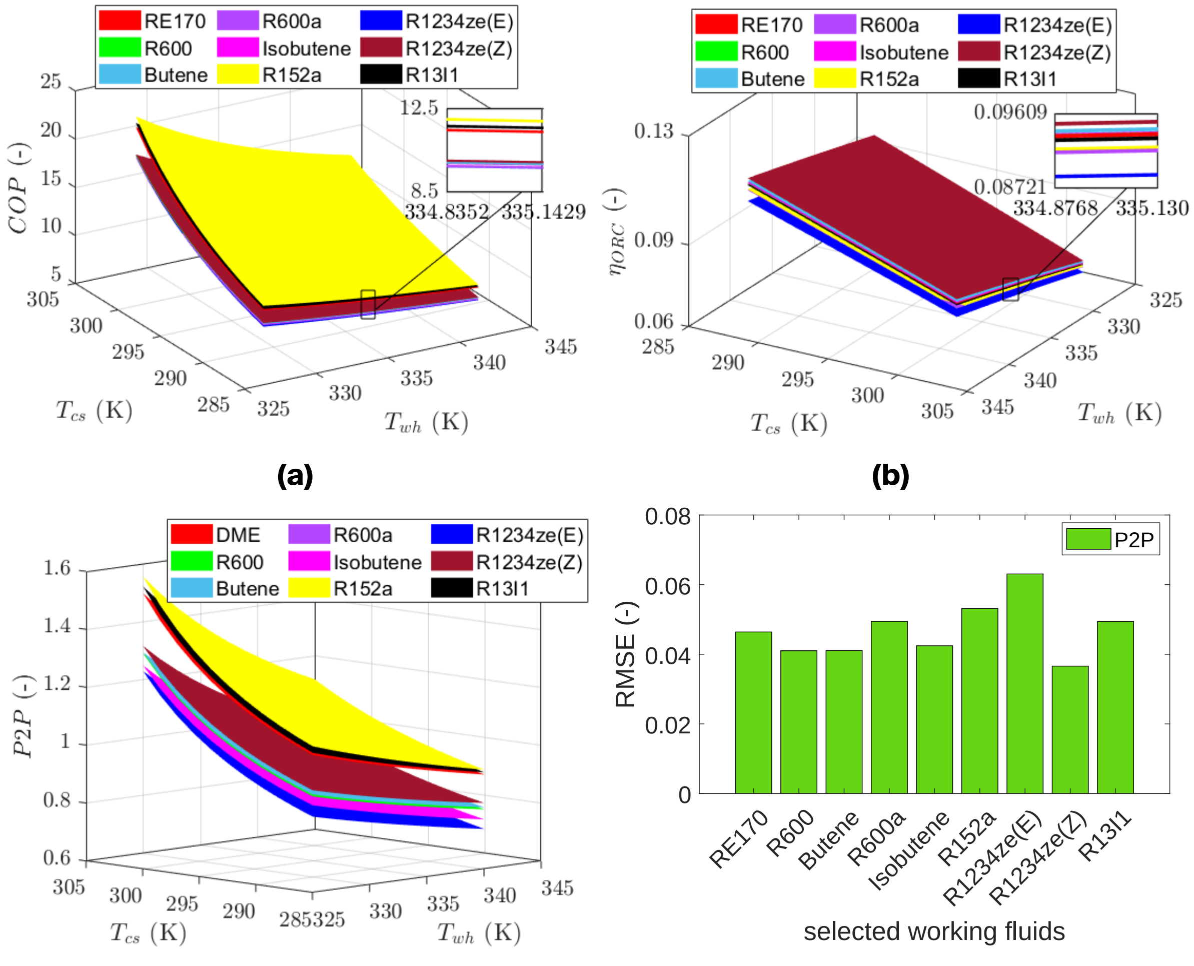

(a)

(b)

(c)

(d)

Fig. 5.9. A comparative performance of Carnot battery using a reversible ORC/heat pump system in **(a)** heat pump mode illustrated in $T_{wh} - T_{cs} - COP$ diagram (3D view), **(b)** ORC mode illustrated in $T_{wh} - T_{cs} - \eta_{ORC}$ diagram (3D view), **(c)** P2P in $T_{wh} - T_{cs} - P2P$ diagram (3D view), and **(d)** RMSE of P2P in working fluid and RMSE diagram, adopted from [128].

The study suggests that modeling results without Baumann's rule are generally acceptable as long as the performance difference remains below 10% for some working fluids. Moreover, the obtained results shown in Fig. 5.9(d) show that RMSE for P2P values in the study ranges from 0.036 to 0.063. Considering that the target P2P values vary from 0.74 to 1.57, these RMSE values can be considered relatively high. Further analysis shows that the highest RMSE value for P2P, at 0.036, occurred with R1234ze(E) as the working fluid, whereas the lowest RMSE, at 0.063, was associated with R1234ze(Z). This suggests a significant variation in prediction accuracy across different working fluids within the study.

Furthermore, the wet isentropic efficiency can be estimated using an AI model validated with experimental results discussed in Chapter 4. This model can design a system integrating low-temperature geothermal heat sources and cold energy utilization. The system employs a PE-ORC and a volumetric expander using R123, with the wet isentropic efficiency predicted by the AI. Assuming a multi-vane volumetric expander operates with $p_{\text{in}}/p_{\text{out}}$=6.7, x_2=0.95, and T_2=348.15, the validated AI model (the FFDNN with LM) can estimate wet isentropic efficiency $\eta_{\text{is,wet}}$=0.4011. Therefore, the ORC efficiency in this case drops to 0.057. It's important to note that this wet isentropic efficiency specifically applies to two-phase multi-vane expanders. Due to limitations in predicting the wet isentropic efficiency, the expander in the heat pump is assumed to be $\eta_{\text{is,wet}}$=0.3. The results from the simulation show COP=8.75, resulting in the $P2P$=0.5032. This low P2P is influenced by the wet isentropic efficiency of the multi-vane expander that was predicted using AI validated by the experimental data. Moreover, it is important to note that in actual operating conditions, P2P might be less than 1 due to the low COP of real systems, as reported in this article [123].

5.4. Conclusions

This chapter explores the application of a two-phase expansion system in enhancing ORC systems. It highlights how this system can be integrated with low- and medium-temperature geothermal heat sources, utilized for cold energy, and employed in waste heat recovery. Moreover, the two-phase expansion system offers the potential to simplify the system architecture by functioning as a reversible machine, thus reducing the number of components required. To summarize the key findings of this chapter, the conclusions are presented in Thesis 7.

Thesis 7. *The incorporation of a two-phase expansion system in an organic Rankine cycle (ORC) system significantly enhances its adaptability to the application in fluctuated low- and medium-temperature heat sources (both renewable and waste heat). This system maintains optimal cycle efficiency across wider operational conditions compared to ORC systems with a superheater that operates under superheated conditions. It also shows particular promise, which has been described in some cases as influencing the geothermal power plant and cold energy utilization. By employing a two-phase expansion system, there is not only an increase in the ability to utilize fluctuating low- and medium-temperature heat sources but also a potential increase in output power. Moreover, the two-phase expansion system allows the ORC to be configured in a reversible cycle incorporating a heat pump mode. In that case, the two-phase expander replaces the throttle valve used in heat pump mode. This adaptation reduces the number of components necessary in applications such as district heating systems and Carnot batteries. It presents a cost-effective and technologically advanced option for future implementation, offering both efficiency and operational flexibility in energy conversion systems.*

The publications by the author that are related to Thesis 7 are [13, 14, 15, 94, 128, 136, 139, 140, 141].

6

Summary

Among the various thermodynamic power cycles available, advancing the ORC system as power generation is seen as particularly promising. The ORC offers the adaptability to change working fluids and operational conditions. The ORC can be operated under subcritical and transcritical operating conditions. The aim of this dissertation is the analysis of the low-boiling working fluid expansion process in the ORC system. The volumetric expanders were chosen as the main focus of the investigation. To encapsulate the main contributions and key findings from this dissertation, the thesis points from the earlier chapters are re-stated and presented below.

6.1. The influence of low-boiling working fluid expansion process to different ORC systems under subcritical conditions

Different ORC systems are analyzed under subcritical operating conditions. PE-ORC, which is ORC with a two-phase expansion system or ORC with a partial evaporation process (PE-ORC), serves as a transitional cycle, bridging the ORC and TFC. An analysis of the low-boiling working fluid expansion process to see the influence on different ORC systems has been conducted. The cycle efficiency of different ORC systems has been analyzed and compared. This chapter theoretically proved that, in some cases, increasing the temperature and pressure range of the expander does not necessarily result in enhanced cycle efficiency across various ORC systems operating under subcritical conditions. The main contributions and key findings are described in Thesis 1 and Thesis 2.

Thesis 1. *The theoretical modeling simulation result shows that under subcritical operating conditions, the cycle efficiency of partially evaporated organic Rankine cycle (PE-ORC) is not always located between that of organic Rankine cycle (ORC) with the saturated vapor state of the working fluid at the inlet to the expander and trilateral flash cycle (TFC or trilateral ORC) in the cycle efficiency and temperature of the working fluid at the inlet to the expander* ($\eta_{cycle} - T_2$) *diagram. The observation using dry and some isentropic working fluids shows that PE-ORCs have the potential to achieve higher cycle efficiency than both ORC and TFC, especially when the* *modeling simulation assumes a certain isentropic efficiency for both the pump and expander. This observation highlights the importance of choosing the appropriate working fluid for specific subcritical power cycles, offering new insights into the selection process. In designing the PE-ORC or TFC with higher cycle efficiency, it is suggested to design the cycle using dry working fluids.*

Thesis 2. *Increasing the operating temperature range of the low-boiling working fluid expansion process in the organic Rankine cycle (ORC) with the saturated vapor state of the working fluid, partially evaporated organic Rankine cycle (PE-ORC), and trilateral flash cycle (TFC or trilateral ORC) with various types of working fluids may improve the cycle efficiency under subcritical operating conditions; however, this improvement is specific to certain operating temperature ranges. When the temperature of the working fluid to the expander inlet is fixed, and the temperature of the working fluid from the expander outlet is below 273.15 K, the cycle efficiency of the ORC, PE-ORC, and TFC is increased. Nonetheless, when increasing the temperature of the working fluid to the expander inlet near the critical point, the maximal cycle efficiency (i.e., a peak cycle efficiency) can be observed in the cycle efficiency and temperature of the working fluid at the expander inlet ($\eta_{\text{cycle}} - T_2$) diagram. This observation implies that any increase in the temperature of the working fluid to the expander inlet beyond this point (the temperature when the maximal cycle efficiency is achieved) may result in a decrease in efficiency. This trend in cycle efficiency can be observed not only in ORC but also in PE-ORC and TFC. In scenarios involving isentropic and dry working fluids, the cycle efficiency of PE-ORCs or TFC may be over the maximal cycle efficiency of ORC with saturated vapor state of the working fluid at the inlet to the expander under both ideal and certain conditions.*

Thesis 1 and Thesis 2 provide main contributions to a theoretical foundational understanding of the operating conditions of a volumetric expander functioning under subcritical conditions. These theses delve into the impact of increased temperature and pressure ratio ranges, as well as the vapor quality at the inlet to the expander. This understanding is crucial for the appropriate selection of ORC systems utilizing a two-phase volumetric expander and selected low-boiling working fluid, ensuring optimal cycle efficiency.

6.2. The influence of low-boiling working fluid expansion process to different ORC systems under subcritical and transcritical conditions

The theory of the Carnot cycle suggests that a wider operating temperature range can enhance the overall cycle efficiency. This principle is applicable to different ORC systems under subcritical and transcritical operating conditions. This chapter theoretically proved that in some cases increasing the temperature and pressure range of the expander does not necessarily result in improved cycle efficiency across ORC system under both subcritical and transcritical operating conditions. The main contributions and key findings are presented in Thesis 3 and Thesis 4.

Thesis 3. *Under ideal operating conditions (i.e., considering isobaric evaporation, isentropic expansion, isobaric condensation, and isentropic pump process), an increased operating temperature range of the low-boiling working fluid expansion process in the organic Rankine cycle (ORC), partially evaporated ORC, ORC with a superheater, and trilateral flash cycle likely enhances cycle efficiency. This approach also applies to the transcritical power cycle (TPC). Nonetheless, when taking the isentropic efficiency of the expander into account, a maximal cycle efficiency point for TPC can be observed. This maximal cycle efficiency of TPCs underscores the significance of selecting an optimal temperature range and pressure ratio of the low-boiling working fluid expansion process and type of thermodynamic power cycle, providing perspectives on the decision-making process for utilizing organic working fluids.*

Thesis 4. *In evaluating the cycle efficiency of various transcritical power cycle (TPC) configurations with different values of vapor quality from the expander outlet, using either wet or isentropic working fluids, an equal efficiency point (EEP) can typically be identified under ideal operating conditions (i.e., considering isobaric evaporation, isentropic expansion, isobaric condensation, and isentropic pump process). However, when employing carbon dioxide or water as working fluids, this EEP cannot be located. Moreover, a scenario may arise where the TPC exhibits negative efficiency, especially when considering higher operating temperature and pressure ratio ranges of the low-boiling working fluid expansion process, along with the isentropic efficiency of the expander. As an example, if the isentropic efficiency were set to the value of 0.8, this negative TPC efficiency would occur as the enthalpy change in the expander is lower than the enthalpy change in the pump. This example theoretically proves that increasing the operating temperature and pressure ratio range of the low-boiling working fluid expansion process does not guarantee an improvement in cycle efficiency.*

Thesis 3 and Thesis 4 provide extended main contributions to a theoretical foundational understanding of the operating conditions of a volumetric expander functioning under subcritical and transcritical conditions. These theses also delve into the impact of increased temperature and pressure ratio ranges, as well as the vapor quality at the inlet to the expander. This understanding is crucial for the appropriate selection of ORC systems under transcritical conditions that use a two-phase volumetric expander and a selected low-boiling working fluid, ensuring optimal cycle efficiency. In some ORC systems operating under transcritical conditions, certain temperature and pressure ranges of the expander and vapor quality must be avoided to prevent negative efficiency.

6.3. Experimental validation and prediction of wet isentropic efficiency in two-phase volumetric expander in an ORC system

Part of the investigation in this dissertation reported the experimental study focused on predicting wet isentropic efficiency in a two-phase expansion system. The multi-vane volumetric expander was chosen in the experimental investigation of the ORC system. This chapter proved that a multi-vane expander can be used in the ORC system operating under two-phase conditions. The main contributions and key findings are presented in Thesis 5 and Thesis 6.

Thesis 5. *A low-boiling working fluid expansion process in an organic Rankine cycle system can be done under two-phase conditions with a multi-vane expander using 2,2-Dichloro-1,1,1-trifluoroethane (R123) as the working fluid. Under the vapor quality at the inlet to the expander* x_2*=0.93-0.98, pressure ratio* p_{in}/p_{out}*=5.67-10.67, density ratio* ρ_{in}/ρ_{out}*=7.4-13.3, and the temperature at the inlet to the expander* T_2*=347.95-358.15 K, the wet isentropic efficiency of the multi-vane expander* $\eta_{wet,is}$*=0.37-0.49 can be obtained with the measurement uncertainty ca.* $\pm$ *0.045.*

Thesis 6. *Predicting wet isentropic efficiency can be done using deep learning or deep neural networks (DNNs), which are methods within the field of artificial intelligence. Low accuracy of prediction was observed when using only the pressure ratio and vapor quality at the expander inlet as input variables of DNN for determining the wet isentropic efficiency of low-boiling working fluid expansion processes. However, adding the temperature of working fluid to the expander inlet as an additional input parameter of the DNN significantly enhances the accuracy of the model, reducing the root mean squared error (RMSE) by up to 68% and increasing the coefficient of determination* R^2 *by up to four times compared to the initial DNN model (using pressure ratio and vapor quality at the inlet to the expander). It is worth noting that using density ratio-based prediction offers higher accuracy in predicting the wet isentropic efficiency of the expander compared to using pressure ratio-based prediction. Furthermore, introducing the expander rotational speed as a fourth input parameter of DNN maintains similar RMSE and* R^2 *values as the three-parameter model but improves computational efficiency, speeding up the prediction time by 2.25% to 49.70%.*

Thesis 5 and Thesis 6 contribute to the experimental validation and the prediction of the wet isentropic efficiency of the volumetric expander, especially using a multi-vane expander with eight vanes. Prediction of wet isentropic efficiency is essential in order to make further analysis and investigation on ORC systems with two-phase expansion systems, such as PE-ORC and TFC, which could benefit from harnessing low and medium-temperature heat sources.

6.4. An increased adaptability of ORC with two-phase expansion system

This study shows that incorporating a two-phase expansion system into ORC configurations significantly improves adaptability when dealing with fluctuating low- and medium-temperature heat sources. It may also potentially increase the output power as power generation. This chapter proved that using a two-phase volumetric expansion system can improve the adaptability of the ORC system, enabling the extension application and wider operating conditions to effectively utilize low- and medium-temperature heat sources. The main contributions and key findings are described in Thesis 7.

Thesis 7. *The incorporation of a two-phase expansion system in an organic Rankine cycle (ORC) system significantly enhances its adaptability to the application in fluctuated low- and medium-temperature heat sources (both renewable and waste heat). This system maintains optimal cycle efficiency across wider operational conditions compared to ORC systems with a superheater that operates under superheated conditions. It also shows particular promise, which has been described in some cases as influencing the geothermal power plant and cold energy utilization. By employing a two-phase expansion system, there is not only an increase in the ability to utilize fluctuating low- and medium-temperature heat sources but also a potential increase in output power. Moreover, the two-phase expansion system allows the ORC to be configured in a reversible cycle incorporating a heat pump mode. In that case, the two-phase expander replaces the throttle valve used in heat pump mode. This adaptation reduces the number of components necessary in applications such as district heating systems and Carnot batteries. It presents a cost-effective and technologically advanced option for future implementation, offering both efficiency and operational flexibility in energy conversion systems.*

Thesis 7 contributes to the extended application and adaptability of the volumetric expander. An ORC system employing a volumetric expander enables the extension of the wider application and operating condition in order to efficiently harness low and medium-temperature heat sources.

6.5. Further direction of the research on this topic

This dissertation shows that PE-ORC can outperform ORC and TFC under certain operating conditions. In some cases, TFC can also outperform ORC systems. These PE-ORC and TFC employ a two-phase expander in the systems. Therefore, future research on the use of a two-phase expander in ORC systems could delve into several promising areas. Firstly, there is a need to investigate various configurations of two-phase expanders, as these have not been extensively studied in both ORC and OFC systems. Understanding how these configurations can be optimized for specific applications will be crucial.

Furthermore, developing advanced simulation models could greatly improve the accuracy of predictions about two-phase expander performance. These models should include computational fluid dynamics to better reflect real-world conditions. Such advancements are crucial for a deeper theoretical understanding before practical implementation. Moreover, experimental validation is essential to support the findings from simulations. More experimental work on two-phase expanders will offer crucial data, especially regarding how this technology can be scaled from lab to industrial use. This research is key to identifying and addressing the challenges of applying two-phase expanders on a larger scale and assessing their potential advantages.

References

[1] Caglar, A. E. and Askin, B. E. “A path towards green revolution: How do competitive industrial performance and renewable energy consumption influence environmental quality indicators?” In: *Renewable Energy* 205 (2023), pp. 273–280. DOI: `10.1016/j.renene.2023.01.080`.

[2] McGlade, C. and Ekins, P. “The geographical distribution of fossil fuels unused when limiting global warming to 2°C”. In: *Nature* (2015), pp. 187–190. DOI: `10.1038/nature14016`.

[3] Elavarasan, R. M. et al. “Envisioning the UN Sustainable Development Goals (SDGs) through the lens of energy sustainability (SDG 7) in the post-COVID-19 world”. In: *Applied Energy* 292 (2021), p. 116665. DOI: `10.1016/j.apenergy.2021.116665`.

[4] Jiménez-Arreola, M. et al. “Thermal power fluctuations in waste heat to power systems: An overview on the challenges and current solutions”. In: *Applied Thermal Engineering* 134 (2018), pp. 576–584. DOI: `10.1016/j.applthermaleng.2018.02.033`.

[5] Hundy, G.F., Trott, A.R., and Welch, T.C. *Refrigeration, Air Conditioning and Heat Pumps*. Fifth Edition. Butterworth-Heinemann, 2016. ISBN: 978-0-08-100647-4.

[6] Daniarta, S., Imre, A. R., and Kolasiński, P. “Thermodynamic efficiency of subcritical and transcritical power cycles utilizing selected ACZ working fluids”. In: *Energy* 254 (2022), p. 124432. DOI: `10.1016/j.energy.2022.124432`.

[7] Maraver, D. et al. “Systematic optimization of subcritical and transcritical organic Rankine cycles (ORCs) constrained by technical parameters in multiple applications”. In: *Applied Energy* 117 (2014), pp. 11–29. DOI: `10.1016/j.apenergy.2013.11.076`.

[8] Algieri, A. and Morrone, P. “Comparative energetic analysis of high-temperature subcritical and transcritical Organic Rankine Cycle (ORC). A biomass application in the Sibari district”. In: *Applied Thermal Engineering* 36 (2012), pp. 236–244. DOI: `10.1016/j.applthermaleng.2011.12.021`.

[9] Wieland, Christoph et al. “Innovations for organic Rankine cycle power systems: Current trends and future perspectives”. In: *Applied Thermal Engineering* 225 (2023), p. 120201. DOI: `10.1016/j.applthermaleng.2023.120201`.

[10] Dickes, R. et al. “From 1885 to nowadays: a (short) techno-historical review of solar organic Rankine cycle systems”. In: *Proceedings of the 6th International Seminar on ORC Power Systems*. Ed. by Munich, Technical University of. Technical University of Munich. Technical University of Munich, 2021. DOI: 10.14459/2021mp1633111.

[11] Wieland, C. et al. “The organic Rankine cycle power systems market: Recent developments and future perspectives”. In: *Applied Thermal Engineering* 224 (2023), p. 119980. DOI: 10.1016/j.applthermaleng.2023.119980.

[12] Quoilin, S. et al. “Techno-economic survey of Organic Rankine Cycle (ORC) systems”. In: *Renewable and Sustainable Energy Reviews* 22 (2013), pp. 168–186. DOI: 10.1016/j.rser.2013.01.028.

[13] Imre, A. R. et al. “Design, Integration, and Control of Organic Rankine Cycles with Thermal Energy Storage and Two-Phase Expansion System Utilizing Intermittent and Fluctuating Heat Sources—A Review”. In: *Energies* 16 (2023). DOI: 10.3390/en16165948.

[14] Daniarta, S., Nemś, M., and Kolasiński, P. “A review on thermal energy storage applicable for low- and medium-temperature organic Rankine cycle”. In: *Energy* 278 (2023), p. 127931. DOI: 10.1016/j.energy.2023.127931.

[15] Daniarta, S. and Kolasiński, P. “An integration of geothermal energy, waste, and cold energy system employing the technology of organic Rankine cycle”. In: *Proceedings of the 6th International Seminar on ORC Power Systems*. Technical University of Munich. Technical University of Munich, 2021. DOI: 10.14459/2021mp1633104.

[16] Daniarta, S. and Kolasiński, P. “Features and characteristics of low-grade heat storage for organic Rankine cycle”. In: *Proceedings of the 6th International Seminar on ORC Power Systems*. Ed. by Munich, Technical University of. Technical University of Munich. Technical University of Munich, 2021. DOI: 10.14459/2021mp1633107.

[17] Kolasiński, P. and Daniarta, S. “Sizing the thermal energy storage (TES) device for organic Rankine cycle (ORC) power systems”. In: *MATEC Web Conf.* 345 (2021), p. 00018. DOI: 10.1051/matecconf/202134500018.

[18] Daniarta, S. et al. “Sizing the Thermal Energy Storage Device Utilizing Phase Change Material (PCM) for Low-Temperature Organic Rankine Cycle Systems Employing Selected Hydrocarbons”. In: *Energies* 15 (2022). DOI: 10.3390/en15030956.

[19] Tartière, T. and Astolfi, M. *ORC World Map*. Accessed: 24 February 2024. 2024. URL: https://orc-world-map.org/.

[20] Daniarta, S. et al. “Techno-economic survey of enhancing Power-to-Methane efficiency via waste heat recovery from electrolysis and biomethanation”. In: *Renewable and Sustainable Energy Reviews* 194 (2024), p. 114301. DOI: 10.1016/j.rser.2024.114301.

[21] Zanelli, R. and Favrat, D. “Experimental Investigation of a Hermetic Scroll Expander–Generator.” In: *Proceedings of the International Compressor Engineering Conference at Purdue* (Jan. 1994).

[22] Nguyen, V.M., Doherty, P.S., and Riffat, S.B. “Development of a prototype low-temperature Rankine cycle electricity generation system”. In: *Applied Thermal Engineering* 21 (2001), pp. 169–181. DOI: `10.1016/S1359-4311(00)00052-1`.

[23] Yagoub, W., Doherty, P., and Riffat, S.B. “Solar energy-gas driven micro-CHP system for an office building”. In: *Applied Thermal Engineering* 26 (2006), pp. 1604–1610. DOI: `10.1016/j.applthermaleng.2005.11.021`.

[24] Manolakos, D. et al. “Experimental evaluation of an autonomous low- temperature solar Rankine cycle system for reverse osmosis desalination”. In: *Desalination* 203 (2007), pp. 366–374. DOI: `10.1016/j.desal.2006.04.018`.

[25] Manolakos, D. et al. “On site experimental evaluation of a low-temperature solar organic Rankine cycle system for RO desalination”. In: *Solar Energy* 83 (2009), pp. 646–656. DOI: `10.1016/j.solener.2008.10.014`.

[26] Wang, X.D. et al. “Performance evaluation of a low-temperature solar Rankine cycle system utilizing R245fa”. In: *Solar Energy* 84 (2010), pp. 353–364. DOI: `10.1016/j.solener.2009.11.004`.

[27] A. Bryszewska-Mazurek, T. Świeboda and Mazurek, W. “Performance Analysis of a Solar-Powered Organic Rankine Cycle Engine”. In: *Journal of the Air & Waste Management Association* 61 (2011), pp. 3–6. DOI: `10.3155/1047-3289.61.1.3`.

[28] Borsukiewicz-Gozdur, A. “Experimental investigation of R227ea applied as working fluid in the ORC power plant with hermetic turbogenerator”. In: *Applied Thermal Engineering* 56 (2013), pp. 126–133. DOI: `10.1016/j.applthermaleng.2013.03.039`.

[29] Farrokhi, M., Noie, S.H., and Akbarzadeh, A.A. “Preliminary experimental investigation of a natural gas-fired ORC-based micro-CHP system for residential buildings”. In: *Applied Thermal Engineering* 69 (2014), pp. 221–229. DOI: `10.1016/j.applthermaleng.2013.11.060`.

[30] Wei, L. et al. “Simulation and Experimental Research of a Low-grade Energy Conversion System Using Organic Rankine Cycles”. In: *Energy Sources, Part A: Recovery, Utilization, and Environmental Effects* 36 (2014), pp. 537–546. DOI: `10.1080/15567036.2010.544001`.

[31] Mu, Y. et al. “Experimental Study of a Low-Temperature Power Generation System in an Organic Rankine Cycle”. In: *Journal of Energy Engineering* 141 (2015), p. 04014017. DOI: `10.1061/(ASCE)EY.1943-7897.0000181`.

[32] Kolasiński, P. “The Influence of the Heat Source Temperature on the Multivane Expander Output Power in an Organic Rankine Cycle (ORC) System”. In: *Energies* 8 (2015), pp. 3351–3369. DOI: `10.3390/en8053351`.

[33] Kolasiński, P., Błasiak, P., and Rak, J. “Experimental and Numerical Analyses on the Rotary Vane Expander Operating Conditions in a Micro Organic Rankine Cycle System”. In: *Energies* 9 (2016). DOI: `10.3390/en9080606`.

[34] Helvaci, H.U. and Khan, Z.A. “Experimental study of thermodynamic assessment of a small scale solar thermal system”. In: *Energy Conversion and Management* 117 (2016), pp. 567–576. DOI: `10.1016/j.enconman.2016.03.050`.

[35] Kosmadakis, G. et al. “Experimental testing of a low-temperature organic Rankine cycle (ORC) engine coupled with concentrating PV/thermal collectors: Laboratory and field tests”. In: *Energy* 117 (2016), pp. 222–236. DOI: `10.1016/j.energy.2016.10.047`.

[36] Dong, S. et al. “Optimum design method of Organic Rankine Cycle system based on semi-empirical model and experimental validation”. In: *Energy Conversion and Management* 108 (2016), pp. 85–95. DOI: `10.1016/j.enconman.2015.10.083`.

[37] Pu, W. et al. “Experimental study on Organic Rankine cycle for low grade thermal energy recovery”. In: *Applied Thermal Engineering* 94 (2016), pp. 221–227. DOI: `10.1016/j.applthermaleng.2015.09.120`.

[38] Kim, D. K. et al. “Parametric study and performance evaluation of an organic Rankine cycle (ORC) system using low-grade heat at temperatures below 80°C”. In: *Applied Energy* 189 (2017), pp. 55–65. DOI: `10.1016/j.apenergy.2016.12.026`.

[39] Li, L. et al. “Experimental investigations into power generation with low grade waste heat and R245fa Organic Rankine Cycles (ORCs)”. In: *Applied Thermal Engineering* 115 (2017), pp. 815–824. DOI: `10.1016/j.applthermaleng.2017.01.024`.

[40] Nematollahi, O. et al. “Experimental study of the effect of brazed compact metal-foam evaporator in an organic Rankine cycle performance: Toward a compact ORC”. In: *Energy Conversion and Management* 173 (2018), pp. 37–45. DOI: `10.1016/j.enconman.2018.07.071`.

[41] Kim, J., Kim, D., and Kim, Y. “Experiment on radial inflow turbines and performance prediction using deep neural network for the organic Rankine cycle”. In: *Applied Thermal Engineering* 149 (2019), pp. 633–643. DOI: `10.1016/j.applthermaleng.2018.12.084`.

[42] Liu, C. et al. “Experimental study of micro-scale organic Rankine cycle system based on scroll expander”. In: *Energy* 188 (2019), p. 115930. DOI: `10.1016/j.energy.2019.115930`.

[43] Dickes, R., Dumont, O., and Lemort, V. “Experimental assessment of the fluid charge distribution in an organic Rankine cycle (ORC) power system”. In: *Applied Thermal Engineering* 179 (2020), p. 115689. DOI: `10.1016/j.applthermaleng.2020.115689`.

[44] Wang, W. et al. “Experimental Study on Heat Loss of a Single Screw Expander for an Organic Rankine Cycle System”. In: *Frontiers in Energy Research* 8 (2020). DOI: `10.3389/fenrg.2020.587726`.

[45] Kolasiński, P. “Domestic Organic Rankine Cycle-Based Cogeneration Systems as a Way to Reduce Dust Emissions in Municipal Heating”. In: *Energies* 13 (2020). DOI: `10.3390/en13153983`.

[46] Gou, Y., Li, L., and Min, H. “Design and performance experiment of radial inflow turbine expander for organic Rankine cycle system”. In: *International Journal of Low-Carbon Technologies* 16 (May 2021), pp. 1202–1209. DOI: `10.1093/ijlct/ctab043`.

[47] Rijpkema, J., Andersson, S. B., and Munch, K. “Experimental study of an organic Rankine cycle with R1233zd(E) for waste heat recovery from the coolant of a heavy-duty truck engine”. In: *Energy Conversion and Management* 244 (2021), p. 114500. DOI: `10.1016/j.enconman.2021.114500`.

[48] Liang, Y. and Yu, Z. “Experimental investigation of an Organic Rankine cycle system using an oil-free scroll expander for low grade heat recovery”. In: *International Journal of Green Energy* 18 (2021), pp. 812–821. DOI: `10.1080/15435075.2021.1880915`.

[49] Lei, M. et al. “Experimental investigation on the characteristics of heat exchangers based on organic Rankine cycle system under different operating conditions”. In: *International Journal of Energy Research* 45 (2021), pp. 13365–13379. DOI: `10.1002/er.6664`.

[50] İpek, O. et al. “Experimental investigation of low-temperature organic Rankine cycle using waste heat from gas turbine bearings for different conditions”. In: *International Journal of Environmental Science and Technology* 19 (2022), pp. 1519–1530. DOI: `10.1007/s13762-021-03172-x`.

[51] Lhermet, G. et al. “A Recent Advance on Partial Evaporating Organic Rankine Cycle: Experimental Results on an Axial Turbine”. In: *Energies* 15 (2022). DOI: `10.3390/en15207559`.

[52] Ottaviano, S. et al. “Experimental investigation on micro-ORC system operating with partial evaporation and two-phase expansion”. In: *Energy Conversion and Management* 274 (2022), p. 116415. DOI: `10.1016/j.enconman.2022.116415`.

[53] Braimakis, K. and Karellas, S. “Exergy efficiency potential of dual-phase expansion trilateral and partial evaporation ORC with zeotropic mixtures”. In: *Energy* 262 (2023), p. 125475. DOI: `10.1016/j.energy.2022.125475`.

[54] Badr, O. et al. “Expansion machine for a low power-output steam Rankine-cycle engine”. In: *Applied Energy* 39 (1991), pp. 93–116. DOI: `10.1016/0306-2619(91)90024-R`.

[55] Badr, O. et al. “Multi-vane expanders as prime movers for low-grade energy organic Rankine-cycle engines”. In: *Applied Energy* 16 (1984), pp. 129–146. DOI: `10.1016/0306-2619(84)90060-6`.

[56] Badr, O. et al. “Wankel engines as steam expanders: Design considerations”. In: *Applied Energy* 40 (1991), pp. 157–170. DOI: 10.1016/0306-2619(91)90055-3.

[57] Smith, I. K., Stosic, N., and Kovacevic, A. “1 - Expanders for power recovery”. In: *Power Recovery from Low Grade Heat by Means of Screw Expanders (Second Edition)*. Ed. by Smith, Ian K., Stosic, Nikola, and Kovacevic, Ahmed. Second Edition. Oxford: Chandos Publishing, 2014, pp. 1–12. DOI: 10.1533/9781782421900.1.

[58] Daniarta, S. and Kolasiński, P. “A preliminary study of two-phase volumetric expanders and their application in ORC systems”. In: *Proceedings of the 6th International Seminar on ORC Power Systems*. Ed. by Munich, Technical University of. Technical University of Munich. Technical University of Munich, 2021. DOI: 10.14459/2021mp1633105.

[59] Hijikata, K. and Mori, Y. “Prototype of rotary two-phase flow expander”. In: *Proceedings of the Japan Society of Mechanical Engineers, Volume B* 48 (1982), pp. 160–167. DOI: 10.1299/kikaib.48.160.

[60] Gopal, V. V. and Seshadri, S. “Effect of cut-off and compression ratio on the isentropic efficiency during off-design and part-load operations of a Wankel rotary steam expander used for small scale cogeneration”. In: *Applied Thermal Engineering* 207 (2022), p. 118212. DOI: 10.1016/j.applthermaleng.2022.118212.

[61] Imran, M. and Usman, M. “Chapter 11 - Mathematical modelling for positive displacement expanders”. In: *Positive Displacement Machines*. Ed. by Sultan, Ibrahim A. and Phung, Truong H. Academic Press, 2019, pp. 293–343. ISBN: 978-0-12-816998-8. DOI: 10.1016/B978-0-12-816998-8.00011-X.

[62] Kanno, H. and Shikazono, N. “Experimental study on two-phase adiabatic expansion in a reciprocating expander with intake and exhaust processes”. In: *International Journal of Heat and Mass Transfer* 102 (2016), pp. 1004–1011. DOI: 10.1016/j.ijheatmasstransfer.2016.06.081.

[63] Heule, X. van, Paepe, M. De, and Lecompte, S. “Two-Phase Volumetric Expanders: A Review of the State-of-the-Art”. In: *Energies* 15 (2022). DOI: 10.3390/en15144991.

[64] Francesconi, M., Briola, S., and Antonelli, M. “A Review on Two-Phase Volumetric Expanders and Their Applications”. In: *Applied Sciences* 12 (2022). DOI: 10.3390/app122010328.

[65] Kolasiński, P. “Application of the Multi-Vane Expanders in ORC Systems—A Review on the Experimental and Modeling Research Activities”. In: *Energies* 12 (2019). DOI: 10.3390/en12152975.

[66] Smith, I. K. “Development of the Trilateral Flash Cycle System: Part 1: Fundamental Considerations”. In: *Proceedings of the Institution of Mechanical Engineers, Part A: Journal of Power and Energy* 207 (1993), pp. 179–194. DOI: 10.1243/PIME_PROC_1993_207_032_02.

[67] Daniarta, S. and Imre, A. R. “Cold Energy Utilization in LNG Regasification System using Organic Rankine Cycle and Trilateral Flash Cycle”. In: *Periodica Polytechnica Mechanical Engineering* 64 (2020), pp. 342–349. DOI: `10.3311/PPme.16668`.

[68] Zeynali, A., Akbari, A., and Khalilian, M. “Investigation of the performance of modified organic Rankine cycles (ORCs) and modified trilateral flash cycles (TFCs) assisted by a solar pond”. In: *Solar Energy* 182 (2019), pp. 361–381. DOI: `j.solener.2019.03.001`.

[69] Lai, K. et al. “Comparison of the Trilateral Flash Cycle and Rankine Cycle with Organic Fluid Using the Pinch Point Temperature”. In: *Entropy* 21 (2019). DOI: `10.3390/e21121197`.

[70] Rijpkema, J., Munch, K., and Andersson, S.B. “Thermodynamic potential of twelve working fluids in Rankine and flash cycles for waste heat recovery in heavy duty diesel engines”. In: *Energy* 160 (2018), pp. 996–1007. DOI: `10.1016/j.energy.2018.07.003`.

[71] Elliot, D. G. “Theory and tests of two-phase turbines”. In: (Mar. 1982). DOI: `10.2172/5346135`. URL: `https://www.osti.gov/biblio/5346135`.

[72] Fischer, J. “Comparison of trilateral cycles and organic Rankine cycles”. In: *Energy* 36 (2011), pp. 6208–6219. DOI: `10.1016/j.energy.2011.07.041`.

[73] Li, Z. et al. “Comparison study of Trilateral Rankine Cycle, Organic Flash Cycle and basic Organic Rankine Cycle for low grade heat recovery”. In: *Energy Procedia* 142 (2017). Proceedings of the 9th International Conference on Applied Energy, pp. 1441–1447. DOI: `10.1016/j.egypro.2017.12.532`.

[74] Ahmed, A. M., Kondor, L., and Imre, A. R. “Thermodynamic Efficiency Maximum of Simple Organic Rankine Cycles”. In: *Energies* 14 (2021). DOI: `10.3390/en14020307`.

[75] Eyerer, S. “Contribution to Improve the Organic Rankine Cycle”. English. PhD thesis. Munich, Germany: Technische Universität München, 2021. URL: `https://mediatum.ub.tum.de/?id=1576831`.

[76] Zhang, X., He, M., and Wang, J. “A new method used to evaluate organic working fluids”. In: *Energy* 67 (2014), pp. 363–369. DOI: `10.1016/j.energy.2014.01.030`.

[77] Secretariat, Ozone. “The Montreal protocol on substances that deplete the ozone layer”. In: *United Nations Environment Programme, Nairobi, Kenya* (2000).

[78] Nations, United. “Kyoto protocol to the united nations framework convention on climate change”. In: (1998).

[79] Badr, O., Probert, S. D., and O’Callaghan, P. W. “Selecting a working fluid for a Rankine-cycle engine”. In: *Applied Energy* 21 (1985), pp. 1–42. DOI: `10.1016/0306-2619(85)90072-8`.

[80] Groniewsky, A., Györke, G., and Imre, A. R. “Description of wet-to-dry transition in model ORC working fluids”. In: *Applied Thermal Engineering* 125 (2017), pp. 963–971. DOI: `10.1016/j.applthermaleng.2017.07.074`.

[81] Györke, G. et al. “Novel classification of pure working fluids for Organic Rankine Cycle”. In: *Energy* 145 (2018), pp. 288–300. DOI: `10.1016/j.energy.2017.12.135`.

[82] Györke, G. “Thermodynamic analysis of power cycles and their basic processes under non-conventional conditions”. Hungarian. PhD thesis. Budapest, Hungary: Budapest University of Technology and Economics, 2019, p. 112. URL: `http://hdl.handle.net/10890/13336`.

[83] Zhang, X., Zhang, Y., and Wang, J. “New classification of dry and isentropic working fluids and a method used to determine their optimal or worst condensation temperature used in Organic Rankine Cycle”. In: *Energy* 201 (2020), p. 117722. DOI: `10.1016/j.energy.2020.117722`.

[84] Zhang, X. and Li, Y. “An examination of super dry working fluids used in regenerative organic Rankine cycles”. In: *Energy* 263 (2023), p. 125931. DOI: `10.1016/j.energy.2022.125931`.

[85] Kustán, R. “Working fluid selection for organic Rankine cycle based on saturation curve properties”. Hungarian. PhD thesis. Budapest, Hungary: Budapest University of Technology and Economics, 2023, p. 125. URL: `http://hdl.handle.net/10890/51354`.

[86] Daniarta, S., Kolasiński, P., and Imre, A. R. “Thermodynamic efficiency of trilateral flash cycle, organic Rankine cycle and partially evaporated organic Rankine cycle”. In: *Energy Conversion and Management* 249 (2021), p. 114731. DOI: `10.1016/j.enconman.2021.114731`.

[87] Bell, I. H. et al. “Pure and Pseudo-pure Fluid Thermophysical Property Evaluation and the Open-Source Thermophysical Property Library CoolProp”. In: *Industrial & Engineering Chemistry Research* 53 (2014), pp. 2498–2508. DOI: `10.1021/ie4033999`.

[88] Lemmon, E. W. et al. *NIST Standard Reference Database 23: Reference Fluid Thermodynamic and Transport Properties-REFPROP, Version 10.0, National Institute of Standards and Technology*. 2018. DOI: `10.18434/T4/1502528`. URL: `https://www.nist.gov/srd/refprop`.

[89] Domingues, A., Matos, H. A., and Pereira, P. M. “Novel integrated system of LNG regasification / electricity generation based on a cascaded two-stage Rankine cycle, with ternary mixtures as working fluids and seawater as hot utility”. In: *Energy* 238 (2022), p. 121972. DOI: `10.1016/j.energy.2021.121972`.

[90] Chowdhury, A. S. and Ehsan, M. M. “A Critical Overview of Working Fluids in Organic Rankine, Supercritical Rankine, and Supercritical Brayton Cycles Under Various Heat Grade Sources”. In: *International Journal of Thermofluids* 20 (2023), p. 100426. DOI: `10.1016/j.ijft.2023.100426`.

[91] Krempus, D. et al. “On mixtures as working fluids of air-cooled ORC bottoming power plants of gas turbines”. In: *Applied Thermal Engineering* 236 (2024), p. 121730. DOI: 10.1016/j.applthermaleng.2023.121730.

[92] Daniarta, S., Imre, A. R., and Kolasiński, P. “Exploring performance map: theoretical analysis of subcritical and transcritical power cycles with wet and isentropic working fluids”. In: *Energy* 299 (2024), p. 131450. DOI: 10.1016/j.energy.2024.131450.

[93] Daniarta, S., Imre, A. R., and Kolasiński, P. “The efficiency of transcritical CO2 cycle near critical point and with high temperature”. In: *MATEC Web Conf.* 345 (2021), p. 00005. DOI: 10.1051/matecconf/202134500005.

[94] Daniarta, S. and Kolasiński, P. “A Comparative Study of Cooling Sources in Organic Rankine Cycle for Low-Temperature Geothermal Heat Sources”. In: *IOP Conference Series: Earth and Environmental Science* 1014 (Apr. 2022), p. 012008. DOI: 10.1088/1755-1315/1014/1/012008.

[95] Banuti, D.T., Raju, M., and Ihme, M. “Between supercritical liquids and gases – Reconciling dynamic and thermodynamic state transitions”. In: *The Journal of Supercritical Fluids* 165 (2020), p. 104895. DOI: 10.1016/j.supflu.2020.104895.

[96] Imre, A.R. et al. “The pseudocritical regions for supercritical water”. In: *Nuclear Engineering and Design* 252 (2012), pp. 179–183. DOI: 10.1016/j.nucengdes.2012.07.007.

[97] Imre, A. R. et al. “Anomalous fluid properties of carbon dioxide in the supercritical region: application to geological CO2 storage and related hazards”. In: *Environmental Earth Sciences* 73 (2015), pp. 4373–4384. DOI: 10.1007/s12665-014-3716-5.

[98] Banuti, D.T. “Crossing the Widom-line – Supercritical pseudo-boiling”. In: *The Journal of Supercritical Fluids* 98 (2015), pp. 12–16. DOI: 10.1016/j.supflu.2014.12.019.

[99] Imamura, T. et al. “Critical ignition conditions for propane/air premixtures impinging on electric heated surfaces: An experimental study”. In: *Fire Safety Journal* 140 (2023), p. 103897. DOI: 10.1016/j.firesaf.2023.103897.

[100] Ge, Z. et al. “Thermodynamic and economic performance evaluations of double-stage organic flash cycle using hydrofluoroolefins (HFOs)”. In: *Renewable Energy* 220 (2024), p. 119593. DOI: 10.1016/j.renene.2023.119593.

[101] Meng, D., Liu, Q., and Ji, Z. “Effects of two-phase expander on the thermoeconomics of organic double-flash cycles for geothermal power generation”. In: *Energy* 239 (2022), p. 122346. DOI: 10.1016/j.energy.2021.122346.

[102] Carlos Mendoza, L., Lemofouet, S., and Schiffmann, J. “Two-phase and oil-free co-rotating scroll compressor/expander”. In: *Applied Thermal Engineering* 148 (2019), pp. 173–187. DOI: 10.1016/j.applthermaleng.2018.11.037.

[103] Dawo, F. et al. “Experimental assessment of an Organic Rankine Cycle with a partially evaporated working fluid”. In: *Applied Thermal Engineering* 221 (2023), p. 119858. DOI: `10.1016/j.applthermaleng.2022.119858`.

[104] Fukuta, M. et al. “Observation of CO2 trans-critical expansion process”. In: *International Refrigeration and Air Conditioning Conference*. 2008.

[105] Daniarta, S. et al. “Artificial intelligence-driven performance mapping: a deep learning-based investigation of a multi-vane expander in retrofitted organic Rankine cycle”. In: *Energy Conversion and Management* (2024). accepted.

[106] Ying, C. et al. “Deep learning for renewable energy forecasting: A taxonomy, and systematic literature review”. In: *Journal of Cleaner Production* 384 (2023), p. 135414. DOI: `10.1016/j.jclepro.2022.135414`.

[107] Morteza, A. et al. “Deep learning hyperparameter optimization: Application to electricity and heat demand prediction for buildings”. In: *Energy and Buildings* 289 (2023), p. 113036. DOI: `10.1016/j.enbuild.2023.113036`.

[108] Shen, Z., Yang, H., and Zhang, S. “Neural network approximation: Three hidden layers are enough”. In: *Neural Networks* 141 (2021), pp. 160–173. DOI: `10.1016/j.neunet.2021.04.011`.

[109] Baumann, K. “Some recent developments in large steam turbine practice”. In: *Journal of the institution of electrical engineers* 59 (1921), pp. 565–623.

[110] Cao, J. et al. “Recent progress in organic Rankine cycle targeting utilisation of ultra-low-temperature heat towards carbon neutrality”. In: *Applied Thermal Engineering* 231 (2023), p. 120903. DOI: `10.1016/j.applthermaleng.2023.120903`.

[111] Malwe, P. et al. “Exergy assessment of an Organic Rankine Cycle for waste heat recovery from a refrigeration system: a review”. In: *Chemical Engineering Communications* 210 (2023), pp. 837–865. DOI: `10.1080/00986445.2021.1980396`.

[112] Li, X. et al. “Towards a novel holistic design of organic Rankine cycle (ORC) systems operating under heat source fluctuations and intermittency”. In: *Renewable and Sustainable Energy Reviews* 147 (2021), p. 111207. DOI: `10.1016/j.rser.2021.111207`.

[113] Faizal, M. and Ahmed, M. R. “On the ocean heat budget and ocean thermal energy conversion”. In: *International Journal of Energy Research* 35 (2011), pp. 1119–1144. DOI: `10.1002/er.1885`.

[114] Vera, D. et al. “Modeling and optimization of an ocean thermal energy conversion system for remote islands electrification”. In: *Renewable Energy* 162 (2020), pp. 1399–1414. DOI: `10.1016/j.renene.2020.07.074`.

[115] Li, D. et al. “Numerical study on ocean thermal energy conversion system”. In: *Journal of Renewable and Sustainable Energy* 10 (July 2018), p. 044501. DOI: `10.1063/1.5034034`.

[116] Han, C. and Yu, X. B. “Sensitivity analysis of a vertical geothermal heat pump system”. In: *Applied Energy* 170 (2016), pp. 148–160. DOI: `10.1016/j.apenergy.2016.02.085`.

[117] Bu, X., Jiang, K., and Li, H. “Performance of geothermal single well for intermittent heating”. In: *Energy* 186 (2019), p. 115858. DOI: `10.1016/j.energy.2019.115858`.

[118] Duggal, R. et al. “A comprehensive review of energy extraction from low-temperature geothermal resources in hydrocarbon fields”. In: *Renewable and Sustainable Energy Reviews* 154 (2022), p. 111865. DOI: `10.1016/j.rser.2021.111865`.

[119] Kanbur, B. B. et al. “Cold utilization systems of LNG: A review”. In: *Renewable and Sustainable Energy Reviews* 79 (2017), pp. 1171–1188. DOI: `10.1016/j.rser.2017.05.161`.

[120] Kahraman, M. and Olcay, A. B. “Techno-economic analysis of evaporative cooling enhancement methods of a 21 MW air-cooled geothermal power plant”. In: *Geothermics* 107 (2023), p. 102598. DOI: `10.1016/j.geothermics.2022.102598`.

[121] Lee, S. “Multi-parameter optimization of cold energy recovery in cascade Rankine cycle for LNG regasification using genetic algorithm”. In: *Energy* 118 (2017), pp. 776–782. DOI: `10.1016/j.energy.2016.10.118`.

[122] Lee, H. Y., Park, S. H., and Kim, K. H. “Comparative analysis of thermodynamic performance and optimization of organic flash cycle (OFC) and organic Rankine cycle (ORC)”. In: *Applied Thermal Engineering* 100 (2016), pp. 680–690. DOI: `10.1016/j.applthermaleng.2016.01.158`.

[123] Dumont, O. et al. “Carnot battery technology: A state-of-the-art review”. In: *Journal of Energy Storage* 32 (2020), p. 101756. DOI: `10.1016/j.est.2020.101756`.

[124] Frate, G. F., Ferrari, L., and Desideri, U. “Rankine Carnot Batteries with the Integration of Thermal Energy Sources: A Review”. In: *Energies* 13 (2020). DOI: `10.3390/en13184766`.

[125] Müller, N. and Fréchette, L. G. “Performance Analysis of Brayton and Rankine Cycle Microsystems for Portable Power Generation”. In: *ASME International Mechanical Engineering Congress and Exposition*. 2002, pp. 513–522. DOI: `10.1115/IMECE2002-39628`.

[126] Dumont, O. et al. “Performance of a reversible heat pump/organic Rankine cycle unit coupled with a passive house to get a positive energy building”. In: *Journal of Building Performance Simulation* 11 (2018), pp. 19–35. DOI: `10.1080/19401493.2016.1265010`.

[127] Staub, S. et al. “Reversible Heat Pump–Organic Rankine Cycle Systems for the Storage of Renewable Electricity”. In: *Energies* 11 (2018). DOI: `10.3390/en11061352`.

[128] Daniarta, S., Kolasiński, P., and Imre, A. R. “Performance map and theoretical analysis of Carnot battery technology via novel reversible Rankine-based cycle”. In: *Energy Reports* 11 (2024), pp. 4500–4514. DOI: `10.1016/j.egyr.2024.04.024`.

[129] Cipriani, M. *Electromagnetic device with reversible generator-motor operation*. US Patent 8,536,751. Sept. 2013.

[130] Cipriani, M. *Modular electromagnetic device with reversible generator-motor operation*. US Patent 8,354,768. Jan. 2013.

[131] Fan, R. and Xi, H. “Energy, exergy, economic (3E) analysis, optimization and comparison of different Carnot battery systems for energy storage”. In: *Energy Conversion and Management* 252 (2022), p. 115037. DOI: `h10.1016/j.enconman.2021.115037`.

[132] Zhang, J. et al. “Revising the Ozone Depletion Potentials Metric for Short-Lived Chemicals Such as CF3I and CH3I”. In: *Journal of Geophysical Research: Atmospheres* 125 (2020), e2020JD032414. DOI: `10.1029/2020JD032414`.

[133] White, M. T. “Cycle and turbine optimisation for an ORC operating with two-phase expansion”. In: *Applied Thermal Engineering* 192 (2021), p. 116852. DOI: `10.1016/j.applthermaleng.2021.116852`.

[134] Daniarta, S. and Imre, A. R. “Cold Energy Utilization in LNG Regasification System Using Organic Rankine Cycle and Trilateral Flash Cycle”. In: *Periodica Polytechnica Mechanical Engineering* 64 (2020), pp. 342–349. DOI: `10.3311/PPme.16668`.

[135] IEA. *Nitrogen Demand by End Use and Scenario, 2020-2050*. Accessed: 2023-04-15. Paris: International Energy Agency, 2020. URL: `https://www.iea.org/data-and-statistics/charts/nitrogen-demand-by-end-use-and-scenario-2020-2050`.

[136] Daniarta, S. et al. “Cost-effective option of cold energy utilization in pharmaceutical industry”. In: *Proceedings of the 7th International Seminar on ORC Power Systems*. status: accepted. 2023.

[137] Lemmens, S. “Cost Engineering Techniques and Their Applicability for Cost Estimation of Organic Rankine Cycle Systems”. In: *Energies* 9 (2016). DOI: `10.3390/en9070485`.

[138] Giampieri, A. et al. “A review of the current automotive manufacturing practice from an energy perspective”. In: *Applied Energy* 261 (2020), p. 114074. DOI: `10.1016/j.apenergy.2019.114074`.

[139] Daniarta, S., Kolasiński, P., and Rogosz, B. “Waste Heat Recovery in Automotive Paint Shop via Organic Rankine Cycle and Thermal Energy Storage System—Selected Thermodynamic Issues”. In: *Energies* 15 (2022). DOI: `10.3390/en15062239`.

[140] Daniarta, S., Imre, A. R., and Kolasiński, P. “A novel approach to district heating: using a two-phase expander in reversible heat pump-organic Rankine cycle system”. In: *Proceedings of the 7th International Seminar on ORC Power Systems*. status: accepted. 2023.

[141] Daniarta, S., Kolasiński, P., and Imre, A. R. “A Preliminary Design and Modeling Analysis of Two-Phase Volumetric Expanders for a Novel Reversible Organic Rankine-Based Cycle for Carnot Battery Technology”. In: *Applied Sciences* 12 (2022). DOI: `10.3390/app12073557`.

[142] Andrzejczyk, R. “Experimental Investigation of the Thermal Performance of a Wickless Heat Pipe Operating with Different Fluids: Water, Ethanol, and SES36. Analysis of Influences of Instability Processes at Working Operation Parameters”. In: *Energies* 12 (2019). DOI: `10.3390/en12010080`.

[143] Yang, H. et al. “Performance analysis of an Organic Rankine Cycle system using evaporative condenser for sewage heat recovery in the petrochemical industry”. In: *Energy Conversion and Management* 205 (2020), p. 112402. DOI: `10.1016/j.enconman.2019.112402`.

List of author's publications related to this dissertation

The following publications derived in relation to the work in this dissertation have been presented in several peer-reviewed journals and in international scientific conference proceedings. The list of publications is organized based on the publication year from 2021 to 2024, as follows:

Articles published in peer-reviewed journals

- **Daniarta, S.**, Kolasiński, P., Imre, A. R. (2021). Thermodynamic efficiency of trilateral flash cycle, organic Rankine cycle and partially evaporated organic Rankine cycle. Energy Conversion and Management, 249, 114731, DOI: 10.1016/j.enconman.2021.114731; (Included in Reference, see Ref. [86]);
- **Daniarta, S.**, Kolasiński, P., Rogosz, B. (2022). Waste Heat Recovery in Automotive Paint Shop via Organic Rankine Cycle and Thermal Energy Storage System—Selected Thermodynamic Issues. Energies, 15(6), 2239, DOI: 10.3390/en15062239; (Included in Reference, see Ref. [139]);
- **Daniarta, S.**, Nemś, M., Kolasiński, P., Pomorski, M. (2022). Sizing the thermal energy storage device utilizing phase change material (PCM) for low-temperature organic Rankine cycle systems employing selected hydrocarbons. Energies, 15(3), 956, DOI: 10.3390/en15030956; (Included in Reference, see Ref. [18]);
- **Daniarta, S.**, Kolasiński, P., Imre, A. R. (2022). A Preliminary design and modeling analysis of two-phase volumetric expanders for a novel reversible Organic Rankine-Based Cycle for Carnot battery technology. Applied Sciences, 12(7), 3557, DOI: 10.3390/app12073557;(Included in Reference, see Ref. [141]);
- **Daniarta, S.**, Imre, A. R., Kolasiński, P. (2022). Thermodynamic efficiency of subcritical and transcritical power cycles utilizing selected ACZ working fluids. Energy, 254, 124432, DOI: 10.1016/j.energy.2022.124432; (Included in Reference, see Ref. [6]);
- **Daniarta, S.**, Nemś, M., Kolasiński, P. (2023). A review on thermal energy storage applicable for low-and medium-temperature organic Rankine cycle. Energy, 278, 127931, DOI: 10.1016/j.en ergy.2023.127931; (Included in Reference, see Ref. [14]);
- Imre, A. R., **Daniarta, S.**, Błasiak, P., Kolasiński, P. (2023). Design, Integration, and Control of Organic Rankine Cycles with Thermal Energy Storage and Two-Phase Expansion System Utilizing Intermittent and Fluctuating Heat Sources—A Review. Energies, 16(16), 5948, DOI: 10.3390/en16165948; (Included in Reference, see Ref. [13]);

- **Daniarta, S.**, Sowa, D., Błasiak, P., Imre, A. R., Kolasiński, P. (2024). Techno-economic survey of enhancing Power-to-Methane efficiency via waste heat recovery from electrolysis and biomethanation. Renewable and Sustainable Energy Reviews, 194, 114301, DOI: 10.1016/j.rser.2024.114301; (Included in Reference, see Ref. [20]);
- **Daniarta, S.**, Kolasiński, P., Imre, A. R. (2024). Performance map and theoretical analysis of Carnot battery technology via novel reversible Rankine-based cycle. Energy Reports, 11, 4500-4514, DOI: 10.1016/j.egyr.2024.04.024; (Included in Reference, see Ref. [128]);
- **Daniarta, S.**, Imre, A. R., Kolasiński, P. (2024). Exploring performance map: theoretical analysis of subcritical and transcritical power cycles with wet and isentropic working fluids. Energy, 131450. DOI: 10.1016/j.energy.2024.131450; (Included in Reference, see Ref. [92]);
- **Daniarta, S.**, Kolasiński, P., Imre, A. R. Sowa, D., (2024). Artificial intelligence-driven performance mapping: a deep learning-based investigation of a multi-vane expander in retrofitted organic Rankine cycle. Energy Conversion and Management. (status: accepted); (Included in Reference, see Ref. [105]).

Presentation at international scientific conferences, full papers published in proceedings

- **Daniarta, S.**, Kolasiński, P. (2021). An integration of geothermal energy, waste, and cold energy system employing the technology of organic Rankine cycle. In Proceedings of the 6th International Seminar on ORC Power Systems, DOI: 10.14459/2021mp1633104; (Included in Reference, see Ref. [15]);
- **Daniarta, S.**, Kolasiński, P. (2021). A preliminary study of two-phase volumetric expanders and their application in ORC systems. In Proceedings of the 6th International Seminar on ORC Power Systems, DOI: 10.14459/2021mp1633105; (Included in Reference, see Ref. [58]);
- **Daniarta, S.**, Kolasiński, P. (2021). Features and characteristics of low-grade heat storage for organic Rankine cycle. In Proceedings of the 6th International Seminar on ORC Power Systems, DOI: 10.14459/2021mp1633107; (Included in Reference, see Ref. [16]);
- **Daniarta, S.**, Imre, A. R., Kolasiński, P. (2021). The efficiency of transcritical CO2 cycle near critical point and with high temperature. In MATEC Web of Conferences (Vol. 345, p. 00005). EDP Sciences, DOI: 10.1051/matecconf/202134500005; (Included in Reference, see Ref. [93]);
- Kolasiński, P., **Daniarta, S.** (2021). Sizing the thermal energy storage (TES) device for organic Rankine cycle (ORC) power systems. In MATEC Web of Conferences (Vol. 345, p. 00018). EDP Sciences, DOI: 10.1051/matecconf/202134500018; (Included in Reference, see Ref. [17]);
- **Daniarta, S.**, Kolasiński, P. (2022). A Comparative Study of Cooling Sources in Organic Rankine Cycle for Low-Temperature Geothermal Heat Sources. In IOP Conference Series: Earth and Environmental Science (Vol. 1014, No. 1, p.

012008). IOP Publishing, DOI: 10.1088/1755-1315/1014/1/012008; (Included in Reference, see Ref. [94]);

- **Daniarta, S.**, Imre, A.R., Kolasiński, P. (2023) A novel approach to district heating: using a two-phase expander in reversible heat pump-organic Rankine cycle system. At 7th International Seminar on ORC Power Systems, Seville, Spain. (status: accepted); (Included in Reference, see Ref. [140]);
- **Daniarta, S.**, Dawid Sowa, Ádám Havas, Imre, A.R., Kolasiński, P. (2023) Cost-effective option of cold energy utilization in pharmaceutical industry. At 7th International Seminar on ORC Power Systems, Seville, Spain. (status: accepted); (Included in Reference, see Ref. [136]).

A

Thermal properties and classification of working fluids

Table A.1. A list of working fluids with the classification and their thermal properties taken from [87, 88]. The list is continued on the next page.

Working fluid	Classification [81]	Chemical	T_b (K)	T_triple (K)	T_c (K)	p_c (MPa)
Butane (R600)	ACNMZ	C_4H_{10}	272.66	134.90	425.13	3.80
Butene	ACNMZ	C_4H_8	266.84	87.80	419.29	4.01
Carbon dioxide (R744)	ACZ	CO_2	194.69	216.59	304.13	7.38
Cyclohexane	ANZCM [1]	C_6H_{12}	353.87	279.86	553.60	4.08
D4	AZCM	$C_8H_{24}O_4Si_4$	448.89	290.25	586.50	1.35
D5	AZCM	$C_{10}H_{30}O_5Si_5$	484.06	226.00	618.30	1.09
D6	AZCM	$C_{12}H_{36}Si_6O_6$	518.11	270.20	645.78	0.96
Decane	ANZCM [1]	$C_{10}H_{22}$	447.27	243.50	617.70	2.10

[1] It is important to note that although these substances appear to be isentropic working fluids (ANZCM types) based on ACZMN points, these isentropic working fluids behave like dry ones in most parts of the relevant temperature range due to the proximity of the point N to Z. These working fluids are also classified as dry working fluids according to other alternative classifications [83, 84].

Table A.1. *(continued).*

Working fluid	**Classi-fication** [81]	**Chemical**	T_b **(K)**	T_{triple} **(K)**	T_c **(K)**	p_c **(MPa)**
Dimethyl ether (RE170 or DME)	ACZ	C_2H_6O	248.37	131.66	400.38	5.34
Dodecane	AZCM	$C_{12}H_{26}$	489.44	263.60	658.10	1.82
Ethylbenzene	ANCMZ	C_8H_{10}	409.31	178.20	617.12	3.62
Hydrogen (R702)	ACZ	H_2	20.37	13.96	33.15	1.30
Heptane	ANZCM	C_7H_{16}	371.55	182.55	540.20	2.74
Hexane	ANZCM	C_6H_{14}	341.87	177.83	507.82	3.04
HFE7000 [51]	AZCM	$C_4H_3F_7O$	307.33	150.65	437.70	2.48
HFE7100 [37]	AZCM	$C_4F_9OCH_3$	n.a.	n.a.	468.45	2.23
Isobutane (R600a)	ACNMZ	C_4H_{10}	261.40	113.73	407.81	3.63
Isohexane	ANCMZ	C_6H_{14}	333.36	119.60	497.70	3.04
Isopentane (R601a)	ANCMZ	C_5H_{12}	300.98	112.65	460.35	3.38
MD2M	ANZCM [1]	$C_{10}H_{30}Si_4O_3$	467.59	205.20	599.40	1.14
MD3M	ANZCM [1]	$C_{12}H_{36}Si_5O_4$	503.03	192.00	628.96	0.96
MD4M	AZCM	$C_{14}H_{42}O_5Si_6$	532.91	214.15	653.20	0.84
MDM	ANZCM [1]	$C_8H_{24}O_2Si_3$	425.63	187.20	565.36	1.44
Methyl linoleate	ANZCM [1]	$C_{19}H_{34}O_2$	628.84	238.10	799.00	1.34
Methyl linolenate	ANZCM [1]	$C_{19}H_{32}O_2$	629.13	218.65	772.00	1.37

---

[1] It is important to note that although these substances appear to be isentropic working fluids (ANZCM types) based on ACZMN points, these isentropic working fluids behave like dry ones in most parts of the relevant temperature range due to the proximity of the point N to Z. These working fluids are also classified as dry working fluids according to other alternative classifications [83, 84].

Table A.1. *(continued).*

Working fluid	**Classi-fication** [81]	**Chemical**	T_b **(K)**	T_{triple} **(K)**	T_c **(K)**	p_c **(MPa)**
Methyl oleate	ANZCM [1]	$C_{19}H_{36}O_2$	627.18	253.47	782.00	1.25
Methyl palmitate	AZCM	$C_{17}H_{34}O_2$	602.27	242.00	755.00	1.35
Methyl stearate	AZCM	$C_{19}H_{38}O_2$	629.56	311.84	775.00	1.24
MM	ANZCM [1]	$C_6H_{18}OSi_2$	373.66	204.93	518.70	1.93
M-xylene	ANZCM	C_8H_{10}	412.21	225.30	616.89	3.53
Nitrogen (R728)	ACZ	N_2	77.36	63.15	126.19	3.40
Neopentane	AZCM	C_5H_{12}	282.65	256.60	433.74	3.20
Ammonia	ACZ	NH_3	239.83	195.49	405.56	11.36
Nonane	ANZCM	C_9H_{20}	423.91	219.70	594.55	2.28
Novec649	AZCM	$C_6F_{12}O$	322.20	165.00	441.81	1.87
n-pentane (R601)	ANCMZ	C_5H_{12}	309.21	143.47	469.70	3.37
Octane	ANZCM	C_8H_{18}	398.79	216.37	568.74	2.48
O-xylene	ANZCM	C_8H_{10}	417.52	247.99	630.26	3.74
Propane (R290)	ACZ	C_3H_8	231.04	85.53	369.89	4.25
P-xylene	ANZCM [1]	C_8H_{10}	411.47	286.40	616.17	3.53
R11 (R11)	ACNMZ	CCl_3F	296.86	162.68	471.11	4.41
R113	ANZCM	$C_2Cl_3F_3$	320.74	236.93	487.21	3.39
R12	ACZ	CCl_2F_2	243.40	116.10	385.12	4.14
R123	ACNMZ	$C_2HCl_2F_3$	300.97	166.00	456.83	3.66

[1] It is important to note that although these substances appear to be isentropic working fluids (ANZCM types) based on ACZMN points, these isentropic working fluids behave like dry ones in most parts of the relevant temperature range due to the proximity of the point N to Z. These working fluids are also classified as dry working fluids according to other alternative classifications [83, 84].

Table A.1. *(continued).*

Working fluid	**Classification** [81]	**Chemical**	T_b **(K)**	T_{triple} **(K)**	T_c **(K)**	p_c **(MPa)**
R1233zd(E)	ACNMZ	$C_3H_2ClF_3$	291.41	195.15	439.60	3.62
R1234yf	ACNMZ	$C_3F_4H_2$	243.67	122.77	367.85	3.38
R1234ze(E)	ACNMZ	$C_3F_4H_2$	254.18	169.00	382.51	3.63
R1234ze(Z)	ACNZM	$C_3F_4H_2$	282.88	238.00	423.27	3.53
R134a	ACZ	$C_2H_2F_4$	247.08	169.85	374.21	4.06
R13I1	ACZ	CF_3I	251.29	195.15	396.44	3.95
R152a	ACZ	$C_2H_4F_2$	249.13	154.56	386.41	4.52
R22	ACZ	$CHClF_2$	232.34	115.73	369.30	4.99
R227ea	ANCMZ	C_3HF_7	256.81	146.35	374.90	2.93
R245fa	ACNMZ	$C_3H_3F_5$	288.20	170.00	427.01	3.65
R365mfc	ANZCM [1]	$C_4H_5F_5$	313.34	239.00	460.00	3.27
R404a	ACZ	mixtures	226.93	200.00	345.27	3.73
RC318	AZCM	C_4F_8	267.18	233.35	388.38	2.78
SES36 [142]	n.a.	n.a.	309.15	233.15	450.75	2.85
Toluene	ANCMZ	C_7H_8	383.75	178.00	591.75	4.13
TY1 [143]	n.a.	n.a.	263.35	n.a.	410.25	4.06
Undecane	ANZCM [1]	$C_{11}H_{24}$	468.93	247.54	638.80	1.99
Water (R718)	ACZ	H_2O	373.12	273.16	647.10	22.06

---

[1] It is important to note that although these substances appear to be isentropic working fluids (ANZCM types) based on ACZMN points, these isentropic working fluids behave like dry ones in most parts of the relevant temperature range due to the proximity of the point N to Z. These working fluids are also classified as dry working fluids according to other alternative classifications [83, 84].